REAL TIME SOLAR AND CONTROLLED EXPERIMENTAL INVESTIGATION OF A LATENT HEAT ENERGY STORAGE SYSTEM

by

Moe Kabbara

Submitted in partial fulfilment of the requirements
for the degree of Master of Applied Science

at

Dalhousie University
Halifax, Nova Scotia
April 2015

To my mother Mona, for all your everlasting support

TABLE OF CONTENTS

LIST OF TABLES

LIST OF FIGURES

ABSTRACT

An experimental characterization of a latent heat energy storage system (LHESS) with dodecanoic acid as the phase change material was conducted under real-time solar and controlled experimental conditions. During charging it was found that natural convection played a significant role, while discharging was mainly dominated by conduction. The heat transfer fluid (HTF) inlet temperature affected the overall performance more significantly than the HTF flow rate. Seasonal evaluation showed that insufficient melting during short days interrupted the onset of natural convection. A comparison between latent and sensible storage showed that the helical coil heat exchanger is not as effective with PCM in comparison with water due to heat transfer limitations. Finned tubes were compared to the helical coil heat exchanger and showed improved performance during charging and discharging. A Fourier number based design method was proposed and validated, which could serve as a useful technique for future designs of LHESS.

List of abbreviations and symbols used

Dimensional Variables

C_p	Specific heat (J kg^{-1} K^{-1})
D	Diameter of pipe (m)
G	Solar irradiance (W m^{-2})
k	Thermal conductivity (W m^{-1} K^{-1})
L	Characteristic length (m)
m	Mass (kg)
$\dot{m}$	Mass flow rate (kg s^{-1})
Q	Energy (kJ)
$\dot{Q}$	Power (W)
R_i	Inner radius of the coil (m)
R_T	Radius of the storage tank (m)
T	Temperature (K)
t	Time (s)
V	Average velocity of the fluid (m s^{-1})
y	Height of the cylindrical volume (m)
Z	Half the pitch of the coil (m)

Greek letters

α	Thermal diffusivity (m^2 s^{-1})
δ	Uncertainty
Δh_m	Latent heat of fusion (kJ kg^{-1})
Δt	Time interval of measurement (s)
ΔT	Temperature difference (K)
μ	Dynamic viscosity (Pa s)
ν	Kinematic viscosity (m^2 s^{-1})
ρ	Density (kg m^{-3})

Subscripts

f	Final
i	Initial
l	Liquid
H	Hot
HTF	Heat transfer fluid
C	Cold
in	Inlet
out	Outlet
c	Cumulative
m	Melting
s	Solid

Abbreviations

HRM	Halifax Regional Municipality
HTF	Heat transfer fluid
LHESS	Latent heat energy storage system
LHS	Latent heat storage
PCM	Phase change material
SDHW	Solar domestic hot water
SHS	Sensible heat storage
TES	Thermal energy storage

Dimensionless numbers

Ste	Stephan number ($C_p\,\Delta T/\Delta h_{m)}$
Re	Reynolds number (VD/ν)
Pr	Prandtl number $(C_p\mu/k)$
Fo	Fourier number $(\alpha t/L)$

Acknowledgments

Foremost, I would like to express my sincere gratitude to my supervisors Dr. Dominic Groulx and Dr. Alain Joseph. Dominic, thanks for all your support and guidance that made this thesis possible, and for your continued support as my upcoming PhD supervisor. Al, this work would have not been possible without your committed support and assistance. You have been a great mentor and supervisor over the past two years and I am hopeful that we will further collaborate in the future, hopefully with no plumbing. I am also grateful for the support of my committee members Dr. Lukas Swan and Dr. Mark Gibson, thanks for taking the time to make sure that my thesis is the best it can be.

I was also very lucky to have had the support of my friend and colleague Louis, a fellow Chem Eng in the Mech world. Thanks for all the technical and emotional support you provided me over the past two years. Thanks to all my office mates: Ben, Trevor, Nick, Laura, Ali, and Tousif. Thanks to all the NSCC fellows that helped make this work possible: The Bens from Austria, Josh, Jack, and Jon. Thanks to Emir for not graduating before me, you walked beside me and reassured me by also taking forever to finish.

I am grateful for the support of my family throughout this whole process even though they were an ocean and a continent away. Hazem, thanks for teaching me how to do algebra with unknown variables in first grade, I think it paid off.

Special thanks for everyone who helped fund my education; it wouldn't have been remotely possible for me to achieve this without your committed support and help throughout my undergraduate program and the beginning of my graduate studies.

Thanks to all of Halifax friends for making this city my home. Alec thanks for your continued support and encouragement, you make me strive to be the best version of myself. Thanks for my roommates, the cats in my life (Georgia, Moo and Roo), and last but not least Sarah for bearing an over caffeinated and sleep deprived version of myself.

CHAPTER 1 INTRODUCTION

1.1 BACKGROUND

Canadians rank among the highest per capita energy users in the world due in part to the colder Canadian climate and geography (IEA, 2008). Thermal energy for space and water heating represent a large fraction of the energy demand. In the residential sector this was 62% and 18% respectively of household energy use in 2007 (NRCAN, 2012). Canada's geography and climate are ideally suited for the use of solar energy to meet a substantial fraction of thermal energy needs. One of the major issues associated with renewable energy from sources such as solar energy is the conflicting time dependency of both the availability and the demand of energy. Thermal energy storage (TES) has been an area of interest in research and development for the past few decades due to its ability to offer a solution to the time-dependency problem (Garg et al., 1985). The development of novel solar storage technologies coincides with a growing demand for renewable energy technology and several Canadian jurisdictions have undertaken a proactive approach to renewable energy development at both provincial and municipal levels. For instance, the Halifax Regional Municipality (HRM) Solar-City Project aims to introduce solar thermal hot-water systems to hundreds of homes per year (Halifax Regional Municipality, 2012).

Conventional solar domestic hot water (SDHW) systems collects thermal energy using panels (flat-plate or evacuated tube (Shukla et al., 2013)) and stores thermal energy in sensible heat storage material (*e.g.* water, rock or brick (Sharma et al., 2009)) via heat exchange with the collection heat transfer fluid (HTF). Typical installations use hot water tanks for short-term heat storage. Bédard and Leduc (2011) reported significant system underutilization in conventional SDHW systems during summer months, where the hot water tank storage capacity is saturated and fails to dissipate the heat transferred from the solar collectors. Increasing the storage capacity of a SDHW system for large applications (*e.g.* multi-unit residential buildings) using sensible heat storage materials requires disproportionately large volumes (Scotian Windfields, 2009; Desgrosseilliers et al., 2011). In order to accommodate such an increase, considerable space would be

required, which can be challenging given that most buildings do not have the capability for such retrofitting. However, thermal energy storage is not restricted to solely sensible storage.

Thermal energy can be stored in either as sensible heat, latent heat or thermochemical. In sensible heat storage (SHS), the thermal energy is stored through increasing the temperature of a solid or liquid. A sensible heat storage system relies on the specific heat of the medium, the temperature change and the amount of storage material (Garg et al., 1985). The sensible energy stored is then calculated using the following equation:

$$Q_{sensible} = mC_p(T_f - T_i) \tag{1.1}$$

where m is the mass of the storage medium,C_p is the specific heat of the medium, and T_f and T_i are the final and initial temperatures of the storage medium, respectively.

Latent heat storage (LHS) occurs when a material goes through a phase change (liquid-solid, liquid-gas, and solid-solid). A phase change material (PCM) absorbs and releases energy at nearly constant temperature and it is superior to conventional SHS systems for the reason that it stores 5-14 times more energy than SHS such as water or rock (Abhat, 1983). The amount of latent heat stored in a particular material is dependent on its latent heat of fusion (Δh_m), its mass (m), and the fraction of mass melted (f_m); the amount of latent energy stored can be calculated using the following equation (Sharma et al., 2009):

$$Q_{latent} = mf_m\Delta h_m \tag{1.2}$$

However LHS also consists of some sensible storage that occurs prior and after the phase change takes place, the overall latent and sensible energy stored by a latent heat storage system can be calculated using the following equation (Lane, 1983):

$$Q_{LHS} = m[C_{p,s}(T_{PCM} - T_i) + f_m\Delta h_m + C_{p,l}\left(T_{PCM} - T_f\right) \tag{1.3}$$

where $C_{p,s}$ is the specific heat of the solid PCM, T_{PCM} is the melting temperature of the PCM, and $C_{p,l}$ is the specific heat of the liquid PCM.

Even though LHESS possess higher energy storage densities, the main problem with them remains achieving the desirable heat transfer rates needed for certain applications. The low thermal conductivity observed in most PCMs is the main cause for the low heat transfer rates observed in these systems (Abhat, 1983).

The containment of phase change materials is known as encapsulation. Encapsulation is necessary in order to contain the PCM in its liquid form, provide protection from surrounding conditions and provide additional heat transfer surface to possibly enhanced heat transfer rates in and out of the system. The encapsulation of PCM ranges in scale (*i.e.* bulk, macro, and micro storage). Bulk storage consists of tanks filled with PCM and fitted with heat exchangers. Macroencapsulation includes containers such as metal cans, tubes, spheres, panels, etc. Microencapsulation consists of dispersing small particles of PCMs in an encapsulating solid container in order to increase surface area which in effect increases heat transfer rates (Lane, 1985). A heat transfer medium is required to transfer the energy from the source to the PCM and then to the load, therefore a careful design of the heat exchanger is highly significant to the overall performance of a latent heat energy storage system (LHESS). Figure 1.1 illustrates a simple schematic of a SDHW system with a LHESS. The system shown in Fig. 1.1 consists of bulk encapsulation of a PCM in a cylindrical tank and two simple coil-in-tank heat exchangers (typically used in conventional water-based storage tanks (Li et al., 2014)) used for charging/discharging the storage unit. The hot coil transfers the energy collected from the solar collector, while the cold coil transfers domestic water in order to heat it to meet the residential hot water demand.

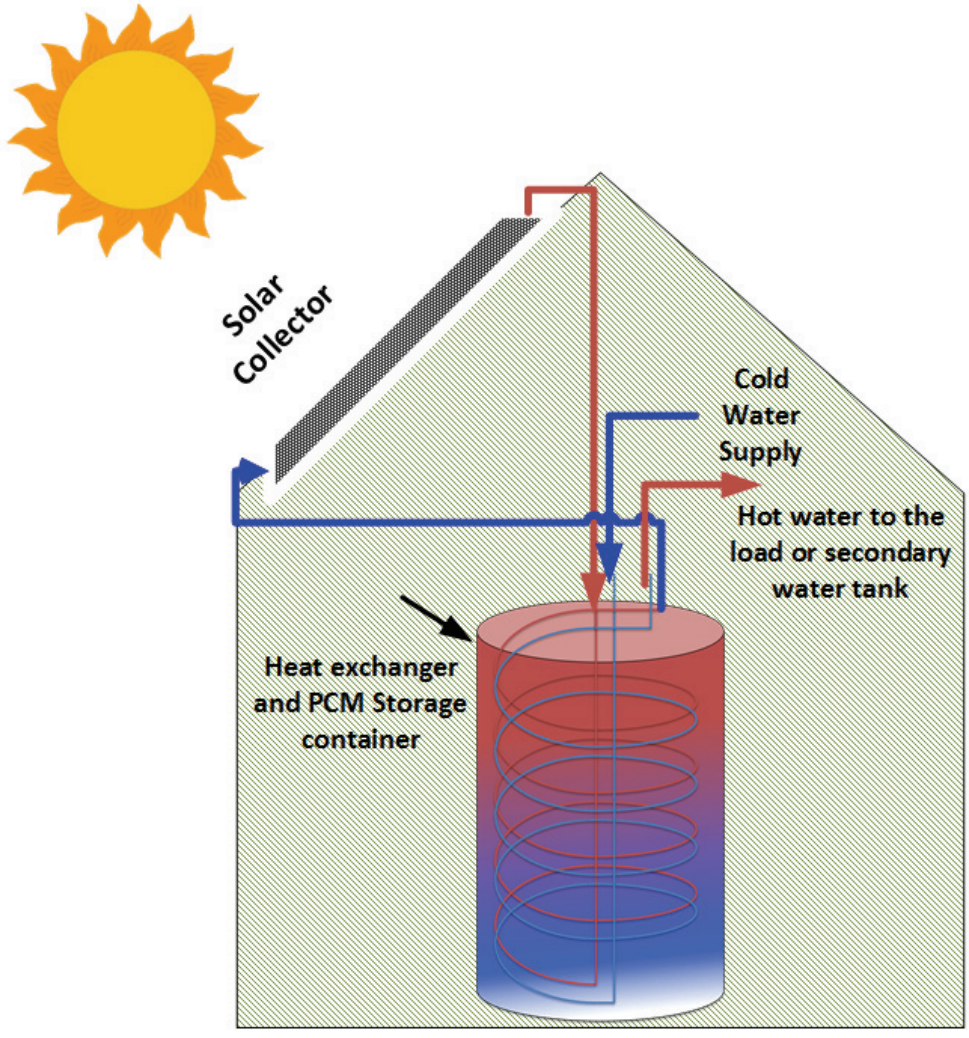

Figure 1.1: Schematic of a SDHW system with a LHESS

1.2 PROBLEM STATEMENT

LHESS possess higher storage capacities than sensible storage system, thus they are capable of storing more energy per unit volume. However, since the availability and demand of energy in SDHW systems is time dependent, the rate at which the energy is transferred/extracted from the storage unit is of great functional importance. Due to the low thermal conductivity of PCM (Abhat, 1983), the rates at which heat is transferred to and from the system do not meet the time restrictions of both the availability and demand of energy, which limits the advantage of the LHESS. With better understanding of the

overall characteristics of the system, it will be possible to identify the limiting factors that impede the commercialization of this storage technology in SDHW systems.

1.3 RESEARCH OBJECTIVES

The objectives of this research project are:

1) Characterizations of the performance of a LHESS.
2) Compare the performance of a coil heat exchanger versus a finned tube heat exchanger.
3) Validate an optimization methodology for a coil heat exchanger design.

Objective 1: Characterize the performance of a LHESS

This aims to experimentally investigate the performance of the LHESS. The important parameters include: heat transfer rates, charging discharging time, phase change behavior of a PCM, under real-time solar conditions and controlled experimental conditions. The real-time solar experimental investigation allows for a seasonal assessment of a functioning LHESS, which is lacking in the literature. Such an investigation is useful since most locations experience seasonal variations in solar radiation. Controlled experimental conditions investigate the effects of various operating parameters (*i.e.* HTF inlet temperature, HTF flow rate) on the performance of the LHESS. In addition, experiments will be conducted to allow a direct comparison between a PCM based storage unit and a water based storage unit, in order to assess the advantages and disadvantages of the LHESS.

Objective 2: Compare the performance of a coil heat exchanger versus finned tubes

The rate at which the heat is transferred to and from the system is a crucial aspect of the overall performance of a LHESS. The heat transfer rate depends on the design of the heat exchanger. The heat exchanger used in a typical solar-water sensible storage system is a helical coil (Shukla et al., 2013). Therefore in order to establish an initial understanding of the system, a helical coil will be used in the LHESS as a baseline measurement of the performance. Subsequently, a finned tube heat exchanger will be

employed in the same experiments in order to compare the performance of a coil versus finned tubes geometry in the LHESS.

Objective 3: Validate an optimization methodology for a coil heat exchanger design

A Fourier number based analysis was used to study the effects of the characteristic length of diffusion on heat transfer rates, melting/solidification time. An optimization method using Fourier number based analysis was developed and used to conduct an experimental validation of the LHESS.

1.4 SCOPE OF THESIS

The background and research objectives of this thesis have been presented in the previous sections. Chapter 2 presents a literature review of LHESS including energy storage materials and their selection criteria, heat transfer in phase change materials, PCM encapsulation, and experimental studies of various geometries and parameters of operation. Heat transfer enhancement techniques are presented with their influence on decreasing charge/discharge time. Chapter 2 also reviews multiple experimental studies conducted under various experimental conditions, and demonstrates that very little work has been published on seasonal evaluation of LHESS under real-time solar conditions.

Chapter 3 presents the theory used in order to assess the performance of the LHESS, both through experimental and theoretical calculations. In addition, the uncertainty propagation associated with the experimental measurements used for these calculations is presented. Chapter 3 also introduces the theory behind the Fourier number based analysis and optimization method.

Chapter 4 presents the experimental setup and the equipment used in addition to the experimental procedures for the various experiments conducted.

Chapter 5 presents the results for the characterization of the LHESS with results from both real-time solar and controlled experimental conditions. Discussion regarding the effects of experimental parameters of operation is also presented. Chapter 5 also

includes the direct experimental comparison of latent versus sensible thermal energy storage.

Chapter 6 presents the results for the comparative study of helical coil versus finned tube heat exchangers. In addition, a comparison of a first prototype coil versus the optimized coil, which was designed using the Fourier number design method, is presented.

Chapter 7 presents the conclusions and recommendations for future work.

CHAPTER 2 LITERATURE REVIEW

2.1 PHASE CHANGE MATERIALS: PROPERTIES AND SELECTION

The wide range of melting/freezing temperatures of various PCMs available allows the technology to be employed in different applications other than SDHW such as: space heating, greenhouses heat recovery, cooling systems (i.e. ice storage), off peak electricity storage systems, etc. Such systems usually vary in performance based on the different influencing parameters such as latent heat of fusion, melting temperature and heat transfer rate. Therefore, a careful selection of the PCM that meets the needs of the application is essential.

Various properties need to be taken into consideration in the selection process of PCM such as kinetic, thermodynamic, physical and chemical properties of the material. Each application requires certain desirable properties in order to employ the material for a specific use.

PCM can be classified into two main categories: organic and inorganic materials. Inorganic materials such as salt hydrates have been extensively studied for their use in latent heat storage applications (Lane, 1983). They cover a wide range of melting temperatures and they are easily available at low costs (Lane, 1983). Salt hydrates have a high heat of fusion and high thermal conductivities which in effect increases the storage density and the heat transfer rates in the storage unit; they also exhibit low volume change which makes them more compatible with wider range of containers (Sharma and Sagara, 2005). However investigations have shown that salt hydrates experience segregation (separation of the salt and water phase) after multiple cycles, in addition to supercooling (supercooling occurs when the material is cooled below its melting point without undergoing solidification) of the liquid PCM without freezing (Abhat, 1983; Lane, 1983; Sharma and Sagara, 2005).

Organic phase change materials include paraffins and non-paraffins such as fatty acids and sugar alcohols. Organic materials have covalent bonds, which makes them less stable at high temperatures. They also crystalize while exhibiting little to no

supercooling which is due to their self-nucleating property (Sharma et al., 2009). Paraffins are the most common organic phase change material used with moderate thermal storage densities (≈200 kJ/kg) (Lane, 1983; Farid et al., 2004). Commercial grade paraffins are a product of petroleum distillation; they are chemically stable, safe, and have a melting temperature range between 23-67 °C (Abhat, 1983; Farid et al., 2004; Sharma and Sagara, 2005). The non-corrosive characteristic of paraffins alongside with their low vapor pressure makes them compatible with metallic containers, however they can cause softening of plastics (Sharma et al., 2009) which is a consideration when designing storage tanks, heat-exchangers, and fluid transfer lines. Paraffins also show little to no degradation in thermal properties after multiple melting/freezing cycles (Sharma and Sagara, 2005). However some undesirable properties are present such as low thermal conductivity and flammability. Low thermal conductivity decreases the heat transfer rate during the freezing cycle, however using finned containers and metallic fillers can enhance the heat transfer rates (Hasnain, 1997; Velraj et al., 1998). Non-paraffins such as fatty acids share similar properties with paraffins with the exception of their incompatibility with certain metals, which is due to their acidic character. Several studies have been carried out on the investigation of the thermal and physical properties of dodecanoic acid (also known as lauric acid) for its use in energy storage applications (Dimaano and Escoto, 1998; Sarı and Kaygusuz, 2002; Sarı et al., 2009; Zuo et al., 2011; Jiao et al., 2012). Lauric acid was studied for its potential use in latent heat storage systems for DSHW applications; its melting range was found to be compatible with the range obtained in solar thermal applications (40°C-50°C) (Murray et al., 2011). It was also shown that lauric acid only undergoes a small volume change (around 8%) and exhibits no signs of degradation even after 500 cycles (Desgrosseilliers et al., 2013). Lauric acid is a non-toxic material therefore it is safe to use in domestic hot water applications (Desgrosseilliers et al., 2011).

Each energy storage application requires certain desirable properties for the PCM, the selection of the material is related to the following desirable properties (Abhat, 1983; Sharma et al., 2009):

i. High thermal conductivity.
ii. Suitable melting temperature that is coordinated with the operating temperature of the application.
iii. High latent heat of fusion.
iv. Low volume change.
v. Limited supercooling and cycling stability.
vi. Compatibility with material of construction and non-toxic and nonflammable material.
vii. Low cost and readily available.

2.2 HEAT TRANSFER IN PHASE CHANGE MATERIALS

A thorough understanding of the heat transfer process in a LHESS is essential in order to develop a well-designed system that adequately meets the requirements of the desired application. Heat transfer during phase change can be categorized into three main modes: conduction dominated, convection dominated or both conduction and convection dominated (Sharma et al., 2009; Agyenim et al., 2010b). During melting, conduction has been shown to be the main mode of heat transfer in the early stages, however convection becomes the main mode once gravity effects become significant (Liu and Groulx, 2014; Murray and Groulx, 2014a; Sciacovelli et al., 2014). During solidification, conduction has been shown to be the main mode of heat transfer (Jesumathy et al., 2014; Liu and Groulx, 2014; Murray and Groulx, 2014a; Rahimi et al., 2014).

Shokouhmand and Kamkari (2013) studied the melting process of dodecanoic acid in a rectangular geometry with two vertical walls (hot and cold wall). The study utilized visualization of the melting process, while the images were processed using MATLAB's image processing toolbox in order to determine the time-based melt front fraction. The measurements of temperatures and the data analysis of the images were used to determine the dominant mode of heat transfer throughout the stages of the melting process. The four stages observed were pure conduction during the early stages,

transition regime at the onset of melting, strong convection and vanishing convection. The intensity of the convection current decreases as the melt front approaches the wall opposite to the heat source.

Since conduction is the dominant mode of heat transfer all throughout the solidification process, the resistance due to conduction between the outer wall temperature of the heat exchanger and the PCM is the limiting factor in the process. Therefore, it can be predicted that an increase in the forced convection resistance due to HTF flow, or the conduction resistance between the inner and outer heat exchanger wall temperatures, would not have a significant effect on the overall heat transfer process.

2.3 LATENT HEAT ENERGY STORAGE SYSTEMS

Latent heat storage systems (LHESS) are not solely dependent on the selection criteria of phase change materials; however they incorporate several other considerations such as the selection of the encapsulation container, the selection of the heat exchanger design, heat transfer enhancement, operating conditions of the system (*i.e.* heat transfer fluid flow rates, operating temperatures and operation modes), and the geometry of the containers holding the PCM. Various studies are found in the literature regarding LHESS in the application of SDHW. Researchers have explored these various parameters affecting the storage systems through both experimental investigations and numerical/analytical analysis. A summary of the findings is presented below.

2.3.1 PCM encapsulation

As was mentioned in section 1.1, encapsulation plays a significant role in the design process of a LHESS. Encapsulation acts as a heat transfer surface, in addition to that it provides protection from ambient conditions and contains the PCM in both its liquid/solid states. Similarly to PCM, Lane (1985) gave a list of criteria for the selection of encapsulent materials (Lane et al., 1978; Lane, 1985):

i. Compatibility with PCM.
ii. Ability to withstand volume changes.
iii. Suitable heat transfer properties.
iv. Provide a vapor barrier to protect the PCM.

v. Reasonably priced and readily available.

Bulk storage is a desirable type of encapsulation due its similarities with conventional sensible storage designs and systems. However, it does have some drawbacks in comparison with the other scales of encapsulations, such as mechanical complexity (*i.e.* more components in the system) and limited application versatility. However it does possess economic benefits due to its larger scale applicability (higher energy density) and it can be used efficiently in larger applications such as commercial and public buildings (*i.e.* apartment buildings, schools, hospitals) (Lane, 1985). The most common type of bulk storage tanks includes a large surface heat exchanger that is imbedded in the PCM (Lane, 1985; Castell et al., 2011; Shokouhmand and Kamkari, 2013; Tay et al., 2013).

2.3.2 Alternative designs in SDHW storage:

The use of LHS in SDHW systems is not exclusive to the system components described in section 1.1. The integration of PCM modules in existing water based storage tank has also been proven to be a beneficial technology in improving the storage performance in SDHW systems (Cabeza and Sole, 2007; Al-Hinti et al., 2010). One study found that the insertion of PCM modules enhanced the storage density and counteracted the major heat loss of the upper layers of water storage tanks (Mehling et al., 2003). However, one study found that the PCM enhanced tanks do not represent a viable solution for SDHW systems: this can be due to the large variation of temperatures inside the tank that may destroy the benefits of the latent heat of PCM with a reduction in sensible heat absorbed (Padovan and Manzan, 2014). Several studies explored the potential of imbedding PCMs directly into the solar collector (Mettawee and Assassa, 2006; Chaabane et al., 2014). Chaabne et al. (2014) studied the effects of directly incorporating a PCM into an integrated collector and storage solar water heater. The PCMs studied were RT42-graphite and myristic acid. The results indicated that the use of PCMs reduced night-time thermal losses. The study also found that myristic acid was a more appropriate PCM than RT42-graphite for this application due to its higher heat of fusion and higher melting temperature

2.4 EXPERIMENTAL STUDIES:

Researchers have carried out various experimental investigations on LHESS over the past several decades. These studies explored several topics such as storage geometries, operating parameters and heat transfer enhancement techniques. A discussion of relevant findings is presented below.

2.4.1 Storage Geometry:

The storage geometry of LHESS is a vital component that affects the system's performance and must be taken into serious consideration during the process of designing a LHESS. The thermal and geometric parameters of the container directly influence the heat transfer characteristics in the PCM and affect the overall performance of the LHESS. Cylindrical (horizontal and vertical) and rectangular geometries are most commonly employed according to a recent survey on published studies (Agyenim et al., 2010b).

Three types of cylindrical PCM containers are studied. The first includes encapsulated PCM in the cylinder with HTF flowing across it (Jones et al., 2006). The second consists of a pipe with HTF flowing inside of it and PCM placed in the annular gap (Agyenim et al., 2010b; Murray and Groulx, 2014b). A study conducted a direct comparison between the encapsulated PCM system and the pipe system taking into consideration the radii of both systems, results indicated that the pipe system recorded a shorter charging time that can be attributed to the smaller thickness of the PCM mass. The pipe system exhibited lower heat loss rates to the environment since the heat source is surrounded by PCM (Mehmet et al., 1997). The third is the shell and tube system, where PCM fills the shell and HTF flows within multiple tubes, this system is used in order to increase heat transfer rates (Ghoneim, 1989). A study compared a single pipe system with a multitube shell and tube system. It was found that the effects of multiple convection cells dominated heat transfer after the onset of natural convections in the shell and tube system as opposed to conductive heat transfer in the single pipe model due to the delay of natural convection. In addition, the temperature gradients recorded in the axial direction for both the pipe and shell and tube systems during the change of phase

were reported to be 2.5% and 3.5% that of the radial direction respectively, which indicates a two-dimensional heat transfer in both systems (Agyenim et al., 2010a).

Several studies on rectangular containers were found in the literature (Solomon, 1979; Hamdan and Elwerr, 1996; Zivkovic and Fujii, 2001). Rectangular containers are used since the solidification/melting front is symmetric at the center of the plate, also the surface area to volume ratio for heat transfer is the largest out of the geometries studied (Zalba et al., 2003). A rectangular container, made of stainless steel, with dimensions of 100 mm wide, 100 mm thick, and 20 mm high was studied experimentally in comparison with a cylindrical container of the same volume (same mass of PCM), results showed that the rectangular container required only half of the melting time of that of the cylindrical container (Zivkovic and Fujii, 2001).

2.4.2 Operating parameters:

Various operating parameters can be modified in order to optimize the operation and performance of the LHESS. These parameters include the HTF inlet temperature, and flow rate (Agyenim et al., 2010b).

Several experimental studies showed that an increase (during charging) or decrease (at discharge) of the HTF inlet temperature results in an increase in heat transfer rates, thus reducing charging/discharging times (Sarı and Kaygusuz, 2002; Nomura et al., 2013; Liu and Groulx, 2014; Murray and Groulx, 2014a). Jesumathy et al. (2014) conducted an experimental study on paraffin wax in a horizontal double pipe LHESS, in which an increase in the HTF inlet temperature from 70 to 74 °C showed a decrease of total melting time by 31%. However, an experimental study on a LHESS conducted by Sarı and Kaygusuz (2002) in which dodecanoic acid filled the annular space between the PCM container and the HTF pipe, showed that an increase of the HTF inlet temperature by 4 °C decreased the total melting time on average by 21%. The effects of HTF inlet temperatures during solidification were also studied. Jesumathy et al. (2014) showed that a decrease of the HTF inlet temperature from 42 to 38 °C resulted in a decrease for total solidification time by 35% (Jesumathy et al., 2014). Whereas, Sarı and Kaygusuz (2002) showed that a decrease of 4 °C showed a decrease of 20% for total solidification time (Sarı and Kaygusuz, 2002). Rahimi et al. (2014) studied the effects of the HTF

inlet temperature in a fin and tube heat exchanger LHESS, the results indicated that melting times decrease much more significantly with a 10 °C increase in the HTF inlet temperature starting from 50 to 60 °C as opposed to an increase from 60 to 70°C (Rahimi et al., 2014). Therefore it can be observed that moderate changes in HTF temperature can have significant impact on LHESS system performance.

The effects of the HTF flow rate on charging and discharging were studied in several studies (Sarı and Kaygusuz, 2002; Jesumathy et al., 2014; Liu and Groulx, 2014; Murray and Groulx, 2014a). The increase in flow rate directly increases the coefficient of heat transfer due to forced convection, which in effect decreases its thermal resistance. Since the melting process is dominated by conduction during its early stages, the increase in flow rate does not have any effect on heat transfer rates. However as the PCM starts to melt, an increase of flow rate increases heat transfer rates and decreases melting times due to the role of natural convection (Jesumathy et al., 2014; Liu and Groulx, 2014; Murray and Groulx, 2014a). Studies have shown that an increase of flow rate during solidification did not have any significance on the heat transfer rates or discharging time, which is attributed to the conduction dominated heat transfer process (Murray and Groulx, 2014a; Rahimi et al., 2014).

2.4.3 Heat transfer enhancement techniques:

Even though higher storage densities are available in LHESS, the low thermal conductivity of most PCM necessitates heat transfer enhancement techniques in order to improve the rates at which the heat is stored/extracted from the system. The increase of heat transfer rates will allow the system to be charged/discharged in the desired time for SDHW applications (Velraj et al., 1998).

Several methods of heat transfer enhancements in LHESS were studied such as: the use of various types of extended fins (Ilken and Toksoy, 1993; Khalifa et al., 2014; Liu and Groulx, 2014; Murray and Groulx, 2014b; Rahimi et al., 2014; Sciacovelli et al., 2015), inserting a graphite or metal matrix within the PCM (Py et al., 2001; Cabeza et al., 2002; Mills et al., 2006), micro-encapsulation of PCM (Alvarado et al., 2007; Zeng et al., 2009), and carbon fiber brushes with high thermal conductivity (Fukai et al., 2003).

The use of fins is an inexpensive and simple method to enhance heat transfer. Fins are usually extended in the side of the PCM as opposed to the HTF in order to increase fin efficiency. Fins are usually either longitudinal or circular in the case of a cylindrical geometry. An experimentally validated numerical study developed a CFD fin optimization method that yielded Y-shaped fins on cylindrical tubes that were capable of increasing the LHESS efficiency by 24% (Sciacovelli et al., 2015).

A study compared a heat pipe with no fins, circular fins, and longitudinal fins. Longitudinal fins were found to give the best performance with increase thermal response for both melting and solidification (Agyenim et al., 2009). Longer fins were found to increase solidification rates, in addition to increasing the natural convection heat transfer coefficient (Ilken and Toksoy, 1993; Castell et al., 2008). Khalifa et al., (2014) conducted a study in order to compare the effect of axial fins relatively to a bare pipe, and showed that the addition of axial fins to a bare heat pipe with an outer diameter of 8 mm increased the energy extracted from the PCM by 86%. An experimental study examined the effects of straight and angled fins; the results showed that the configuration of the fins was a significant parameter only during melting when the HTF inlet temperature was 60 °C (Liu and Groulx, 2014).

The effects of impregnating paraffin with a graphite matrix were studied; various results indicated that the composite matrix substantially increased heat transfer (Py et al., 2001; Mills et al., 2006). One of the studies showed an increase in thermal conductivity by 20 to 130 times (Mills et al., 2006). Another study analyzed the effects of inserting copper pieces, stainless steel pieces and graphite matrix impregnated with PCM. The results showed that stainless steel pieces did not significantly enhance heat transfer rates, while copper pieces and the graphite matrix showed useful heat transfer enhancements. The study concluded that the addition of metal pieces in the PCM is only useful in the case of highly conductive materials as in the case of copper and the graphite matrix. However, the graphite matrix has an advantage over loose packing of the metal pieces by forming a consolidated block with many uninterrupted heat flux paths (Cabeza et al., 2002). These techniques indicate that it is possible to address the limitations of heat transfer with PCM through the material itself.

A study analyzed the effects of adding carbon-fiber brushes on the shell side of a heat exchanger in order to improve heat transfer rates, and results showed that discharge rates increased by 30% by using brushes with one volume percent compared to using no fibers. It was found that the addition of brushes blocked natural convection during charging, however the charging rates were still 10-20% higher to using no fibers. It is therefore evident that the increase of thermal conductivities makes up for the reduction in the convective heat transfer rate (Fukai et al., 2003).

2.5 SUMMARY

As shown, several studies have explored various aspects of LHESS and PCM as a heat storage medium, however the most significant findings relevant to this thesis are presented as follows:

- The literature indicates that organic PCMs such as lauric acid are suitable for use in SDHW.
- The use of coil-in-tank or multiple coils has not been studied in LHESS as a way of increasing heat transfer area.
- The increase of the HTF flowrate during melting decreases charging time, however it was found that it did not have any effect on discharging time.
- The increase of HTF inlet temperature during charging decreases charging times.
- A direct experimental comparison between sensible and latent storage material using the same storage container and heat exchanger could not be found in the literature.
- Real-time solar seasonal evaluation of a LHESS have not been widely reported or published.

CHAPTER 3
THEORY & METHODOLOGY

3.1 THEORETICAL STORAGE CAPACITY

The theoretical storage capacity of a LHESS is dependent on the thermophysical properties and quantity of PCM. Knowing the theoretical storage capacity of a LHESS provides a baseline against which experimental results can be compared. Equation (1.1) shows the relationship between the sensible storage capacity and the specific heat of the storage material and the temperature difference from the material's initial state to its final state. Latent heat storage capacity is given in Eq. (1.2), however it includes only the latent heat storage capacity when a material has reached its phase change temperature. The combined latent and sensible heat storage capacity of a LHESS, as given in Eq. (1.3), provides the theoretical storage capacity of the system, which acts as a reference point for comparison with experimental results. A comparison of the storage capacities of latent heat storage systems versus sensible storage systems is highly dependent on the temperature range at which the system operates. Chapters 5 and 6 compare the theoretical storage capacities to the experimental storage capacities in order to evaluate the reasonability of the results.

3.2 ANALYSIS OF EXPERIMENTAL DATA

The experimental characterization and analysis of a LHESS is based on calculating the system's experimental capacity for storing/releasing thermal energy, as well as the rates at which the system stores/releases the energy.

Considering a general LHESS such as the one shown in Fig. 1.1, with two coil heat exchangers for charging and discharging the system, an experimental investigation can be conducted by measuring the hot and cold HTF inlet and outlet temperatures, as well as their flow rates. Based on these measurements, the power input $\dot{Q}_{input}$, and power output $\dot{Q}_{output}$ can be calculated using Eqs. (3.1) and (3.2) respectively:

$$\dot{Q}_{input} = \dot{m} Cp_{Hot\_HTF}\left(T_{H,in} - T_{H,out}\right) \tag{3.1}$$

where $\dot{m}$ is the mass flow rate of the HTF, Cp_{HTF} is the specific heat capacity of the HTF, $T_{H,in}$ is the inlet temperature of the hot HTF, and $T_{H,out}$ is the outlet temperature of the hot HTF.

$$\dot{Q}_{output} = \dot{m} Cp_{Cold\_HTF}\left(T_{C,out} - T_{C,in}\right) \tag{3.2}$$

where $T_{C,out}$ is the outlet temperature of the cold HTF, and $T_{C,in}$ is the inlet temperature of the cold HTF.

Assuming that the tank is well insulated, the amount of heat loss will be insignificant and it can be considered that all the energy added to the tank stays in the tank. This leads to calculating the amount of energy stored Q_{input} and released Q_{output} per time interval of measurement Δt using Eq. (3.3).

$$Q_{input\backslash output} = \Delta t \dot{Q}_{input\backslash output} \tag{3.3}$$

The cumulative energy stored $Q_{c,stored}$ or recovered $Q_{c,recovered}$ can be calculated by summing the energy input and output over the overall time intervals during the charging/discharging period, it is expressed by Eq. (3.4).

$$Q_{c,stored\backslash recovered} = \sum_{t=0}^{t=t_{final}} \Delta t \; \dot{Q}_{input\backslash output} \tag{3.4}$$

The cumulative energy calculated can be used to assess the overall performance of the system, which can then be compared to the theoretical storage capacity expected from a certain amount of PCM mass.

3.3 UNCERTAINTY ANALYSIS

Bias uncertainty is the dominant type of uncertainty in the measurements and calculations done in this work. Due to the offset uncertainties in the measurements provided by the thermocouples and flow meters, a propagation of uncertainty is required in order to estimate the uncertainty in the calculation of the amount of energy stored/recovered. The following calculations show the method of propagation of uncertainty that can be applied for Eq. (3.3).

$$Q = t\dot{m}C_{p_{HTF}}\Delta T \pm \delta_Q \tag{3.5}$$

where Q is the energy input/output, ΔT is the HTF inlet/outlet temperature difference, and δ_Q is the uncertainty in the energy input/output expressed as:

$$\delta_Q = \sqrt{\left(\frac{\partial Q}{\partial \dot{m}}\delta_{\dot{m}}\right)^2 + \left(\frac{\partial Q}{\partial T_{out}}\delta_{T_{out}}\right)^2 + \left(\frac{\partial Q}{\partial T_{in}}\delta_{T_{in}}\right)^2} \tag{3.6}$$

where $\delta_{\dot{m}}$ is the flow meter uncertainty, $\delta_{T_{out}}$ and $\delta_{T_{in}}$ are the thermocouple uncertainties for the HTF outlet and inlet temperatures, respectively.

The uncertainty in temperature measurements for the hot and cold HTF can vary; therefore separate uncertainty propagation may be required. Assuming $C_{p_{HTF}}$ to be accurate, $\delta_{Q_{input}}$ and $\delta_{Q_{ouput}}$ can be expressed by Eqs. (3.7) and (3.8).

$$\delta_{Q_{input}} = tCp_{Hot,HTF}\sqrt{(\Delta T\delta_{\dot{m}})^2 + \left(\dot{m}\delta_{T_{H,out}}\right)^2 + \left(-\dot{m}\delta_{T_{H,in}}\right)^2} \tag{3.7}$$

$$\delta_{Q_{ouput}} = tCp_{Cold,HTF}\sqrt{(\Delta T\delta_{\dot{m}})^2 + \left(\dot{m}\delta_{T_{C,out}}\right)^2 + \left(-\dot{m}\delta_{T_{C,in}}\right)^2} \tag{3.8}$$

where $\delta_{T_{H,out}}$, $\delta_{T_{H,in}}$, $\delta_{T_{C,out}}$ and $\delta_{T_{C,in}}$ are the thermocouple uncertainties for the hot and cold HTF outlet and inlet temperatures, respectively. The derivations of Eqs. (3.7) and (3.8) are shown in Appendix A.

This analysis is used as the methodology for data analysis in the results section in chapters 5 and 6 in order to quantify the uncertainty in the calculations conducted for each charging/discharging process during the experimental investigation. The specific uncertainty of the sensors used in the temperature and flow measurements is described in the experimental setup in chapter 4.

3.4 FOURIER NUMBER ANALYSIS

3.4.1 Fourier number

The Fourier number is the ratio of the heat conduction rate to the rate of thermal energy storage in a solid for a given volume element (dimensionless time). The Fourier number is dependent on the physical properties of the material used and it is defined by the following equation (Incropera et al., 2011):

$$Fo = \frac{k}{\rho C_p}\frac{t}{L^2} = \frac{\alpha t_c}{L^2} \tag{3.9}$$

where k is the thermal conductivity, C_p is the specific heat (liquid, or solid), ρ is the density, t_c is the characteristic time, α is the thermal diffusivity, and L is the characteristic length.

Due to the transient nature of conduction heat transfer in PCMs, it is challenging to determine the charge/discharge state of a LHESS. The Fourier number expresses the penetration of heat through the characteristic length of a solid in a given period of time, thus a larger value is indicative of deeper penetration of the material (Singh and Heldman, 2014). The choice of the physical properties of the PCM at a particular phase (*i.e.* liquid or solid) in the calculation of *Fo* reflects the physical trend of a given phenomenon (Liu et al., 2014). For instance, the choice of the solid physical properties indicates the relative time necessary for the PCM to fully solidify across the characteristic length.

3.4.2 Scale-up design method

The Fourier number analysis could be extended to develop a scale-up method to determine the optimum characteristic dimensions of the storage tank and heat exchanger required to recover the stored energy within a desired time.

The proposed method requires an initial characterization of the storage tank in order to determine experimentally the time required to recover the stored energy for a certain characteristic length. The method aims to provide a relative quantification of the value of *Fo* at the final state of the discharge process, in order to determine the optimum characteristic length that meets the time limitations of particular applications. The Fourier number can be calculated based on the characteristic length, thermal diffusivity (α) and the observed experimental discharge time under specific experimental conditions (*i.e.* HTF inlet temperatures, flow rates). The hypothesis supporting this method suggests that in order to achieve the same final state during a shorter period of time (under the same experimental conditions), the experimentally obtained value of *Fo* has to be fixed, while substituting the characteristic time with the desired time. Therefore, this method allows for an experimental evaluation of the maximum allowed characteristic length required to meet time restrictions.

Identifying the relation between the characteristic length and the characteristic time makes it possible to develop a heat-exchanger design method that utilizes a modular approach in order to meet time restrictions. In the case of the coil-in-tank design, a modular approach would consist of hypothetical small tanks embedded in a large tank. Each hypothetical tank would have its respective coil penetrating the maximum characteristic length, therefore making it possible to discharge the system at a desired rate.

Note that this method is only suggested as an analogy in order to represent the limiting factor, which is the heat diffusion during the discharge process. Hence, it is not an analytical approach to the problem of phase change; it is an analogy that utilizes an experimentally determined Fourier number as a reference point in order to identify the state of the PCM during the discharge process.

3.4.3 Uniformity of heat diffusion

In the case of multiple heat transfer directions from the heat transfer surface to the PCM, several characteristic lengths are defined. Consequently, *Fo* values differ in each direction, causing variations in the charge/discharge state of the PCM throughout the storage volume. In order to achieve uniform diffusion in all directions, the values of *Fo* must be equated in all directions. Therefore, the uniformity of heat diffusion can be achieved by equating the characteristic lengths. For instance, when considering the heat diffusion in a coil-in-tank LHESS as shown in Fig. 3.1, there are three directions for heat diffusion: planar, cylindrical, and annular.

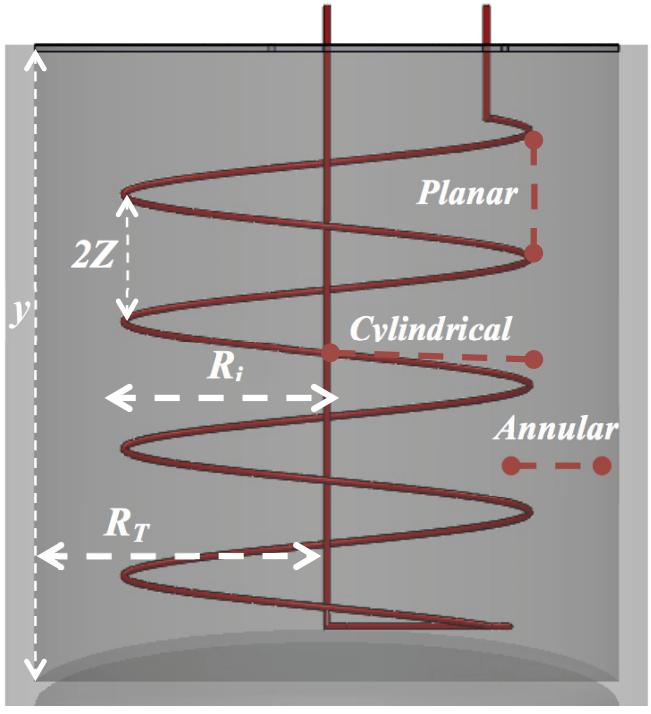

Figure 3.1: Schematic of heat diffusion directions in a coil-in-tank design

The characteristic length is defined as the ratio of the volume of the body to the area of the surface. The characteristics lengths L_1, L_2, and L_3 for planar, cylindrical, and annular are defined in Eqs. (3.10), (3.11) and (3.12), respectively.

Planar: $L_1 = \frac{Z \times (2Ri)^2}{(2Ri)^2} = Z$ (3.10)

Cylindrical: $L_2 = \frac{\pi R_i^2 \times y}{2\pi R_i \times y} = \frac{R_i}{2}$ (3.11)

Annular: $L_3 = \frac{\pi(R_T^2 - R_i^2) \times y}{2\pi R_i \times y} = \frac{R_T^2 - R_i^2}{2R_i}$ (3.12)

where Z is half the pitch of the coil, y is the height of the cylindrical volume, R_i is the inner radius of the coil, and R_T is the radius of the storage tank. As it can be seen, L_1 is independent of L_2 and L_3, therefore once L_2 and L_3 are equated; the obtained value could be assigned for L_1. The obtained relation by equating L_2 and L_3 is given in Eq. (3.13):

$$R_i = \frac{1}{\sqrt{2}} R_T \quad (3.13)$$

Therefore, the sizing of the coil heat exchanger in LHESS can be more deliberate to achieve uniform heat diffusion in order to avoid sensible overcharging in certain parts of the tank.

CHAPTER 4 EXPERIMENTAL SETUP & PROCEDURE

4.1 GENERAL EXPERIMENTAL SETUP

An initial LHESS was built in the Applied Energy Research Lab (AERLab) at the Nova Scotia Community College (NSCC), as part of a collaboration with the Lab of Applied Multiphase Thermal Engineering (LAMTE) and the department of Chemistry at Dalhousie University. An experimental setup was constructed using a cylindrical well-insulated tank filled with PCM and thermocouples to monitor the PCM's thermal behavior. The original purpose of the system was to conduct an experimental investigation under real-time solar conditions using the solar thermal facilities available at NSCC. However, further testing generated interest in characterizing the LHESS under controlled experimental conditions too. The validation of the Fourier number analysis (section 3.4) required a second tank (Tank B) with the initial tank (Tank A) as a reference. Therefore, a second LHESS was built to validate the Fourier number design method and test out multiple heat exchangers. Figure 4.1 shows the general experimental setup for both LHESS which includes all the common components present in both setups.

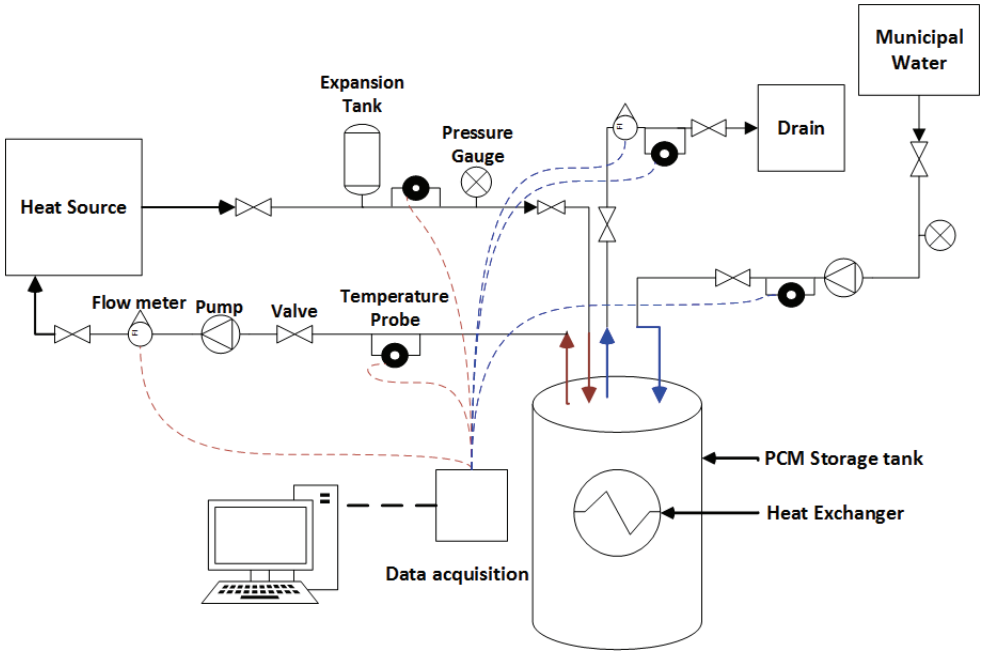

Figure 4.1: General experimental setup for the LHESS (Tank A & Tank B)

4.2 EXPERIMENTAL SETUP: TANK A

The PCM storage tank was fabricated by modifying a conventional residential hot-water tank to half of its vertical dimension. Aviation snips were used to remove the outer sheet metal shell. The insulation was removed in a small band and then an angle grinder was used to cut the internal tank in two. The bottom half was used as the main storage container for the LHESS. The other half of the tank was filled with water and used for experiments of direct comparison of PCM versus water storage. The resulting PCM tank was a well-insulated cylindrical steel tank measuring 52 cm (20.47 in.) long by 46 cm (18.11 in.) in diameter and had a volume of 60 L. The tank was filled with 60 kg of PCM. An insulating cap was made of expanded polystyrene wall insulation and fitted to the tank. Holes were drilled in the cap to allow heat exchanger tubes and thermal probes to pass through. Two copper tubing coils were embedded in the tank in order to charge/discharge the PCM independently, in order to avoid mixing the HTFs used during charging/discharging. The coils were made from 0.635 cm (1/4 in.) nominal diameter copper tubing coiled into two concentric helices. The coils had the following characteristics: 400 cm length, 32 cm diameter, 10 cm pitch and 4 turns. The pitch was

maintained using PVC spacers. The coils sit on top of each other with a radial distance of approximately 5 cm at the entrance of the tank as shown in Fig. 4.2.

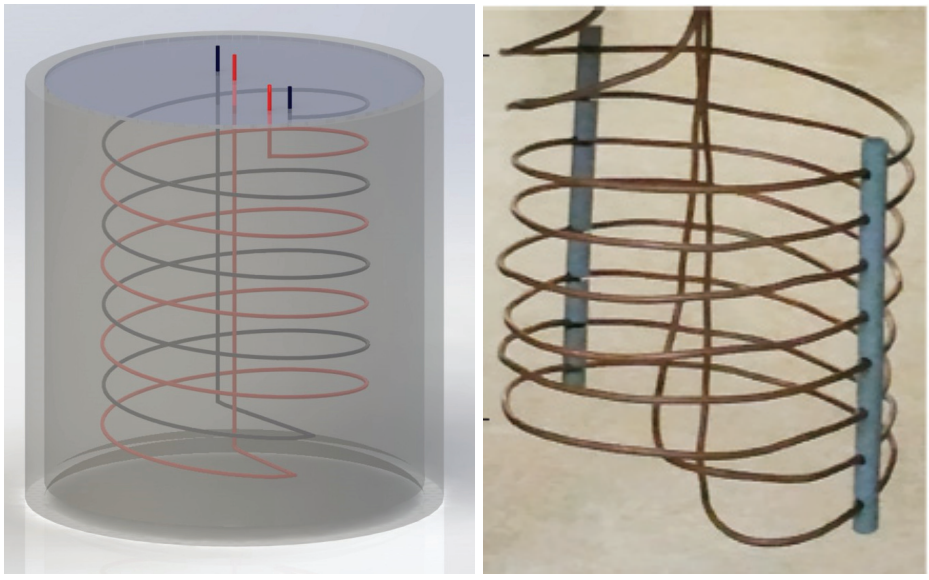

Figure 4.2: left: 3D rendering of tank A; right: A photograph of the coils prior to insertion

4.2.1 Real-time solar setup

The layout of the experimental setup is the same as the general setup shown in Fig. 4.1. A flat-plate solar collector was used as the heat source for the real-time solar experiments. The real-time solar system setup consisted of: ½ in. NPT brass pipes, a Laing D5-710B circulating pump, expansion tanks (Watts Regulator ETX-15 and Bell & Grove HFT-15 for water loop and solar loop respectively), relief valves, Blue-White F-400 acrylic variable area flow meter (0.5-5 L) with a reading uncertainty of ±3%, analog pressure and temperature gauges, and a custom PCM tank with two integrated copper-coil heat exchangers. Figure 4.3 shows a photograph of the experimental setup used for real-time solar testing.

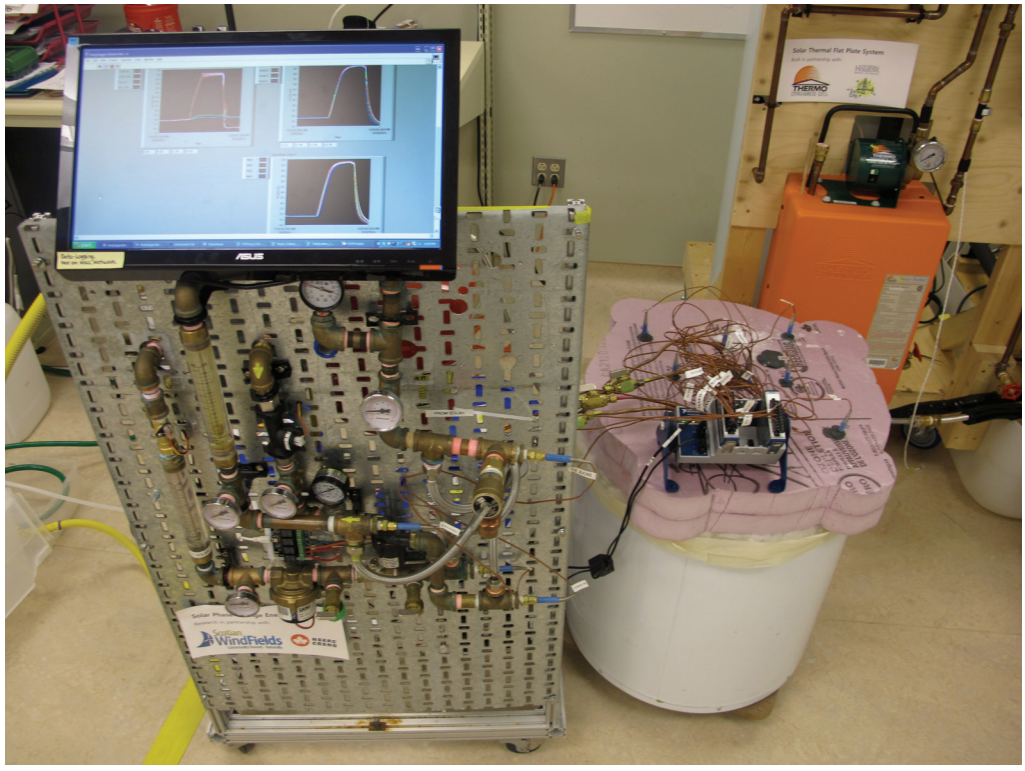

Figure 4.3: A photograph of the experimental setup of Tank A

A Thermo Dynamics Ltd. MicroFlow™ S-32 flat-plate solar collector mounted on a due south orientation with a 45° tilt-angle was used as the solar energy heat-source for the experiments. The collector had a gross surface area of 2.98 m^2 with an aperture area of 2.78 m^2. The initial experimental location was subject to early morning and late-day shading. In June 2014, the experimental equipment was relocated to an open, unshaded location to provide data on LHESS operation under ideal solar conditions. Figure 4.4 shows both collectors at the two locations. Solar insolation was measured using an Apogee sp-215 in real-time with the operation of the LHESS.

Figure 4.4: Top: Ground location (shaded), bottom: Roof location (unshaded)

A glycol and water mixture (40% ethylene glycol) was used as the heat-transfer fluid (HTF) in the solar loop. The Hot HTF enters through the straight copper section and therefore is at its warmest at the bottom of the tank first. Hot HTF is circulated through one coil in order to charge the system, while cold HTF (municipal water) is circulated through the other coil in order to discharge the system. The cold HTF enters through the coiled part (top of the tank) and leaves through the straight copper section. Thermophysical properties of these HTFs are presented in Tables 4.1 and 4.2.

Table 4.1: Thermophysical properties of water (Incropera et al., 2011)

T (◦C)	ρ (kg/m^3)	$\mu \times 10^3$(kg/m·s)	k(W/m·K)	c_p (J/kg·K)	Pr
10	999.70	1.2995	0.5869	4194.1	9.2860
15	999.10	1.1360	0.5953	4188.5	7.9910
60	983.19	0.4630	0.6535	4184.8	2.9650
70	977.76	0.4004	0.6623	4192.0	2.5340
80	971.79	0.3509	0.6698	4200.1	2.2010

Table 4.2:Thermophysical properties of 40% glycol/60% water mixture (ASHRAE Handbook, 2009)

T (◦C)	ρ (kg/m^3)	$\mu \times 10^3$(kg/m·s)	k(W/m·K)	c_p (J/kg·K)	Pr
10	1064.8	4.0387	0.3753	3414.1	36.738
15	1062.7	3.3814	0.3805	3451.8	30.674
60	1040.9	1.1699	0.4099	3602.4	10.281
70	1033.9	0.9508	0.4151	3640.1	8.3374
80	1028.3	0.8268	0.4177	3671.5	7.2670

4.2.2 Controlled experimental conditions setup

A 43 L 'Space-saver' 1.5 kW electric hot-water tank was utilized as the heat source for testing under controlled experimental conditions. The controlled experimental setup consisted of the same main components present in the real-time solar setup. However, in order to achieve higher flow rates, a Grundfos ALPHA™ (ALPHA 15-55F) pump was used for water circulation. A ball valve was used in order to throttle and control the HTF flow rates. Flow rates of 1.1, 1.5 and 2.5 L/min were tested, which are within the range of recommended flow rates of SDHW application (Bertram, 1981). An external digital temperature controller (Ranco ETC) was used in order to set the temperature on the water tank to the desired temperature of the HTF. The HTF was operated at three temperatures: 60, 70 and 80 °C.

A turbine pulse flowmeter (Adafru-Liquid Flow Meter 833 - Brass ½ in.) was used to measure flow rate with a reduced reading uncertainty after calibration of ±3%. The flow meter was connected to a pulse counter (NI 9235 module), which was inserted in a NI CompactDAQ 4-Slot USB Chassis (NI cDAQ-9174). The pulse counter counts the frequency signal from the flow meter (pulse/sec), which can be converted by knowing that the flow meter gives 485 pulses/L. The flow meter was calibrated by determining the time required to fill a 3 L vessel using various flow rates.

During the experiments with controlled experimental conditions, water was used as the HTF for charging/discharging, entering through the same coil during both processes. The HTF enters through the coiled part (top of the tank) and leaves through the straight copper section. Since the same coil is used for both processes, a brass tee was used to allow for pipe sections from the hot water tank and the municipal water to be connected to the inlet of the coil. Solenoid valves in each section were used in order to open or close depending on whether the system is being charged or discharged. The solenoid valves were connected to an electromechanical relay module (NI 9481), which allowed for operation from LabView.

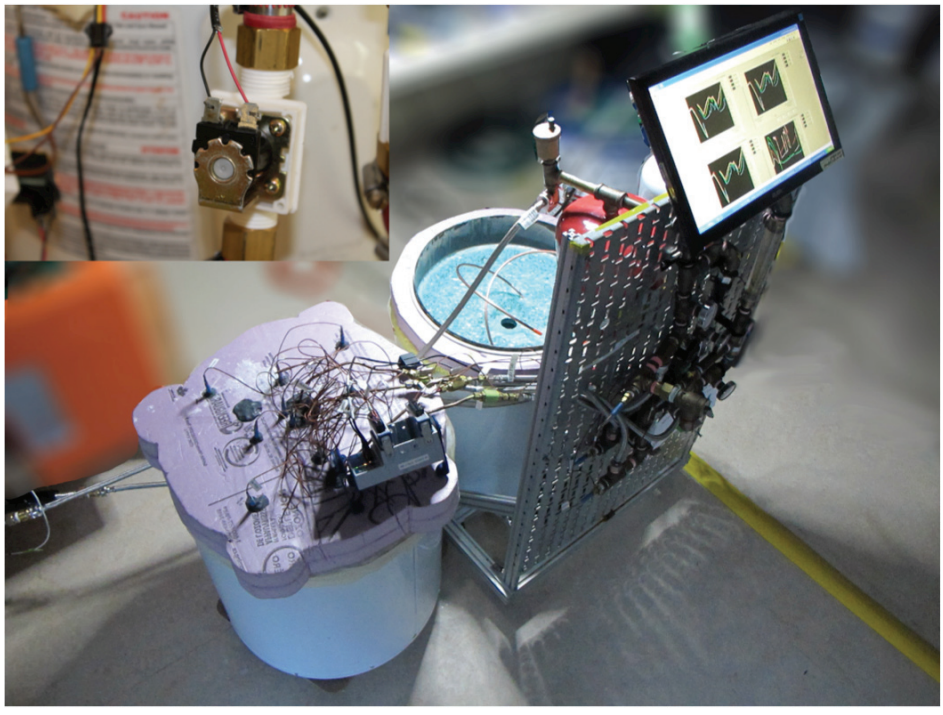

Figure 4.5 Picture of the controlled experimental setup of Tank A and solenoid valve

4.2.3 Temperature Measurements: Tank A

Twelve type-T thermocouples (T1-T12) were located within the PCM as shown in Fig. 4.5, while four type T- thermocouples (T13-T16) were located at the inlets/outlets of the coils in order to measure the temperatures of the HTFs. The thermocouples were placed at three different radial positions (2, 11.5 and 21 cm). Each radial position had four depths (10, 20, 30 and 45 cm ± 2.5 cm) and was spaced 90° from the others.

Due to the dome shape of the bottom of the tank, the deepest probes had slightly uneven lengths (±2.5 cm) at different radial positions. The inner probes (T1-T4) were spaced 2 cm from the point located midway between the two central heat exchanger tubes, therefore they were not exactly centrally located in order to accommodate the HTF lines (see Fig. 4.5).

All thermal probes were T type, copper-constantan, thermocouples housed in stainless steel sheaths of 1/16 in. (0.159 cm) in diameter in the tank and 1/8 in. (0.3175 cm) in the HTF lines. Two thermocouple input modules, NI 9213, and NI 9211, were added to the National Instruments NI-cDAQ-9174 CompactDAQ 4-Slot USB Chassis to record data.

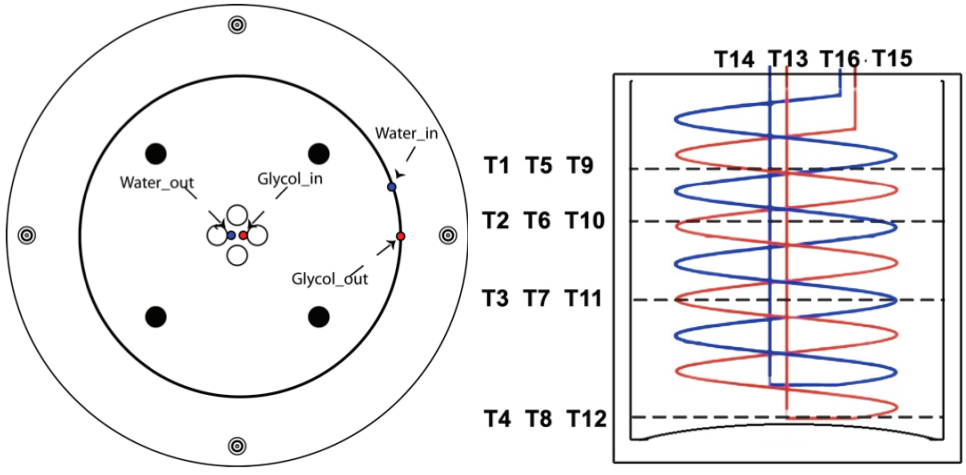

Figure 4.6: Top view and right view of the tank with locations of thermocouples. The ○ symbol represents the radial position of T1-T2-T3-T4, (shifted off-center slightly to accommodate HTF lines). The ● symbol represents the radial position of T5-T6-T7-T8. The ◎ symbol represents the radial position of T9-T10-T11-T12.

4.3 EXPERIMENTAL SETUP: TANK B

As mentioned earlier, in order to determine the validity of the Fourier analysis scale up method, a second tank with different characteristic dimensions was required. Tank B was fabricated by modifying a small conventional residential hot-water tank through an angle grinder to cut off the top of the tank. Tapped holes were inserted into a thin metal sheet in order to allow for the insertion of compression fittings for temperature probes. Insulation was placed at the top after inserting the probes. Tank B is a well-insulated cylindrical tank 43.5 cm long by 32 cm in diameter and has a volume of 30 L. The tank was filled with 25 kg of PCM. Two heat exchangers were used in Tank B sequentially: coil heat exchanger and finned tubes. The experimental setup of Tank B is precisely the same as the one utilized in the controlled experimental conditions setup described in section 4.2.2.

4.3.1 Coil heat exchanger

A coil heat exchanger was used to allow for comparison with Tank A. The coil dimensions were designed based on the heat uniformity method demonstrated in section 3.4.2. The coil was made from 0.635 cm (1/4 in. nominal) diameter copper tubing coiled into a concentric helix. The coil had the following characteristics: 2.6 m length, 21 cm diameter, 10 cm pitch and 4 turns. The coil heat exchanger was used to compare the results from Tank A and evaluate the effects of the characteristic length of diffusion on discharge times and heat transfer rates. The tank had two holes on the side, which were used for the inlet and outlet. Two valves were used to plug the holes, while having a flare fitting inside the tank in order to seamlessly change heat exchangers. The HTF enters at the top of the tank through the coiled part and leaves through the straight copper section as seen in Fig. 4.8. Therefore it is at its warmest at the top of the tank first during charging, and coldest during discharging; which is the same as the controlled experiments conducted on tank A using the water coil. Figure 4.7 shows a 3D rendering of Tank B with the coil heat exchanger. Figure 4.8 shows photographs of Tank B, the coil heat exchanger, top metal sheet and the compression fittings during the building stage.

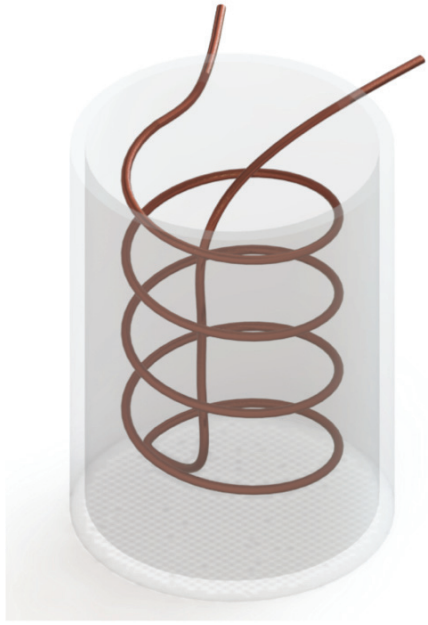

Figure 4.7: 3D Rendering of Tank B with coil heat exchanger

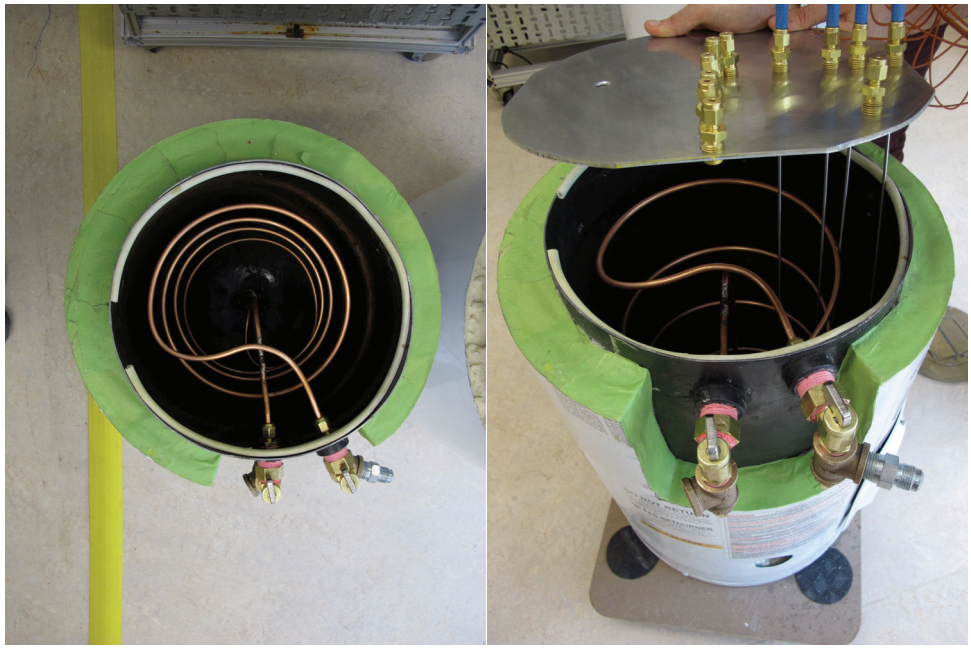

Figure 4.8: Photographs of Tank B with coil heat exchanger during the building stage

4.3.2 Temperature measurements: Coil heat exchanger

Thirteen type-T thermocouples were located within the PCM as shown in Fig. 4.9 while two type-T thermocouples were located at the inlets/outlets of the coil in order to measure the temperatures of the HTF. The thermocouples placement in Tank B differed from the one for Tank A. The comparison conducted between Tank A and B was focused mainly on the energy analysis and heat transfer rates in the tank. Therefore the difference in the thermocouples' locations in the two tanks is not an issue for the purpose of this work. The thermocouples were located at five various radial positions, and four depths. With the addition of one probe that was located very close to the edge and at the very bottom of the tank where the PCM would be expected to melt last.

The nomenclature for the thermocouples was chosen to be R*x*D*y*, with *x* as the number of the radial position (*i.e.* 1: closest to the center, 5: closest to the edge), and *y* as the number of the depth position (*i.e.* 1 as the shallowest, and 4 as the deepest). The spatial distribution consisted of measuring various combinations of the radial and axial positions.

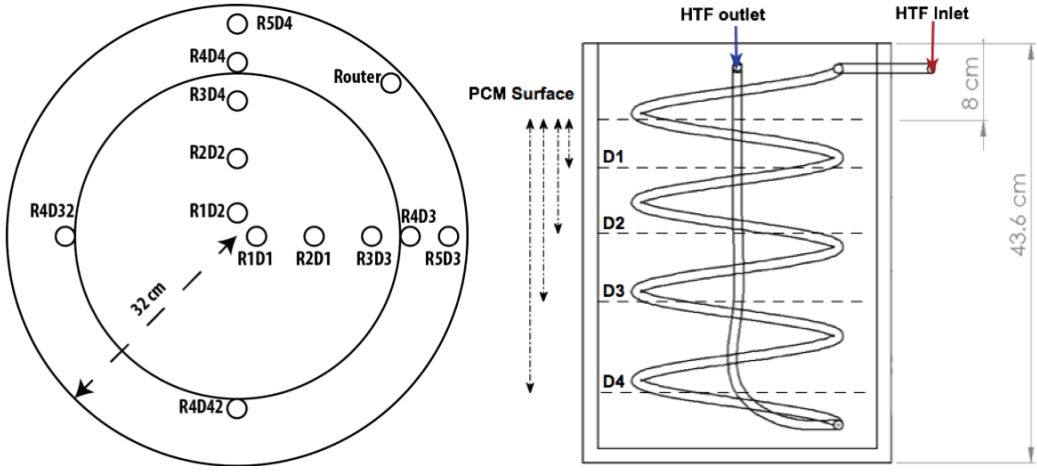

Figure 4.9: Top view and back view of Tank B (coil) with thermocouple locations

Table 4.3 presents the thermocouple locations in term of the radial (relative to the center) and the axial position (relative to the surface).

Table 4.3: Radial and axial positions used for Tank B: Coil Heat Exchanger

Number	R(Radial Position)	D (Depth)
1	1.27 cm (0.5 in.)	5.10 cm (2 in.)
2	5.10 cm (2 in.)	12.7 cm (5 in.)
3	8.89 cm (3.5 in.)	20.32 cm (8 in.)
4	11.43 cm (4.5 in.)	30.48 cm (12 in.)
5	13.97 cm (5.5 in.)	----------

4.3.3 Finned tubes heat exchanger

A series of four 1.58 cm (1/2 in. nominal) diameter copper tubes with rectangular longitudinal fins were used in Tank B. Each tube had the following characteristics: 1.58 cm (1/2 in. nominal) diameter, 5.5 × 5.7 cm fin dimensions and 0.5 cm spacing between the fins. The finned tubes were used in order to increase the heat transfer area to the PCM and compare them to the coil heat exchanger. The locations of the tubes in the tank were designed in order to promote uniform heat transfer in all directions. The tubes were distributed throughout the four quadrants of the tank equidistantly. Figure 4.10 shows a 3D rendering of the tank with the finned tubes.

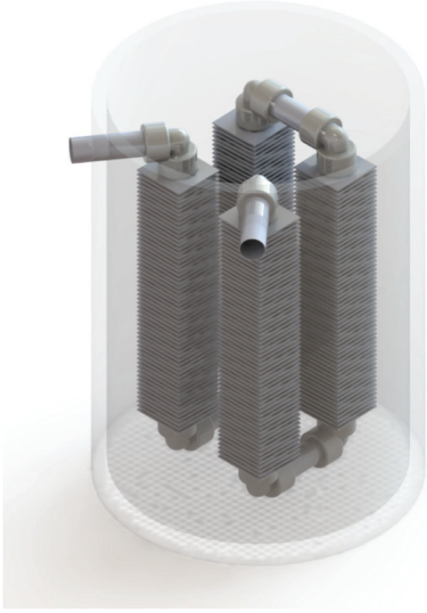

Figure 4.10 3D rendering of Tank B with finned tubes

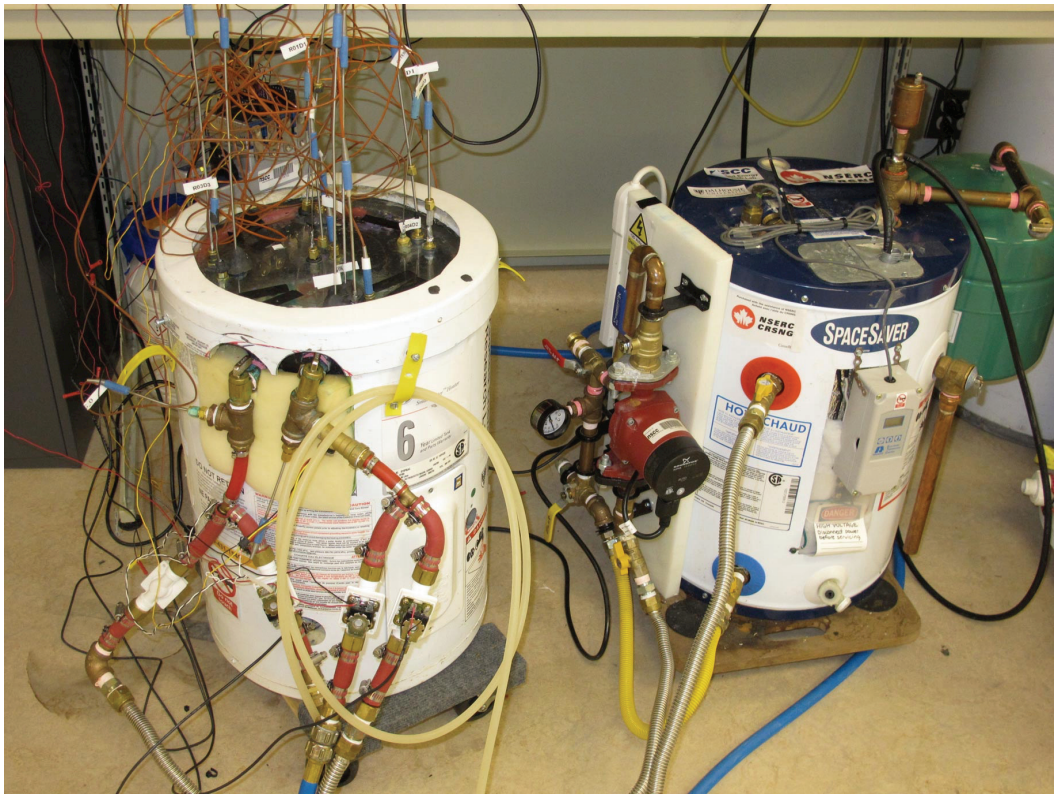

Figure 4.11 Experimental setup of Tank B with the finned tube heat exchanger

4.3.4 Temperature measurements: Finned tubes heat exchanger

Sixteen type-T thermocouples were located within the PCM as shown in Fig. 4.12, while two type-T thermocouples were located at the inlets/outlets of the tubes in order to measure the temperatures of the HTF. The thermocouples were located at five radial positions, and three depths as shown in Fig. 4.12. With the addition of one probe (T16) that was located very close to the edge and at the very bottom of the tank to indicate the state of the tank. The nomenclature of the thermocouples in the tank followed the same system that was shown in section 4.3.2. The spatial distribution of the radial and axial positions aimed to study the nature of the heat transfer from the fins. It differed from the probe distribution in the coil in order to accommodate the different geometry present using the finned heat exchanger. The probes were placed at three various depths, while each depth contained several probes in various radial positions in order to study the effect of the proximity to the HTF inlet on the fin surface temperature. Table 4.4 presents

the radial positions (relative to the center), and axial positions (relative to the surface) in the nomenclature system.

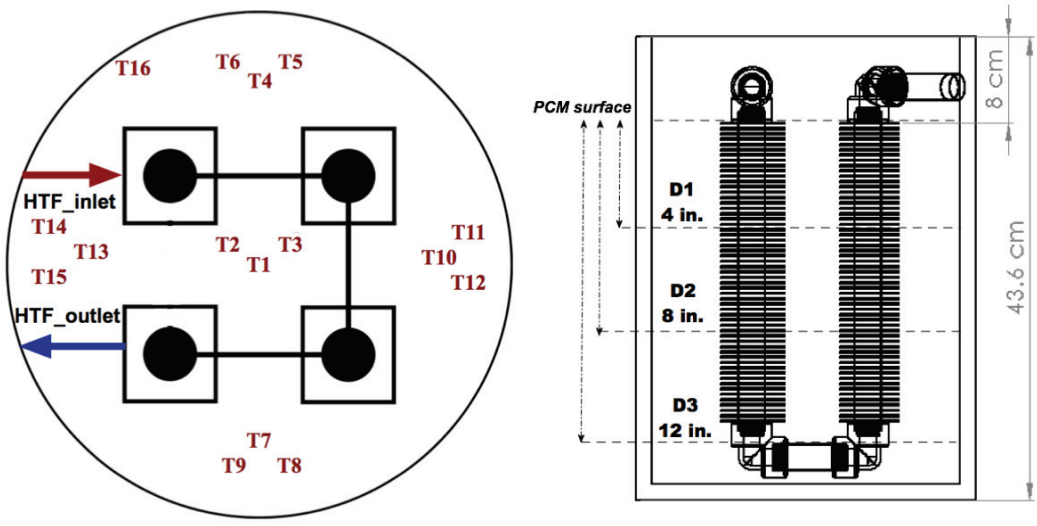

Figure 4.12: Top view and back view of Tank B (fins) with thermocouple locations

Table 4.4: Radial and axial positions used for Tank B: Finned Tubes Heat Exchanger

Distance From Centre	**Probes**
2.55 cm (1 in.)	T1,T2, T3
11.43 cm (4.5 in.)	T4, T7, T10, T13
12.75 cm (5 in.)	T5, T6, T8, T9, T11, T12, T14, T15
Distance From Surface	**Probes**
10.2 cm (4 in.)	T1, T4, T10, T7, T13
20.4 cm (8 in.)	T2, T5, T8, T11, T14
30.6 cm (12 in.)	T3, T6, T9, T12, T15

4.4 PHASE CHANGE MATERIAL

Dodecanoic acid ($CH_3(CH_2)_{10}COOH$), 98% pure, Alfa Aesar, also known as lauric acid) was chosen as the PCM for this study because it is non-toxic, it possesses a melting temperature of 43.5 ± 0.5 ºC which is within the range of the desired application (SDHW), it is relatively inexpensive and it shows little hysteresis (Murray et al., 2011; Desgrosseilliers et al., 2013). The thermophysical properties of dodecanoic acid are presented in Table 4.5.

Dodecanoic acid was used as the PCM for both Tank A and Tank B. The mass of the PCM used for each tank defined the theoretical storage capacity of each tank. The theoretical storage capacities were calculated using the method discussed in section 3.1. Table 4.6 presents the theoretical latent and sensible storage capacities in the tested tanks assuming an initial temperature of 20 ± 2°C and several final temperatures.

Table 4.5 Physical Properties of dodecanoic acid (Desgrosseilliers et al., 2013; Shokouhmand and Kamkari, 2013)

Heat capacity solid at 20°C	1.95 ± 0.03 J g^{-1} K^{-1}
Heat capacity liquid at 45°C	2.4 ± 0.2 J g^{-1} K^{-1}
Thermal conductivity solid at 30 °C	0.160 ± 0.004 W m^{-1} K^{-1}
Thermal conductivity liquid at 50 °C	0.150 ± 0.004 W m^{-1} K^{-1}
Density solid at 22 °C	930 ± 20 kg m^{-3}
Density liquid at 50 °C	885 ± 20 kg m^{-3}
Volume change from 44 °C to 22 °C	6.1%
Onset of melting temperature	43.3 ± 1.5 °C
Heat of fusion	184 ± 9 J g^{-1}

Table 4.6 Theoretical latent and sensible storage capacities in the tested tanks

Tank	PCM Mass (kg)	Final Temperature (°C)	Latent Storage Capacity (MJ)	Sensible Storage Capacity (MJ)	Overall Storage Capacity (MJ)
Tank A	60 .08kg	55	11.04 ± 0.54	4.40 ± 0.18	15.44 ± 0.72
		65	11.04 ± 0.54	5.84 ± 0.30	16.89 ± 0.84
		70	11.04 ± 0.54	6.56 ± 0.90	17.60 ± 0.90
Tank B	25.04 kg	65	4.60 ± 0.54	2.56 ± 0.10	7.16 ± 0.64

4.5 EXPERIMENTAL PROCEDURE

4.5.1 Real-Time solar charging:

Real-time solar experiments were conducted using outdoor solar research facilities at the NSCC Applied Energy Research Lab (AER-Lab), located in Dartmouth, NS, Canada (44.653740; -63.551620 Latitude/Longitude). In preparation for solar experiments, the PCM tank was brought to a state where all probes read were at room temperature (20 ± 2°C). The solar (glycol) loop was then circulated over the period the solar collector received direct insolation. The experiments were conducted during the period of November 2013 to September 2014.

4.5.2 Hot Water Tank Charging

The space saver heating tank as described previous in 4.2.2 was utilized as the heat source for controlled PCM testing. Testing began with all probes reading 20 ± 2 °C. This procedure provided a base line for comparison. The water tank was heated to a set temperature using a digital temperature controller. Testing was conducted under various operating parameters (*i.e.* HTF flow rates, and charging inlet temperatures). The experimental conditions are presented in details in Chapter 5 and Chapter 6.

4.5.3 Discharging

The discharging experiment consisted of using municipal water as the HTF in order to extract the energy from the PCM tank. Municipal water was circulated in the coil when all the probes in the tank were above the melting temperature. The average temperature of the municipal water varied with the seasons ranging from 9 to 17 °C. The municipal water valve was used in order to control the flow rate for the cold HTF. The discharge experiment was conducted until the tank reached an average temperature of 20°C ± 2 °C.

CHAPTER 5 RESULTS AND DISCUSSION: TANK A

This chapter presents the experimental results of charging and discharging of tank A. The results include temperature profiles, heat transfer rates (power input/out), cumulative energy stored with the uncertainty, and heat fluxes. The experiments with real-time solar conditions include additional results of the solar insolation and the glycol inlet/outlet temperatures pattern relative to the insolation.

Charging was conducted under controlled experimental conditions and real-time solar conditions as illustrated in section 4.2.1 and 4.2.2 respectively. The controlled experiments studied the effects of various HTF inlet temperatures and flow rates on the overall performance of the LHESS. The real-time solar experiments studied the seasonal effects on the charging performance of the LHESS.

Discharging was conducted using the municipal water, which varied in temperature according to the season. The effects of the HTF inlet temperature and flow rate were studied during the discharge process.

The comparison between latent storage and sensible storage for tank A is presented in this chapter with charging under real-time solar and discharging using municipal water.

5.1 CHARGING: CONTROLLED EXPERIMENTS

Several controlled experiments were conducted with varying HTF inlet temperatures and flow rates. Table 5.1 lists the experiments conducted along with their varying parameters.

Table 5.1 List of the experiments conducted during charging and the parameters used

Experiment Number	Location in Thesis	Flow Rate	Inlet HTF Temperature
1	Section 5.1.1	1.1 ± 0.02 L/min	60 ± 0.45 °C
2	Section 5.1.1	1.1 ± 0.02 L/min	70 ± 0.45 °C
3	Section 5.1.1	1.1 ± 0.02 L/min	80 ± 0.45 °C
4	Section 5.1.2	1.7 ± 0.02 L/min	60 ± 0.45 °C
5	Section 5.1.2	2.5 ± 0.02 L/min	60 ± 0.45 °C

5.1.1 Effect of HTF inlet temperature

The parametric investigation on the effect of the HTF inlet temperature was conducted using three temperatures: 60, 70 and 80 °C, at a fixed flow rate of 1.1 L/min. The combination of HTF inlet temperature used for charging or discharging the LHESS and the PCM initial temperature can be represented by the Stefan number. The Stefan number is a dimensionless number that relates sensible heat storage to latent heat storage. In the case of melting, the calculation of the sensible heat takes into account the heating of the solid PCM from an initial temperature T_i to the melting temperature T_m using a HTF temperature T_{HTF} as shown in Eq. (5.1) (Ziegler, 2010). Whereas in the case of solidification, the calculation of the sensible heat takes into account the cooling of the liquid PCM from an initial temperature T_i to the melting temperature T_m using a HTF temperature T_{HTF} as shown in Eq. (5.2) (Ziegler, 2010):

$$Ste_{melting} = \frac{C_{p,s}(T_m - T_i) + C_{p,l}(T_{HTF} - T_m)}{\Delta h_m} \tag{5.1}$$

$$Ste_{solidifcation} = \frac{C_{p,l}(T_i - T_m) + C_{p,s}(T_m - T_{HTF})}{\Delta h_m} \tag{5.2}$$

In the case of LHESS, the *Ste* number is generally less than 1 since the sensible heat capacity associated with the specific heat C_p is smaller than the latent heat capacity Δh_m. The Stefan number for experiments 1, 2, and 3 is 0.464, 0.594, and 0.725, respectively.

These differences show that a higher HTF inlet temperature signifies a lower percentage of latent heat storage.

Figures 5.1 to 5.3 illustrate the temperature profiles measured by the 12 temperature probes located in Tank A during all three experiments. An illustration of the tank is shown next to each figure with the location of the probes shown in the graph. Figures 5.1a), 5.2a) and 5.3a) show the temperature profiles of the inner probes T1 to T4. Figures 5.1b), 5.2b) and 5.3b) show the temperature profiles if the middle probes T5 to T8. Figures 5.1c), 5.2c) and 5.3c) show the temperature profiles of the outer probes T9 to T12.

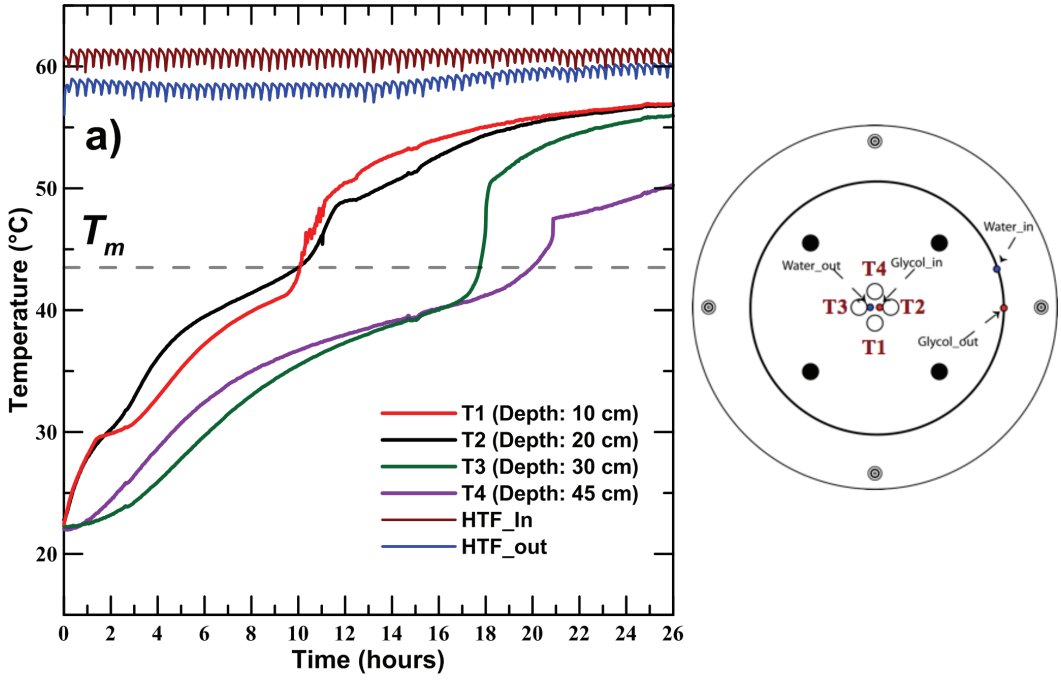

Figure 5.1 Temperature profiles as a function of time measured during charging ($T_{H,in}$ = 60 °C, 1.1 L/min) : a) Inner probes T1 to T4

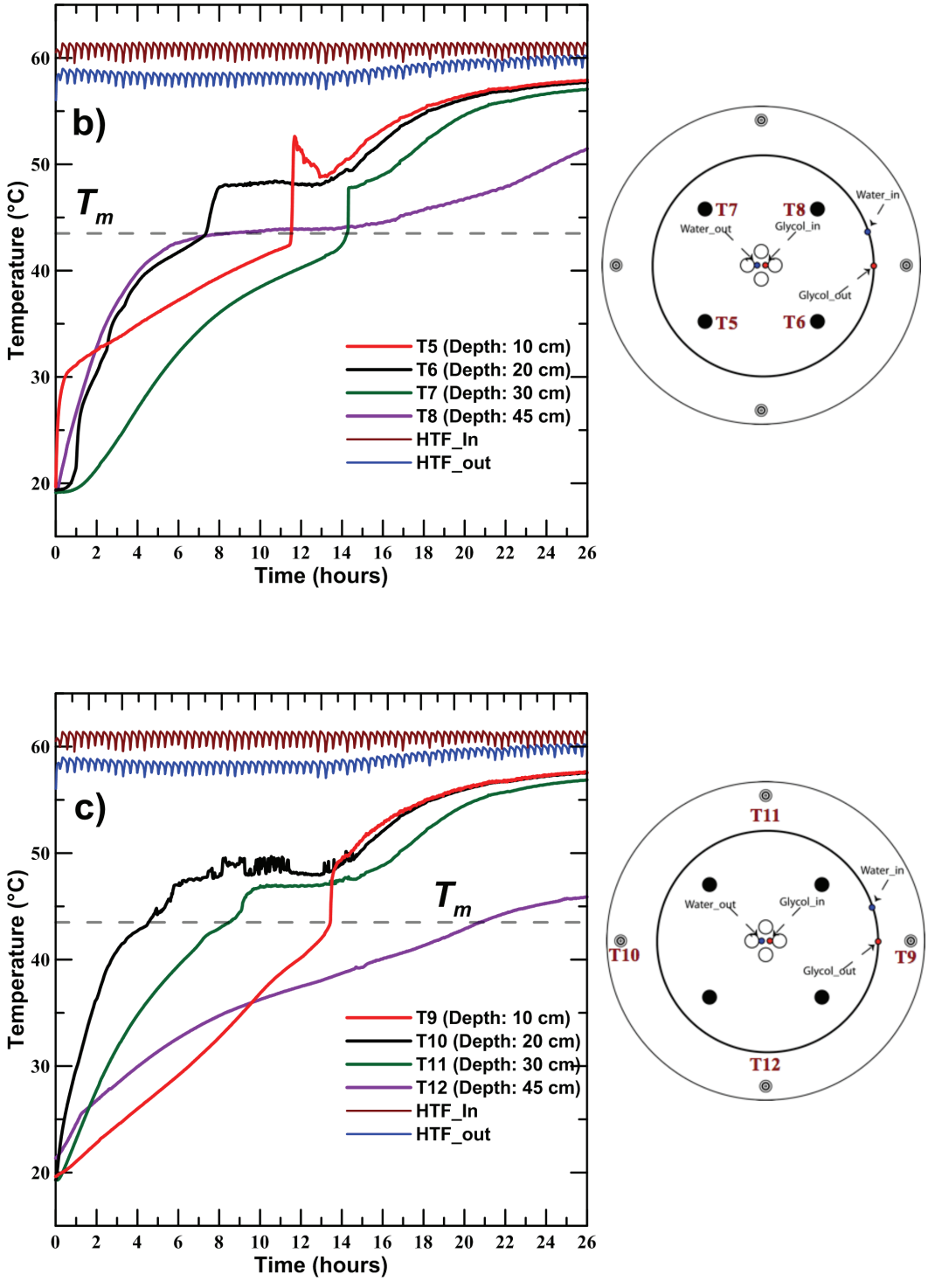

Figure 5.1 Temperature profiles as a function of time measured during charging ($T_{H,in}$ = 60 ºC, 1.1 L/min): b) Middle probes T5 to T8, c) Outer probes T9 to T12, continued

Each figure shows four probes at four various depths with the color coding red, black, green and purple for 10, 20, 30 and 40 cm depth, respectively. Water was used as the HTF for the charging experiments, entering through the coiled part and exiting after passing the straight copper section.

Experiment 1 utilized a HTF temperature of 60 ºC. The experiment showed a similar temperature profiles for T1 and T2 as shown in Fig. 5.1a). The probes were located at the center of the tank and near the top, with T2 having a slightly higher temperature prior to melting. Similarly T4 showed higher temperature profiles than T3 during the first half of the process. As it was mentioned earlier in section 4.2.3, the radial positions of T1 to T4 were shifted slightly off center in order to accommodate for the HTF lines. Therefore, the difference in temperature is due to the radial proximity of T2/T4 in comparison to T1/T3 to the straight copper section. However, as more PCM melted, T1 showed higher temperatures than T2, and T3 showed higher temperatures than T4, which is indicative of the role played by natural convection during later stages of the process as more of the PCM melts and moves upwards.

The coil in the tank used for water charging starts coiling in the direction of T5, which explains the fast dynamic response of the probe T5 in Fig. 5.1b). However, the first probes to show melting were T6 and T8. The probes T6 and T8 were located at the same depth as the 2^{nd} and 4^{th} turn of the coil, which explains why they showed higher temperatures in comparison to T5 and T7 which were at the depth of mid-point of the pitch distance. The temperature profile of T5 shows a slight anomaly after melting, with a sudden rise and drop. One probable explanation for this anomaly could be the sudden movement of hot PCM upwards, which causes the sudden rise in the temperature recorded by T5. After all probes showed melting at around 14 hour, it can be observed that a vertical gradient was established with the highest temperatures recorded by the probes closer to the surface. These observations point to a conduction dominant mode of heat transfer in the mid-section of the tank during the early stages of the process, and an onset of natural convection as more PCM melts.

Figure 5.1c) shows the temperature profiles of the probes on the outer edge of the tank. The temperature profile of T10 indicates melting after approximately 7 hours, which is

due to the probes location near the 2nd turn of the coil, and exposure to hotter HTF than T11 due to the direction of the HTF from top to bottom. The location of T11 also was similar to T10 however close to the 3rd turn of the coil. It can be observed that T9, which was located at the top of the tank however not exposed radially to any heat surface, was not affected by natural convection until after 12 hours, which can be explained by the delay of melting on the outer edges of the tank and the dominance of radial conduction during the early stages of the process. The last probe to show melting was T12, due to its location at the bottom of the tank and on the outer edge with no direct radial exposure to a heat surface.

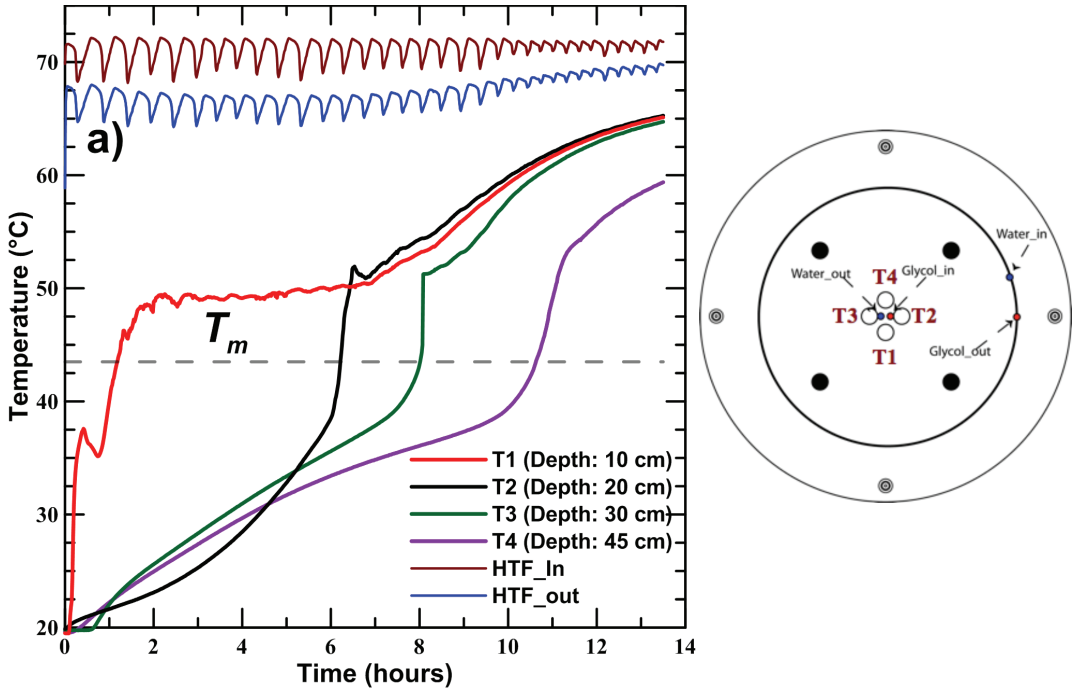

Figure 5.2 Temperature profiles as a function of time measured during charging ($T_{H,in}$ = 70°, 1.1 L/min) : a) Inner probes T1 to T4

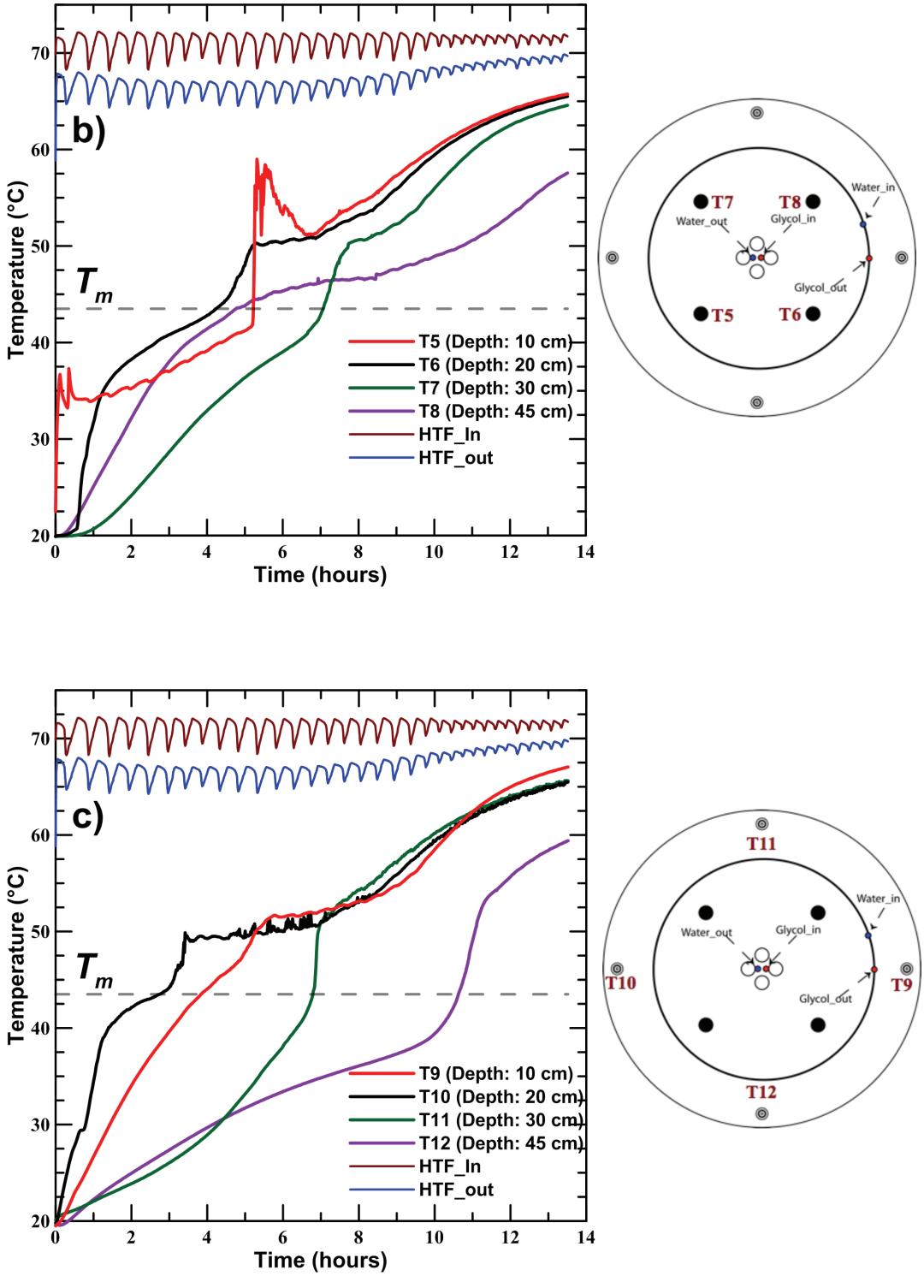

Figure 5.2 Temperature profiles as a function of time measured during charging ($T_{H,in}$ = 70°, 1.1 L/min) : b) Middle probes T5 to T8, c) Outer probes T9 to T12, continued

The effect of the HTF inlet temperature was studied in context of the changes observed in the behavior of the PCM within the tank using the probes located in the tank. The temperature profiles of the experiment using HTF inlet temperature of 70 ºC are shown in Fig. 5.2. The probe T1 in Fig. 5.2a) showed melting first, which is due to the faster melting of PCM in the tank and faster movement of liquid to the top. The same pattern was observed for T2, T3, and T4 with the shallowest probe showing melting prior to the deepest probe. This indicates that faster melting was observed in the mid section of the tank due to the increase of the HTF inlet temperature, with an increase in the vertical temperature gradient in comparison to experiment 1. The last probe to show temperature above melting was T4, with a melting time of 20 hours and 10.5 hours for the experiments 1 and 2 respectively.

The results observed in Fig. 5.2b) show the same melting behavior as the one discussed for Fig. 5.2a). The difference in the observed melting time between T7 and T8 was approximately 2.5 hours for experiment 2 in comparison to 7 hours in experiment 1. As mentioned earlier, the location of T8 gives it an advantage due to its proximity to a heat source. However this decrease in time shows that the advantage of the axial position of T7 during charging was more noticeable in experiment 2. Therefore, this decrease in melting time indicates the significance of the role played by natural convection with the increase of the temperature of the HTF. The probe T7 was the last probe to undergo melting between T5 to T8, with 13 and 7 hours for experiments 1 and 2, respectively.

The temperatures measured by the outer probes observed during experiment 2 are shown in Fig. 5.2c). The first probe to show melting was T10, which is consistent with the results observed in Fig. 5.1c). However the second probe to show melting was T9 instead, which is inconsistent with experiment 1 that showed T11 as the second probe to melt. This shows that an increase in the HTF did speed up the onset of natural convection as mentioned earlier, which led to higher temperatures being recorded by T9 in experiment 2 in comparison with experiment 1. The last probe to show melting was T12 which is consistent with the observations and reasoning from experiment 1.

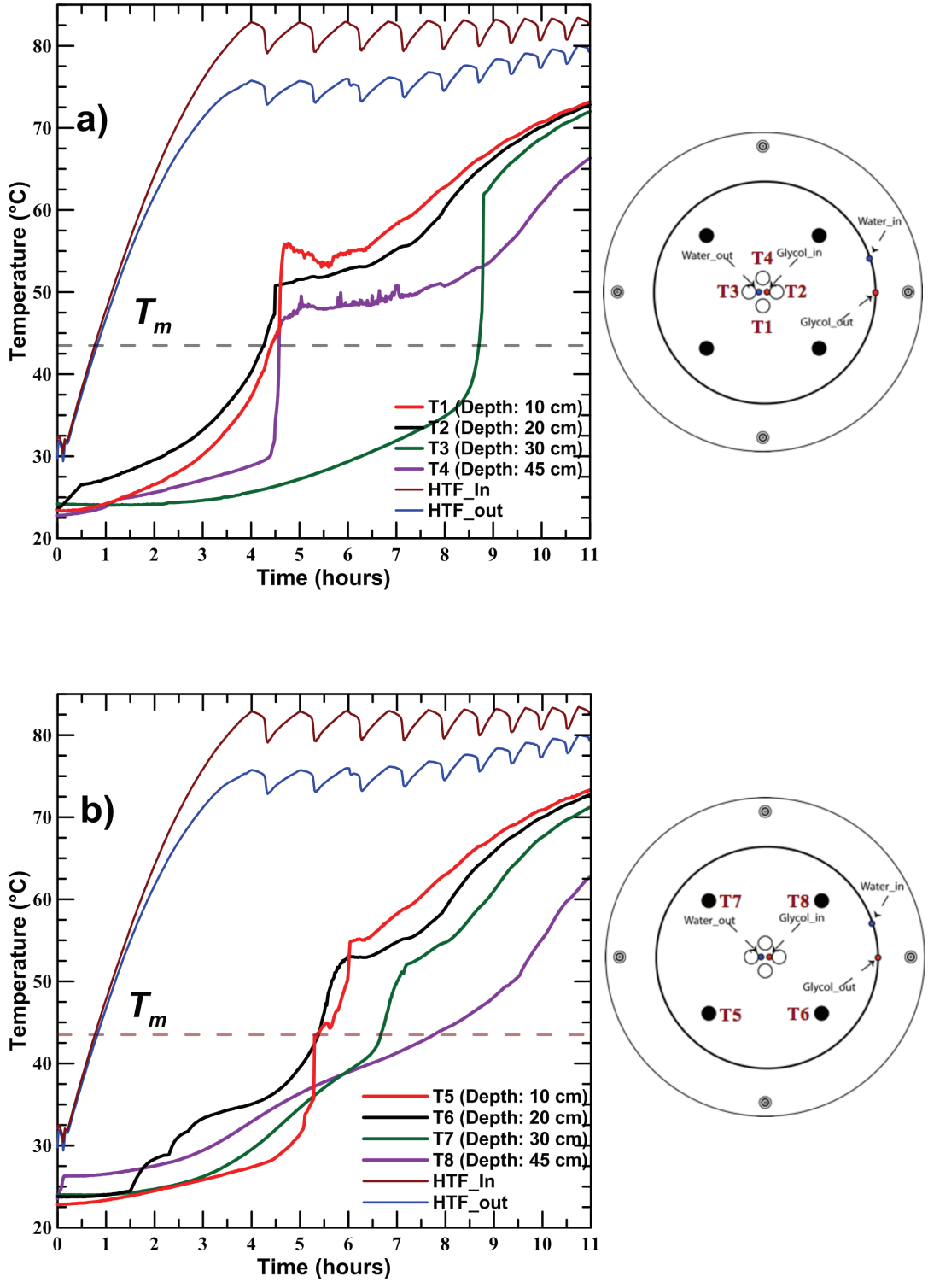

Figure 5.3 Temperature profiles as a function of time measured during charging ($T_{H,in}$ = 80°, 1.1 L/min) : a) Inner probes T1 to T4, b) Middle probes T5 to T8

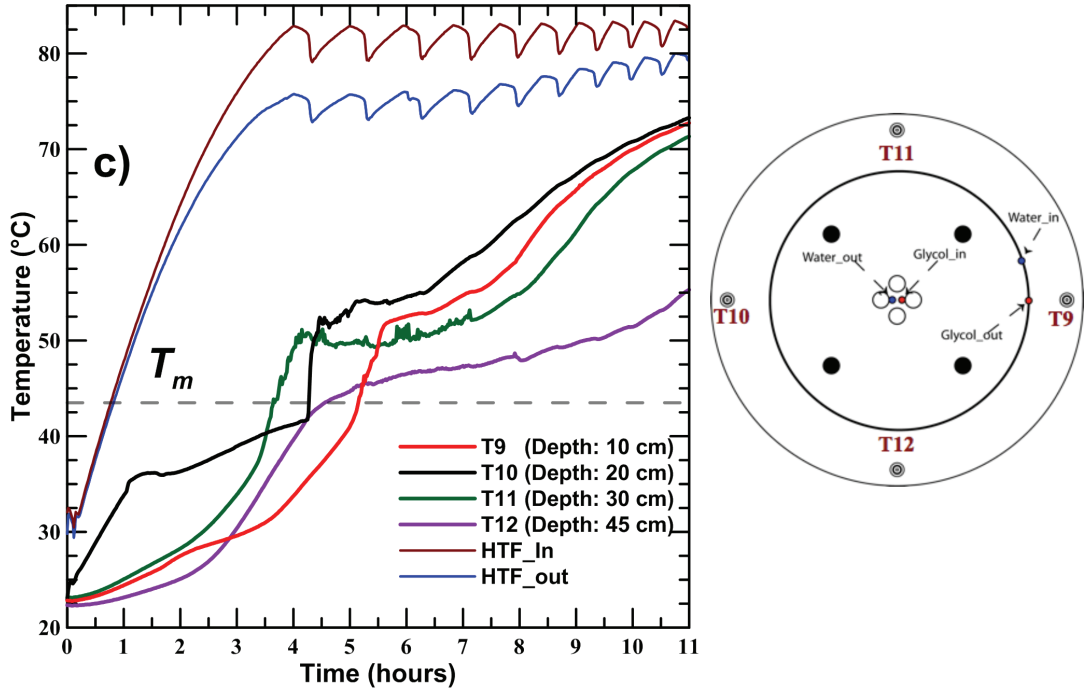

Figure 5.3 Temperature profiles as a function of time measured during charging ($T_{H,in}$ = 80º, 1.1 L/min) : c) Outer probes T9 to T12, continued

The third experiment utilized a HTF inlet temperature of 80 ºC, however it was different than the previous experiments in the sense that the HTF temperature increased gradually to 80 ºC over a period of approximately 4 hours. The experiment was set up to test the temperature controller, and therefore a constant temperature of 80 ºC was not reached prior to the start of the experiment. The reason for such inconsistency is due to a technical failure of the temperature controller after that experimental test was conducted and the inability to reach temperatures as high as 80 ºC in future experiments. Therefore an experiment with the HTF at 80 ºC throughout the whole process was not performed.

Even though the experiments are not directly comparable, the results from the experiment are valuable and they reaffirm certain findings from the first two experiments. For instance, as shown in Fig. 5.3a), T2 showed higher temperatures than T1 throughout the period of the gradual rise of the HTF inlet temperature, however as the HTF inlet temperature stabilizes at 80 ± 2 ºC, T1 showed higher temperatures than T2 due to the movement of PCM to the top of the tank with melting. Similarly to

experiment 2, T4 showed higher temperatures than T3 during the gradual heating stage and underwent melting faster than T3 due to its location next to the coil, however as the temperature stabilized and more PCM melted, T3 showed higher temperature profiles than T4. Therefore, the gradual heating of the tank illustrates the division between the modes of heat transfer during the early stage and later stage of the process.

Figure 5.3b) does not show the same anomaly for T5, however the third experiment as mentioned earlier underwent gradual heating of the tank and therefore did not experience the effect of a sudden movement of PCM. This observation further supports the explanation of the anomaly given in the first two experiments. Similarly to the first two experiments, T6 was the first to show melting, followed by T5, which showed a fast rise in temperature as the HTF temperature reached 80 ºC. The temperature profile observed by T8 was higher than T7 during the gradual heating period, however as the HTF temperature stabilized, the temperature recorded by T7 were higher and reached melting faster than T8. This was not observed in experiment 1 and 2, which showed a faster melting by T8 due to its proximity to the coil's 4^{th} turn. One probable explanation for the difference in the PCM behavior in experiment 3 is the change in the level of natural convection. As seen that prior to the HTF temperature reaching 80 ºC, T8 was showing behavior similar to that in experiments 1 and 2, however as the temperature reached its maximum value, the PCM melted at a faster rate, which moved heat faster in the direction of T7.

Figure 5.3c) shows similar profiles to Fig. 5.1c) for all probes prior to the stabilization of the HTF temperature. However, after the temperature reached 80 ºC, the temperature profiles begin to resemble those observed during experiment 2 seen in Fig. 5.2c). These observations reiterate the importance of natural convection after melting, in addition to showing a relationship between the HTF inlet temperature and the time required for the onset of natural convection.

Figures 5.4 and 5.5 show the power input and energy stored respectively for experiment 1. The fluctuations in the inlet temperature and power input are a result of the temperature controller dynamics on the hot water tank. It is observed that the general trend shows an increase of the power input during the first 6 hours, which plateaus

around 0.2 kW and then start to decrease for the remaining part of the process. The initial increase at the beginning could be explained by the onset of natural convection increasing the heat transfer coefficient. The decrease at the end is explained by the decrease of the temperature difference between the inlet and outlet temperatures of the HTF. The power input ranged between 0.2 and 0.1 kW, while the heat flux ranged between 2.5 and 1.25 kW/m^2. The heat flux was determined through dividing the power input by the surface area of the coil heat exchanger (0.08 m^2).

Figure 5.5 shows the cumulative energy stored along with the cumulative uncertainty associated with it. The cumulative energy stored for experiment 1 was 15.415 MJ ±13%, however the cumulative energy stored was closely aligned with the theoretical storage capacity, which provides great confidence in the experimental results. The total charging time in order to bring the tank from an average temperature of 20 ± 2 °C to 55 ± 2 °C was 26 hours. The final temperature of the PCM was chosen to be 5 °C lower than the HTF inlet temperature in order to avoid long overcharging times.

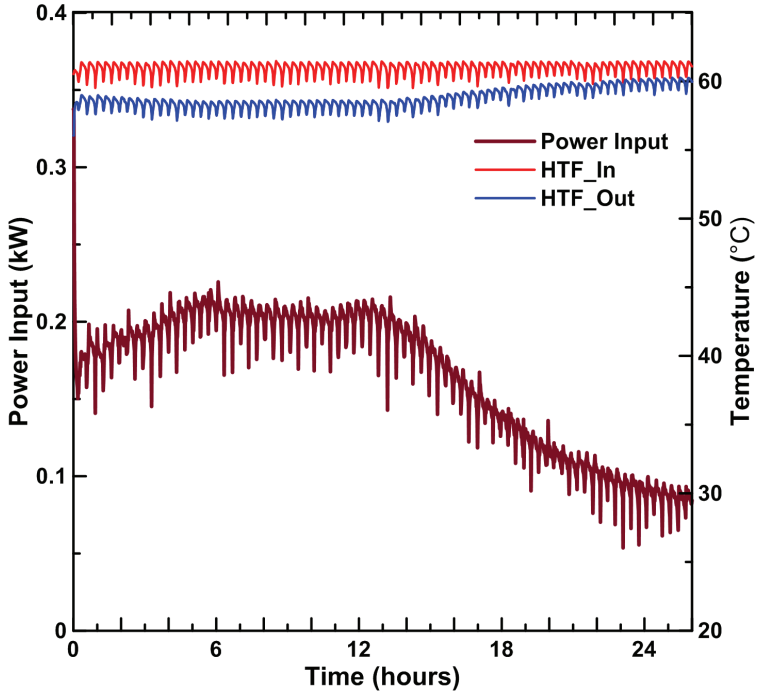

Figure 5.4 Power input as a function of time during charging experiment ($T_{H,in}$ = 60°C, 1.1 L/min)

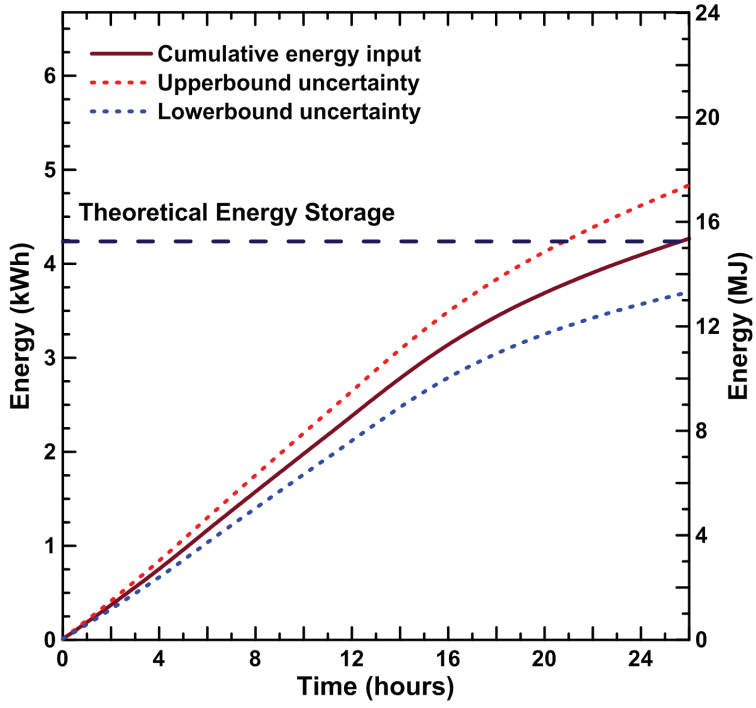

Figure 5.5 Cumulative energy input as a function of time during charging experiment ($T_{H,in}$ = 60°C, 1.1 L/min)

Figures 5.6 shows the power input for experiment 2. Due to the control mechanism of the water tank controller, the fluctuations in the inlet temperature increase with higher temperatures, which can be observed in experiment 2 and 3. The power input in experiment 2 reaches 0.4 kW which is double the value observed in experiment 1, which shows the significant effect of increasing the HTF inlet temperature on heat transfer rates. The power input ranged between 0.4 and 0.2 kW, while the heat flux ranged between 5 and 2.5 kW/m^2.

The total charging time to bring the tank from an average temperature of 20 ± 2 °C to 65 ± 2 °C was 13.5 hours. Therefore the increase of the HTF temperature from 60 to 70 °C decreased the charging time by 52%. The cumulative energy stored for experiment 2 was 16.13 MJ ± 7.5% as shown in Fig. 5.9. The measurement uncertainty of the temperature probe is the main contributor to the overall uncertainty. Consequently, the uncertainty observed in experiment 2 was lower than that of experiment 1 due to the increase in the temperature difference between the HTF inlet and outlet in experiment 2.

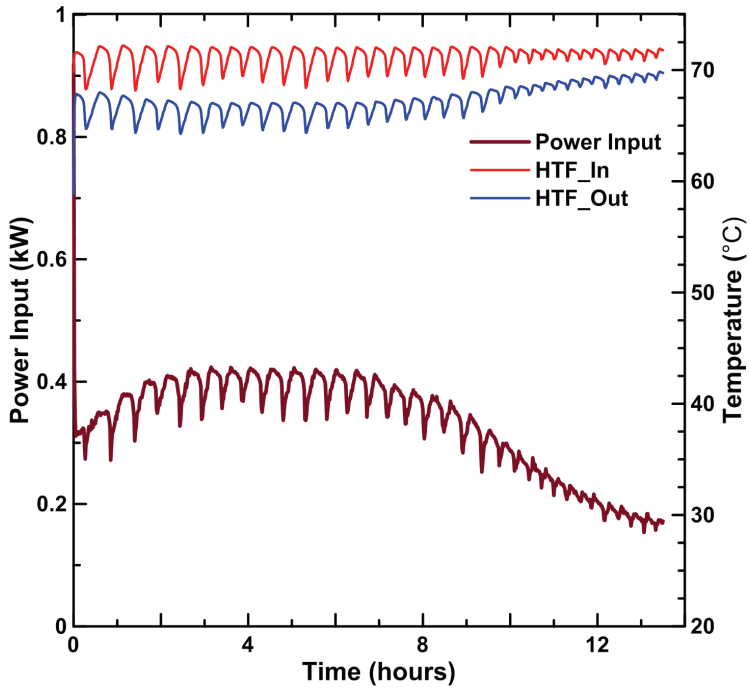

Figure 5.6 Power input as a function of time during charging experiment ($T_{H,in}$ = 70°C, 1.1 L/min)

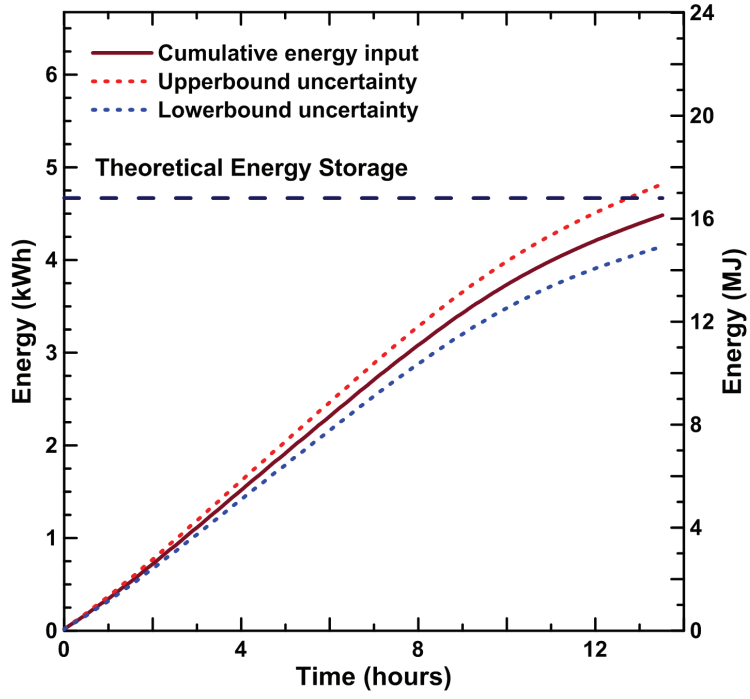

Figure 5.7 Cumulative energy input as a function of time during charging experiment ($T_{H,in}$ = 70°C, 1.1 L/min)

Figures 5.8 and 5.9 show the power input and energy stored respectively for experiment 3. As mentioned earlier the HTF inlet temperature for experiment 3 gradually reached the desired temperature as opposed to experiment 1 and 2, which had the desired HTF inlet temperature at the beginning of the process. Even though such inconsistency makes it difficult to compare overall charging time, however the instantaneous heat transfer rate remains a valid factor to compare between all three experiments.

The power input in experiment 3 reached 0.6 kW which is 1.5 times the value observed in experiment 2 and 3 times the value observed during experiment 1. The power input ranged between 0.6 and 0.3 kW, while the heat flux ranged between 7.5 and 3.75 kW/m^2. The final average temperature of the PCM was chosen as 70 °C in order to avoid overheating the tank. The total charging time to bring the tank from an average temperature of 20 ± 2 °C to 70 ± 2 °C was 11 hours. However the first 4 hours were not charged at the desired consistent temperature, therefore the time of the process is not a true reflection of the charging time using 80 °C inlet temperature

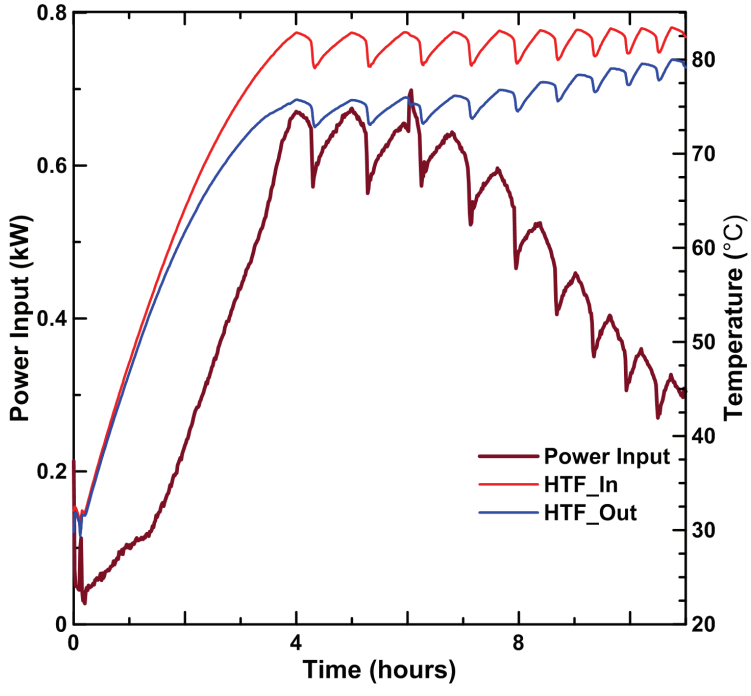

Figure 5.8 Power input as a function of time during charging experiment ($T_{H,in}$ = 80°C, 1.1 L/min)

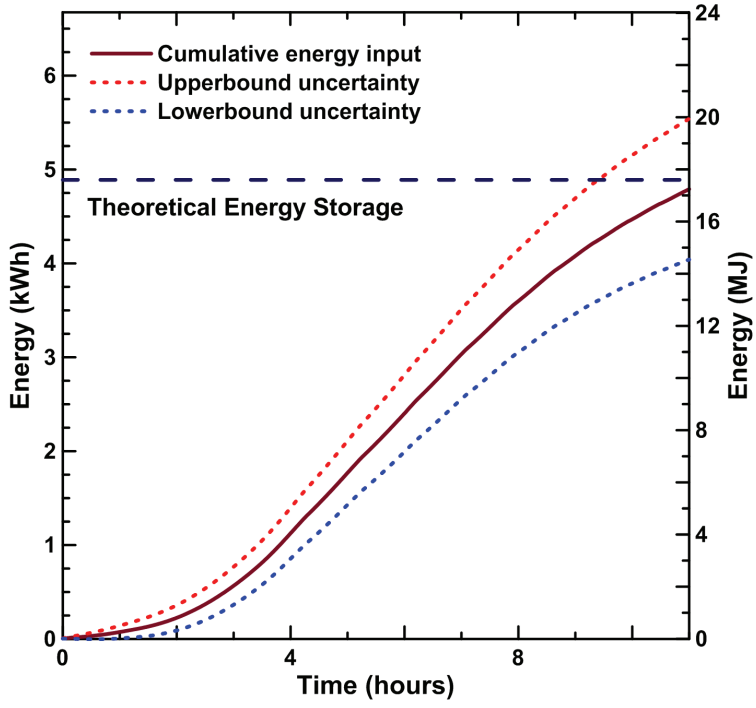

Figure 5.9 Cumulative energy as a function of time during charging experiment ($T_{H,in}$ = 80°C, 1.1 L/min)

The cumulative energy stored during experiment 3 was 17.24 MJ ± 15.6 % as shown in Fig. 5.9. However the cumulative energy stored was consistent with the first two experiments, which showed close proximity with the theoretical storage capacity of the tank.

It is therefore observed that increasing the HTF inlet temperature (*i.e.* Stefan number) results in substantially higher heat transfer rates and lower charging times. Table 5.2 summarizes the results observed during experiment 1, 2 and 3.

Table 5.2 Summary of results for charging experiments with various inlet temperatures

Experiment	Power input range (kW)	HTF inlet temperature	Cumulative Energy stored (MJ)	Charging time (Hours)
1	0.2- 0.1	60 ± 0.45 °C	15.41 ± 13 %	26
2	0.4-0.2	70 ± 0.45 °C	16.13 ± 7.4 %	13.5
3	0.6-0.3	80 ± 0.45 °C	17.24 ± 15.6%	11

5.1.2 Effect of HTF flow rate

The parametric investigation on the effect of the HTF flow rate was conducted using three flow rates: 1.1, 1.5 and 2.5 L/min, at a fixed inlet temperature of 60 °C. The dimensionless Reynolds number can represent the flow rate of water inside the heat exchanger, as well as the flow regime. The Reynolds number is the ratio of the inertia and viscous forces of the fluid. For the case of a pipe, it is represented by Eq. (5.3):

$$\mathrm{Re} = \frac{VD}{\nu} \tag{5.3}$$

where V is the average velocity of the fluid (in m/s), D is the inner diameter of the pipe (in m) and ν is the kinematic viscosity (in m^2/s). An internal pipe flow is defined as turbulent with a Re > 2300 (Massoud, 2005). The values of the Reynolds number for the flow rates used are 5847, 8186 and 13565 for 1.1, 1.5 and 2.5 L/min, respectively. The flow for all three experiments was turbulent. A Turbulent flow is generally known for promoting a higher heat transfer coefficient due to internal forced convection in comparison to laminar flow.

Figures 5.1, 5.10 and 5.11 illustrate the temperature profiles of the 12 temperature probes located in the tank during all three experiments. The representation of the temperature profiles follows the same format discussed in section 5.1.1. The internal probes T1 to T4 are shown in Figs. 5.1a), 5.10a) and 5.11a). All three figures show T2 being the first probe to undergo melting. The reason being is the radial proximity of T2 in comparison to the other probes to the straight cooper section as mentioned in section 5.1.1. The effect of increasing the flow rate caused the temperature profile of T2 to shift in time, with a faster melting time at higher flow rates. This can be explained by the increase in velocity, which in effect decreased the resistance due to forced convection internally, and may have contributed to a higher heat transfer in the location where T2 is located. T1 is observed to be the second probe to undergo melting and shows similar profiles in experiments 4 and 5.

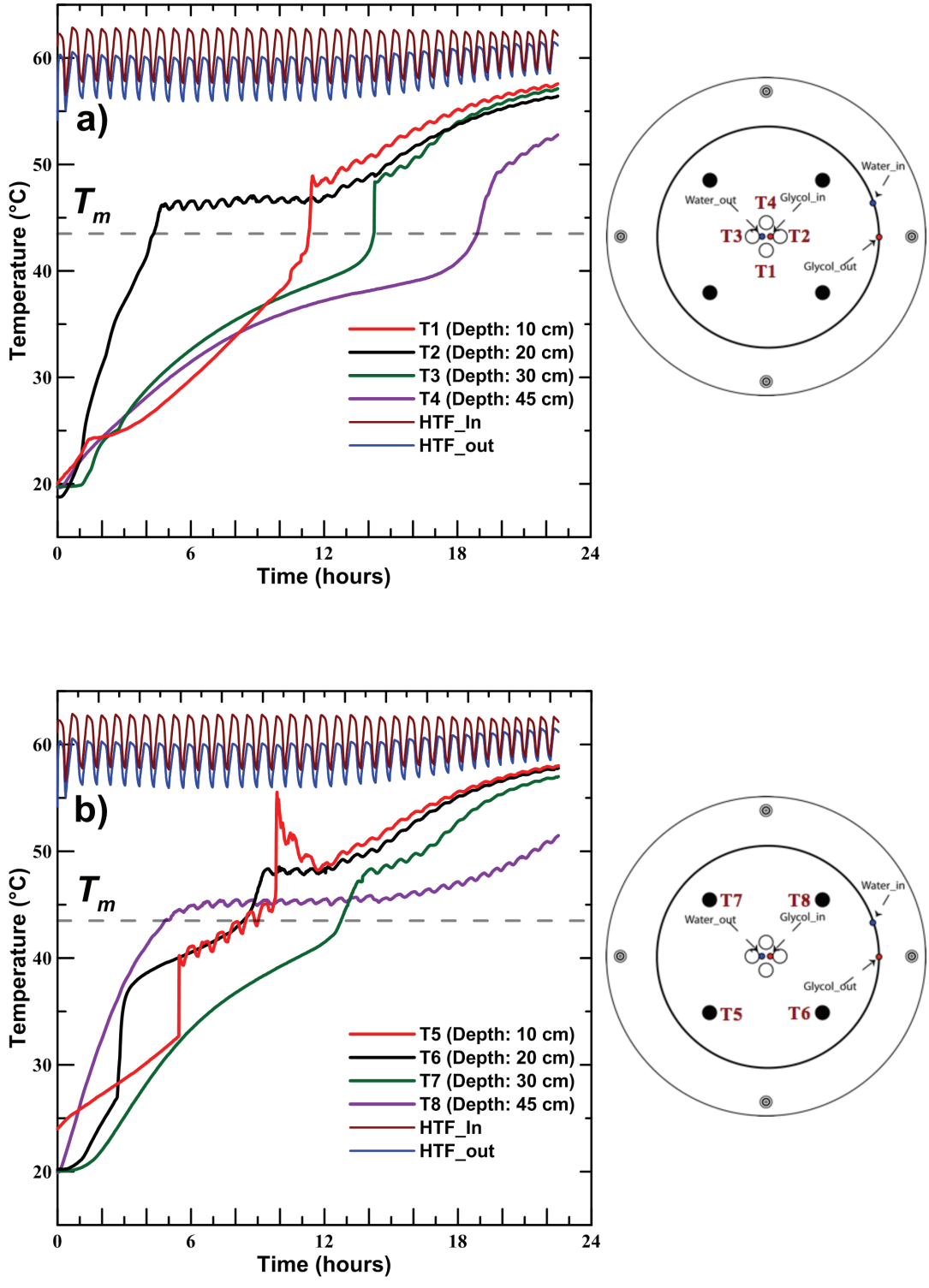

Figure 5.10 Temperature profiles as a function of time measured during charging ($T_{H,in}$ = 60°, 1.5 L/min) : a) Inner probes T1 to T4, b) Middle probes T5 to T8

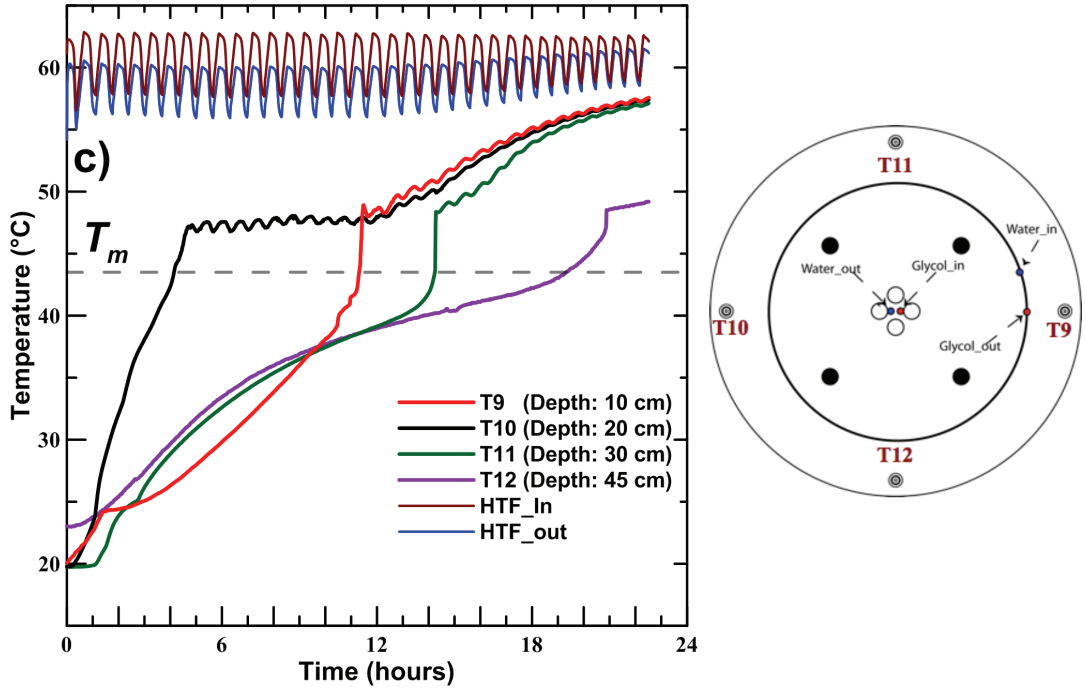

Figure 5.10 Temperature profiles as a function of time measured during charging ($T_{H,in}$ = 60°, 1.5 L/min) : c) Outer probes T9 to T12, continued

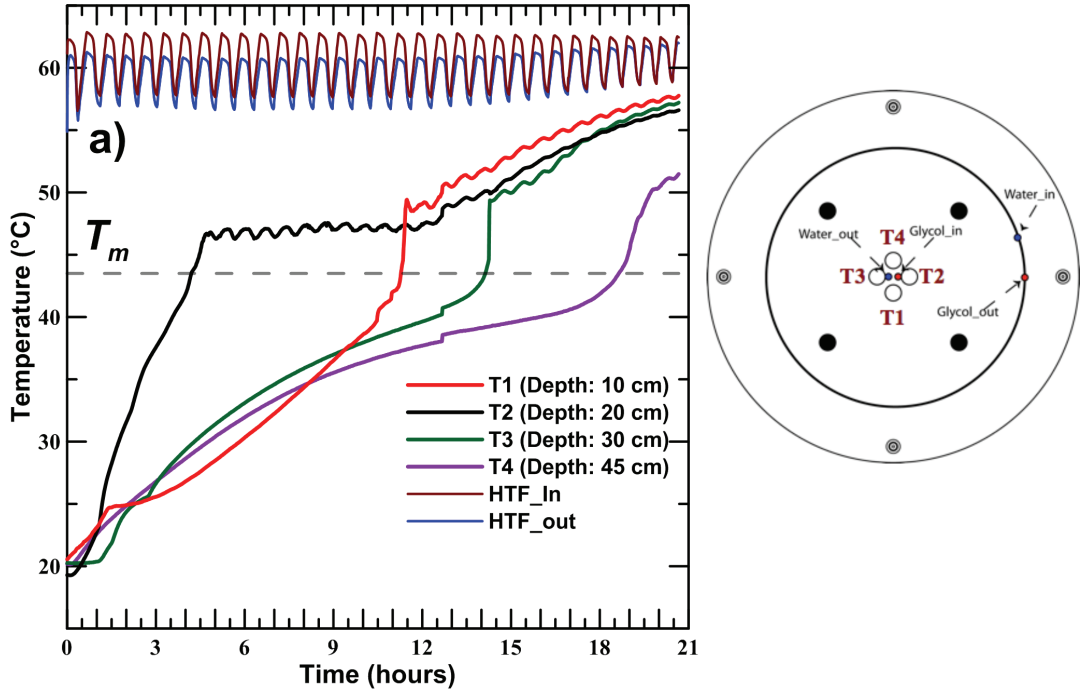

Figure 5.11 Temperature profiles as a function of time measured during charging ($T_{H,in}$ = 60°, 2.5 L/min) : a) Inner probes T1 to T4

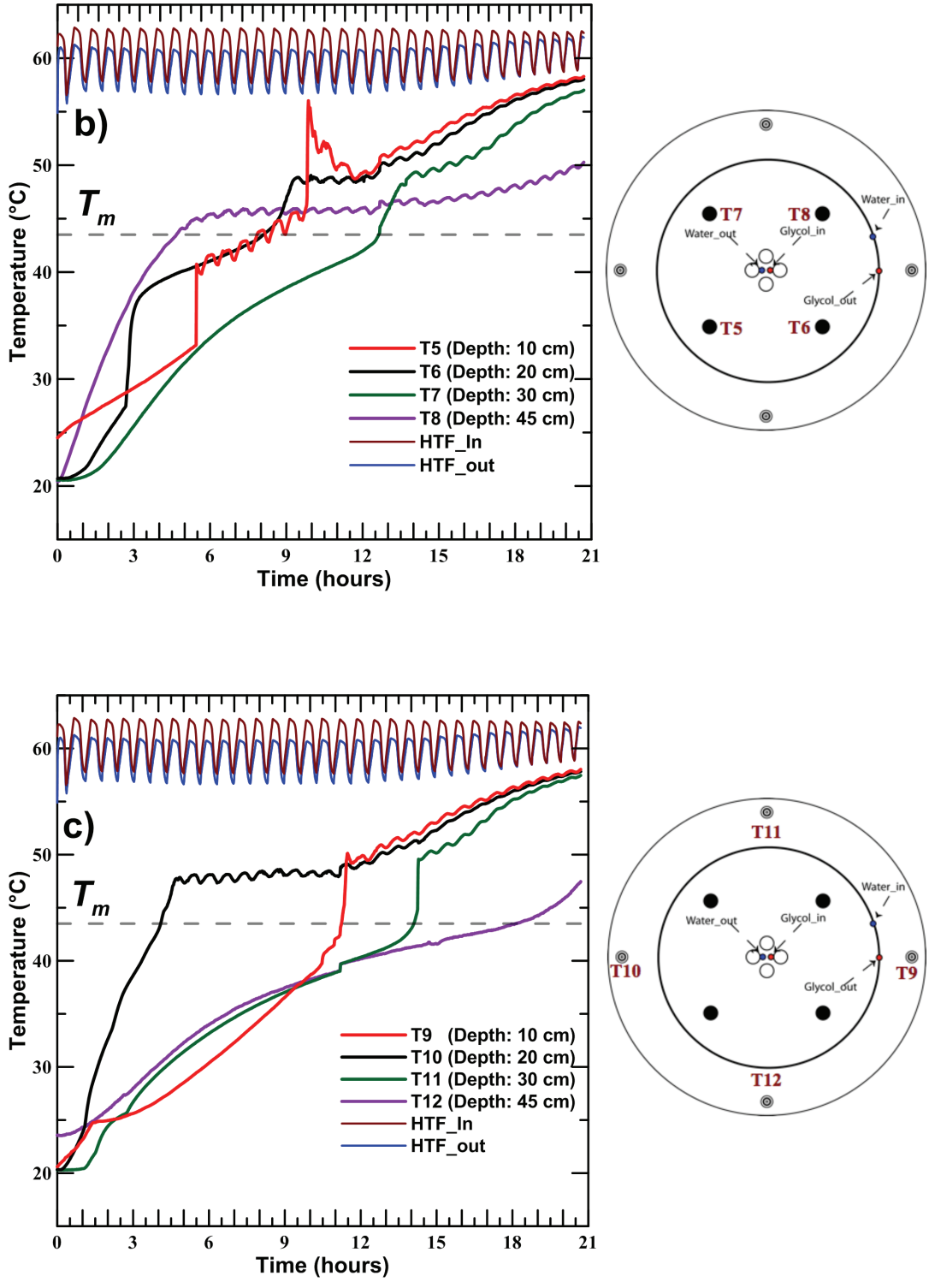

Figure 5.11 Temperature profiles as a function of time measured during charging ($T_{H,in}$ = 60°, 2.5 L/min) : b) Middle probes T5 to T8, c) Outer probes T9 to T12, continued

Figures 5.1b), 5.10b) and 5.11b) show the temperature profiles of T5 to T8. The anomaly associated with T5, which was observed in experiment 1 and 2 and discussed in section 5.1.1, is also present experiments 4 and 5. The temperature profiles of all three experiments are closely aligned with the exception of a time shift between them; the charging time decreased with an increase in HTF flow rate.

Figures 5.1c), 5.10c) and 5.11c) show the temperature profiles of T9 to T12. As discussed in section 5.1.1, T9 did not undergo melting until the later stages of experiment 1. However, it is observed in experiments 4 and 5 that T9 shows melting prior to T11. The early stages of both experiments show T9 lagging behind T11 and T12, however the rise in temperature is witnessed at an earlier stage with 2 hours difference between experiment 1 and experiments 4 and 5. The rest of the probes T10 to T12 show similar profiles as experiment 1 with the exception of a time shift, however the profiles can be explained by the same reasons given the previous section: the heat transfer coefficient due to forced convection inside the pipe increases with an increase in the Reynolds number. Consequently this increases the overall heat transfer coefficient between the HTF and the PCM which contributes to faster melting times, which in effect contributes to an earlier onset of natural convection.

Figures 5.12 and 5.13 show the power input and energy stored respectively for experiment 4. As mentioned in section 5.1.1, the fluctuations in the inlet temperature and power input are a result of the temperature controller dynamics on the hot water tank. The general trend observed was similar to experiment 1 in the sense that the power input increases during the first 6 hours and then plateaus. However, the plateau showed an increase of 0.05 kW over the 0.2 kW observed in experiment 1. The power input ranged between 0.25 and 0.1 kW, while the heat flux ranged between 3.1 and 1.25 kW/m^2. Figure 5.13 shows the cumulative energy stored along with the cumulative uncertainty associated with it. The cumulative energy stored for experiment 4 was 15.35 ± 14.2 %, the cumulative energy stored was closely aligned with the theoretical storage capacity, which provides higher reliability in the experimental results. The total charging time in order to bring the tank from an average temperature of 20 ± 2 °C to 55 ± 2 °C was 22 hours.

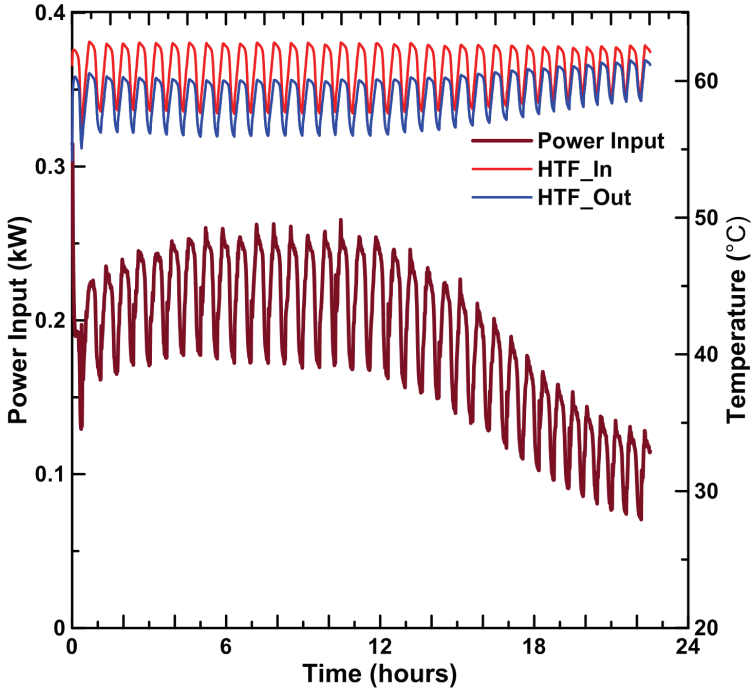

Figure 5.12 Power input as a function of time during charging experiment ($T_{H,in}$ = 60°C,1.5 L/min)

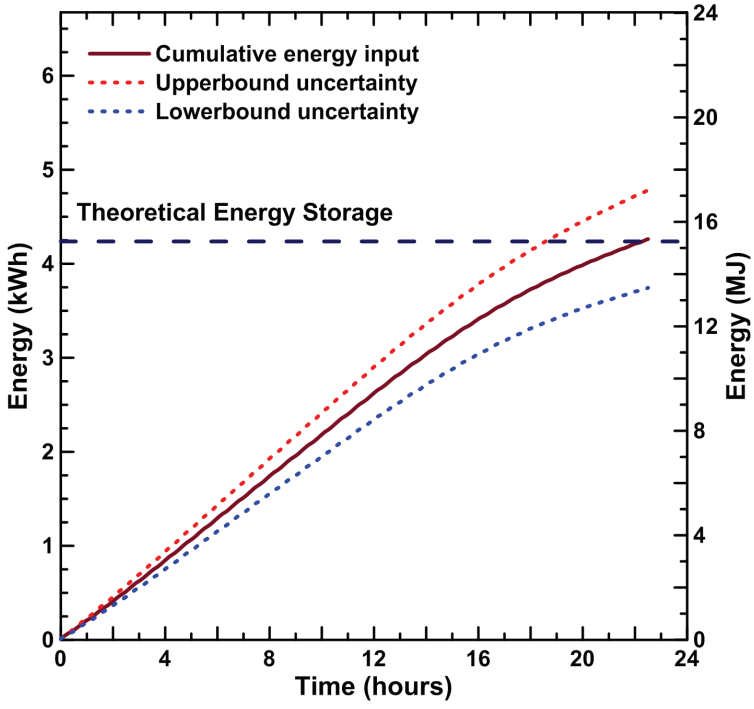

Figure 5.13 Cumulative energy as a function of time during charging experiment ($T_{H,in}$ = 60°C, 1.5 L/min)

Figure 5.14 shows the power input for experiment 5. The power input observed for experiment 5 show a maximum power of 0.35 kW, which is an increase of 0.1 kW from the maximum power observed in experiment 4. The power input ranged between 0.35 and 0.05 kW, while the heat flux ranged between 4.38 and 0.62 kW/m^2.

Figure 5.15 shows the cumulative energy stored along with the cumulative uncertainty associated with it. The cumulative energy stored for experiment 5 was 15.85 MJ ± 22.3%, the cumulative energy stored was closely aligned with the theoretical storage capacity, which confirms the confidence in the experimental results. The total charging time in order to bring the tank from an average temperature of 20 ± 2 °C to 55 ± 2 °C was 20.7 hours.

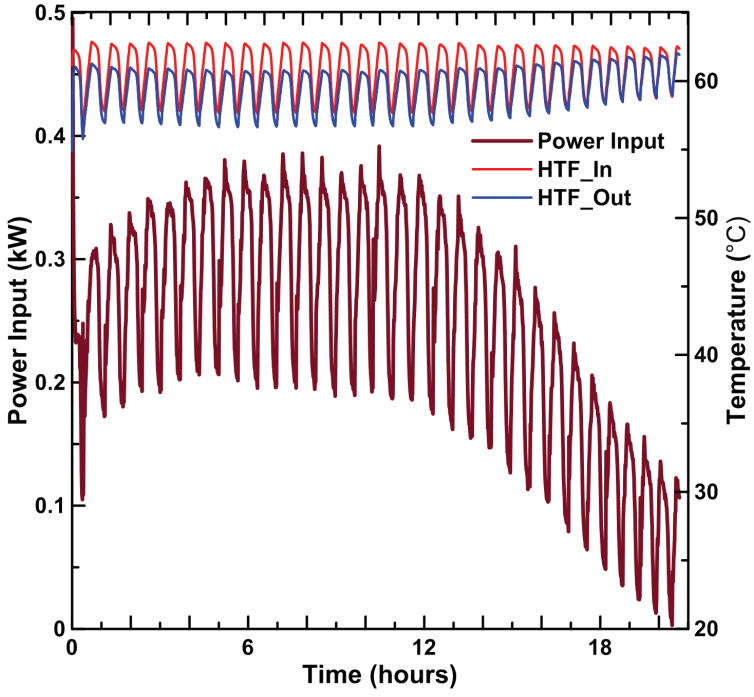

Figure 5.14 Power input as a function of time during charging experiment ($T_{H,in}$ = 60°C, 2.5 L/min)

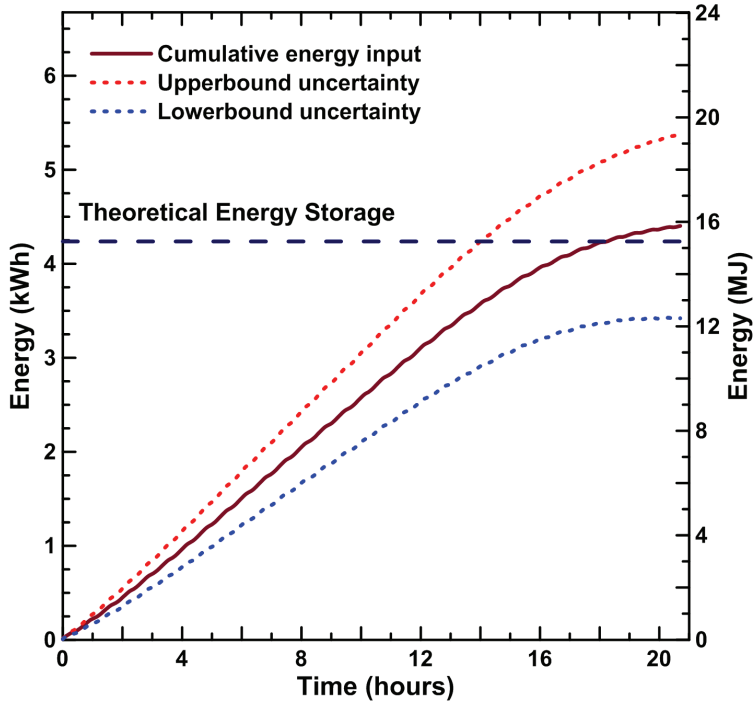

Figure 5.15 Cumulative energy as a function of time during charging experiment ($T_{H,in}$ = 60°C, 2.5 L/min)

The uncertainty was observed to increase with the decrease in the temperature difference between the HTF inlet and outlet. As discussed earlier, the uncertainty values of the experiments with 1.1, 1.5 and 2.5 L/min were 12, 14 and 22% respectively. Figure 5.16 shows the temperature difference between the HTF inlet and outlet for the three flow rates used in all three experiments. It can be observed that the lowest flow rate shows the highest temperature difference, which is due to the increase of residence time of the HTF in the heat exchanger. The value of such observation can be related to design considerations where for instance a solar collector efficiency decreases with a higher glycol inlet temperature.

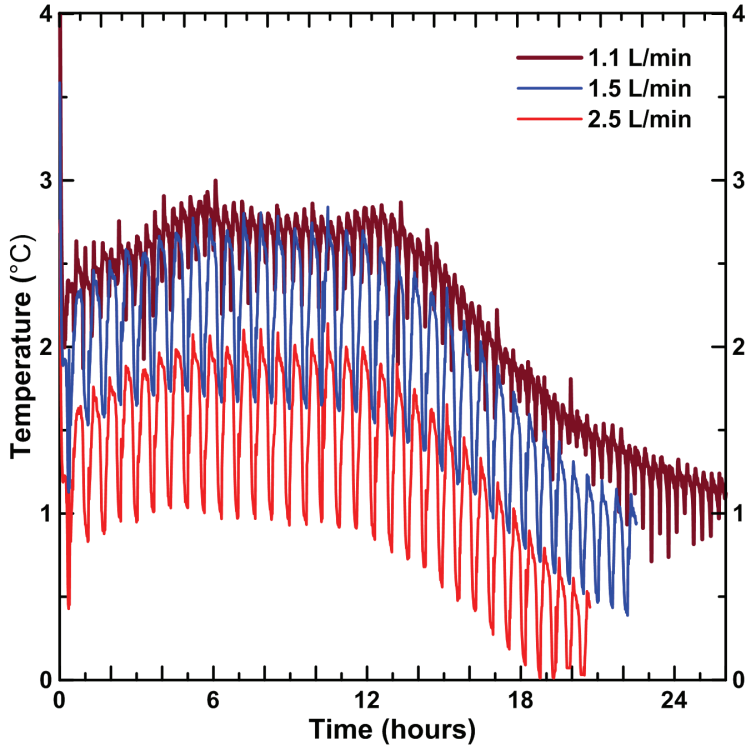

Figure 5.16 Temperature difference between the HTF inlet and outlet temperature for three flow rates at 1.1, 1.5, and 2.5 L/min

The effect of increasing the HTF flow rate on the overall performance of the system is not substantial. Hence, the internal thermal resistance due to forced convection does not play a huge role in the overall thermal resistance between the HTF and the PCM. Consequently, the increase of Re does not substantially improve heat transfer rates in this case. Even though reductions to charging time were observed, using the highest flow might not always be the most efficient solution particularly when taking into consideration the tradeoff between achieving slightly higher heat transfer rates or maintaining a higher solar collector efficiency in the case of a SDHW system. Therefore, the lowest flow rate might be the most reasonable for an application such as SDHW. Table 5.3 summarizes the results for the charging experiments conducted using various flow rates.

Table 5.3 Summary of results for charging experiments with various flow rates

Experiment	Power input range (kW)	Cumulative Energy stored (MJ)	Charging time (Hours)
1	0.2- 0.1	15.41 ± 13 %	26
4	0.25-0.1	15.35 ± 14.5 %	22
5	0.35-0.05	15.85 ± 22.3%	20.7

5.2 CHARGING: REAL-TIME SOLAR

The LHESS was operated under real-time solar conditions over a 10 months period, from November 2013 to August 2014, in order to observe the variations of solar charging conditions. The experimental setup was initially on ground level where several solar collectors were available for research purposes. However, the location tended to experience shading in the early times of the day and late afternoon. The setup used on the ground was moved to the roof in July 2014, in order to capture an ideal solar day without the effect of shading. The selected days attempt to portray the representative characteristic of a given day in a particular season. Needless to say, it is challenging to represent a season in a day, however the days selected show a range of solar conditions that captures the various solar conditions present throughout the year.

Table 5.4 List of experiments conducted for Real-time solar charging

Solar day date	Location in Thesis	Flow rate	Day length
November 24th 2013	Section 5.2.1	0.7 L/min	6 hours
February 11th 2014	Section 5.2.2	0.7 L/min	5 hours
March 4th 2014	Section 5.2.3	0.7 L/min	5.6 hours
July 12th 2014	Section 5.2.4	0.7 L/min	11.45 hours

5.2.1 November 2013

Data was collected on the day of November 24th, 2013. Figure 5.17 shows the measured solar insolation data at the testing location. The shading effect can be clearly observed in Fig. 5.17a), which unsurprisingly decreases the available solar energy to the system.

The time zero in Fig. 5.17b) signifies the turning on of the pump after shading was no longer observed. A typical fall day in NS is characterized by partial overcast and short day-length conditions. November 24th meets these criteria as shown below. The temperature profiles observed within the storage tank provided insight into the behavior of the PCM. Figure 5.18 shows the temperature profiles of all 12 thermocouples present in the tank. It is clear that the majority of the PCM present in the tank remained in the solid phase. The onset of natural convection observed in the experiments discussed in section 5.1 could not be reached which limited the overall performance of the heat transfer process. The temperature probes showing the highest temperatures were T2, T8, T10 and T11. T2 is located directly next to the glycol straight copper section, T8 is located at the depth of the 4th turn of the glycol coil, T10 was located in between the 2nd and 3rd turn of the glycol coil, while T11 is located right next to the edge of the outer surface of the coil.

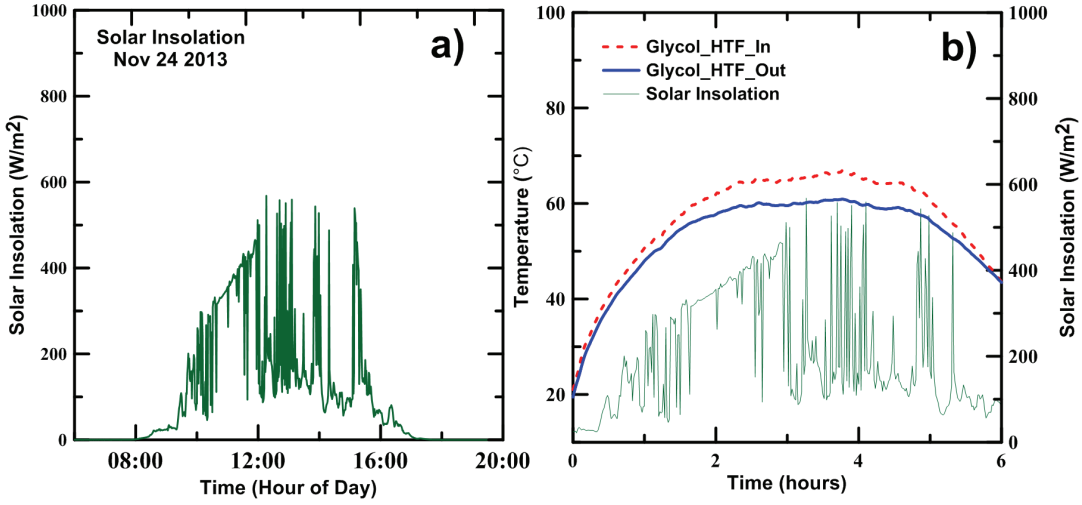

Figure 5.17 a) Solar insolation on November 24th 2013, b) Glycol inlet/outlet temperatures relatively to solar insolation

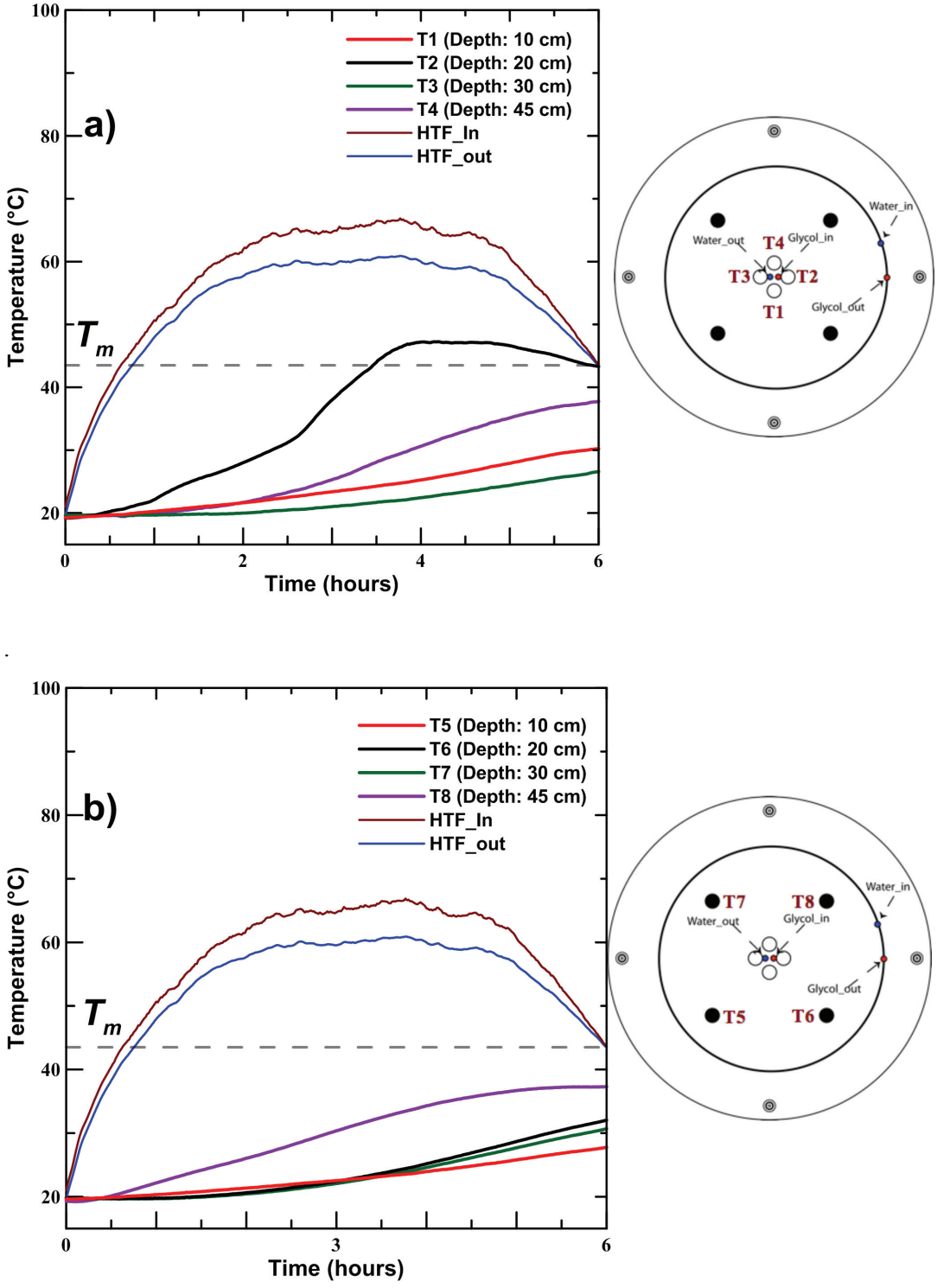

Figure 5.18 Temperature profiles as a function of time on November 24th 2013: a) Inner probes T1 to T4 b) Middle probes T5 to T8

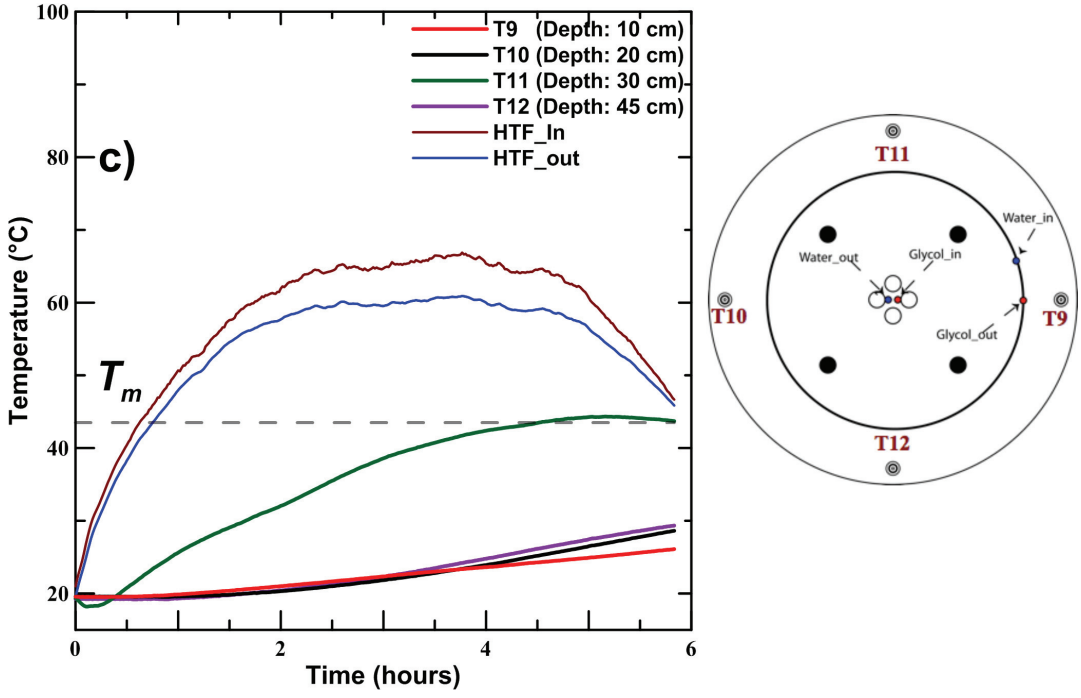

Figure 5.18 Temperature profiles as a function of time on November 24th 2013: c) Outer probes T9 to T12, continued

Figure 5.19 shows the power input and the HTF inlet and outlet temperatures over the whole charging period. For November 24th, the peak power input observed was 0.25 kW and the cumulative energy stored was 3.5 MJ (< 1 kWh) with an uncertainty of 25% as shown in Fig. 5.20. The power input increases with the increase of the HTF inlet temperatures, however the solar insolation was so poor for that day that a substantial charge was not achieved.

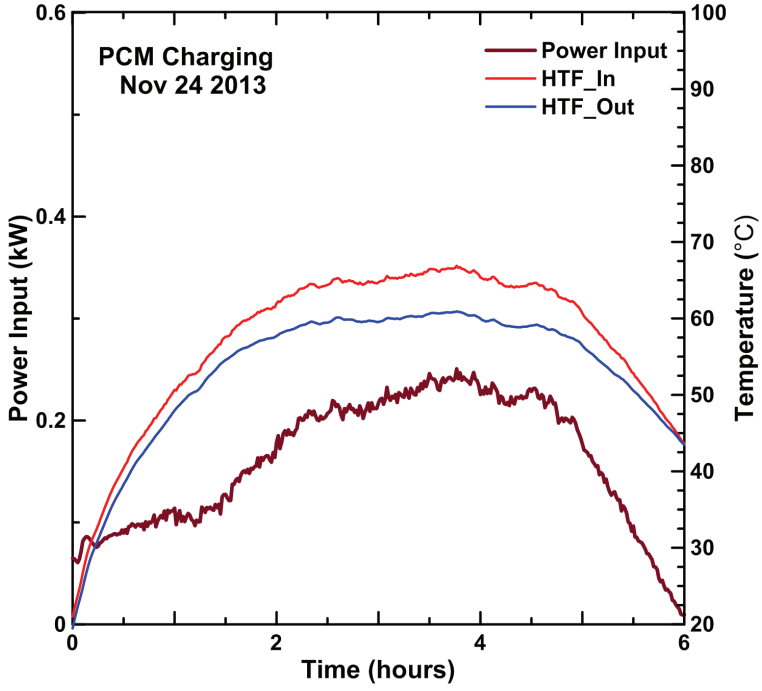

Figure 5.19 Power input and HTF inlet and outlet temperatures as a function of time during PCM charging on November 24th 2013.

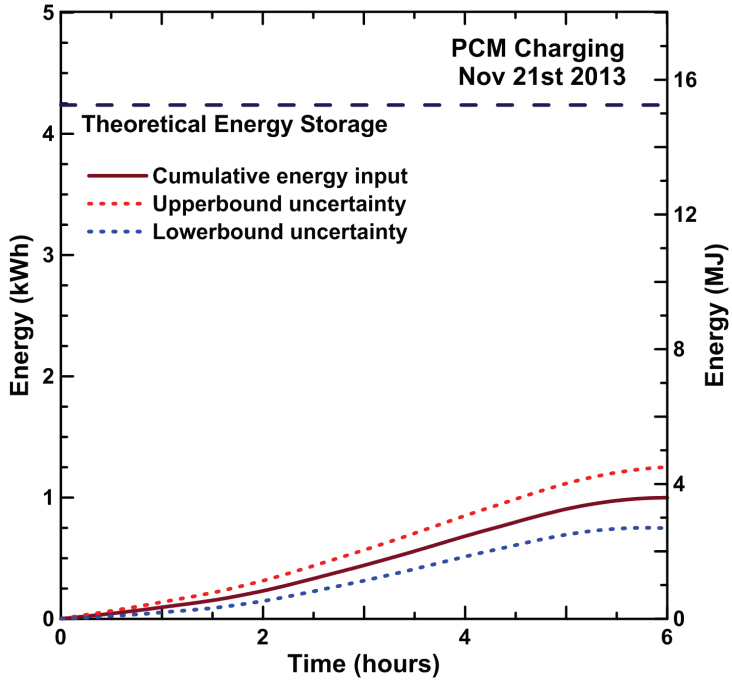

Figure 5.20 Cumulative energy stored throughout the solar charge on November 24th 2013

5.2.2 February 2014

Data was collected on the day of February 11th, 2014. Figure 5.21 shows the measured solar insolation data at the testing location. The experimental setup was still at the initial ground location which explains the shading seen in the solar insolation. One way of understanding the performance of the system on that given day can be analyzed by looking at the temperature profiles of the tank. Figure 5.22 shows the temperature profiles for all thermocouples in the tank. Even though this day is more overcast than the day observed in November, the glycol temperature reaches higher values by approximately 5 °C. Figure 5.22a) shows an interesting profile of the probe T1. As seen in the previous solar day in November, the probe T1 did not get close to the melting temperature, however higher glycol inlet temperatures can cause faster melting around the coil which could have contributed to more natural convection than was present in November. It is observed that the HTF inlet temperature becomes lower than HTF outlet temperature, which actually takes away energy from the system in lieu of storing it. This occurs where the temperature of the glycol loop drops below the temperature of the tank, and thus it is observed that the temperature at T1 goes back down during that period from hours 3 to 6. Applying a proper control strategy can provide a solution for this issue.

The temperature profiles of the middle probes remain below the melting temperature similarly to the day in November. However, as opposed to witnessing a high temperature for T8, the temperature profiles of T5-T8 in Fig. 5.22b) shows more of a vertical stratification, which reiterates the initial observations regarding an earlier onset of natural convection due to higher glycol temperatures.

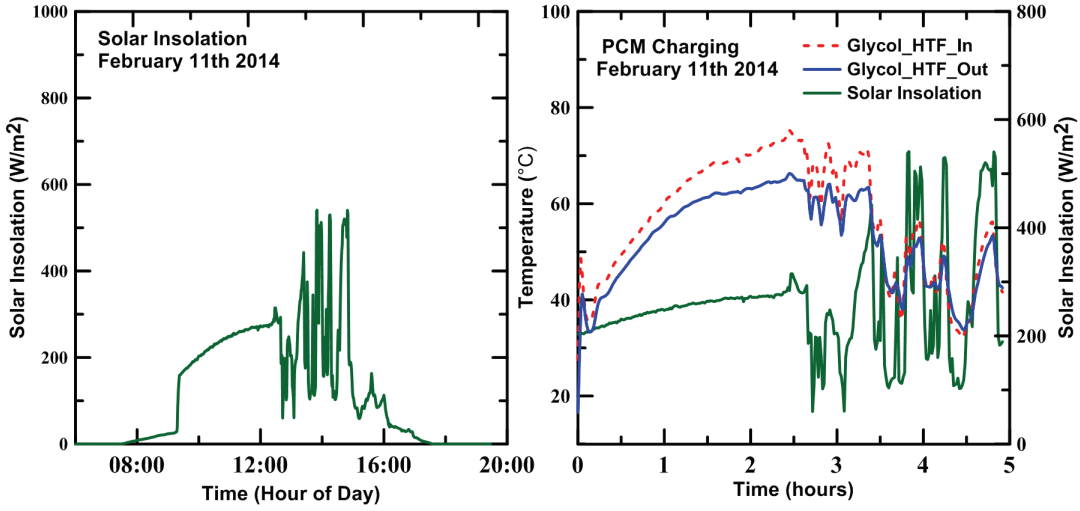

Figure 5.21 a) Solar insolation on February 11th 2014, b) Glycol inlet/outlet temperatures relatively to solar insolation

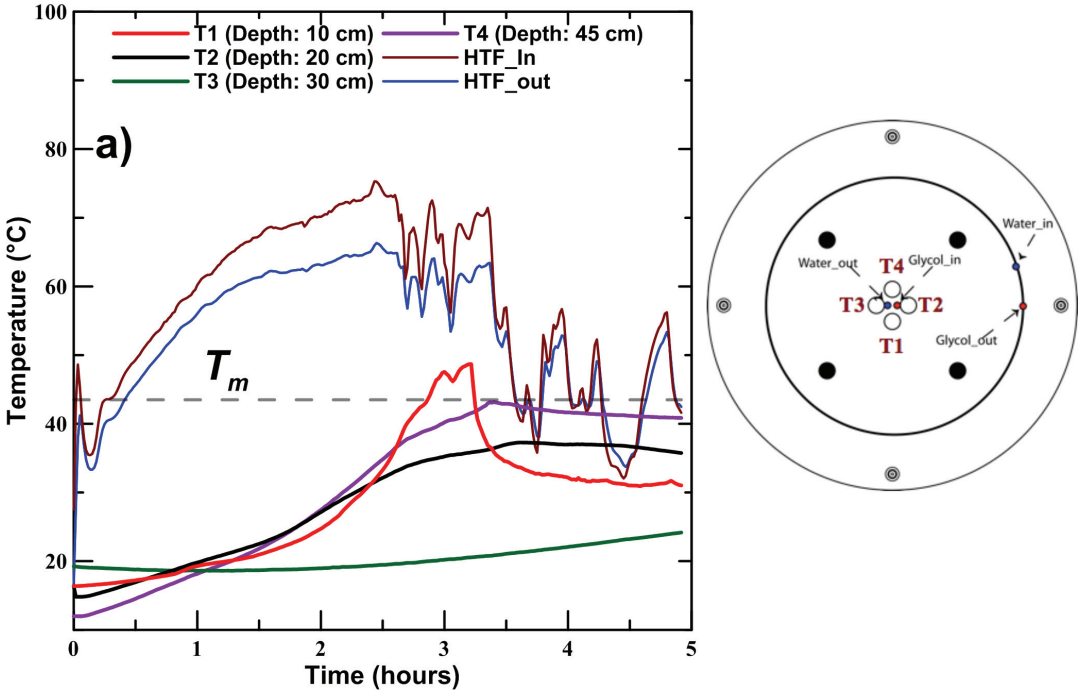

Figure 5.22 Temperature profiles as a function of time on February 11th 2014: a) Inner probes T1 to T4

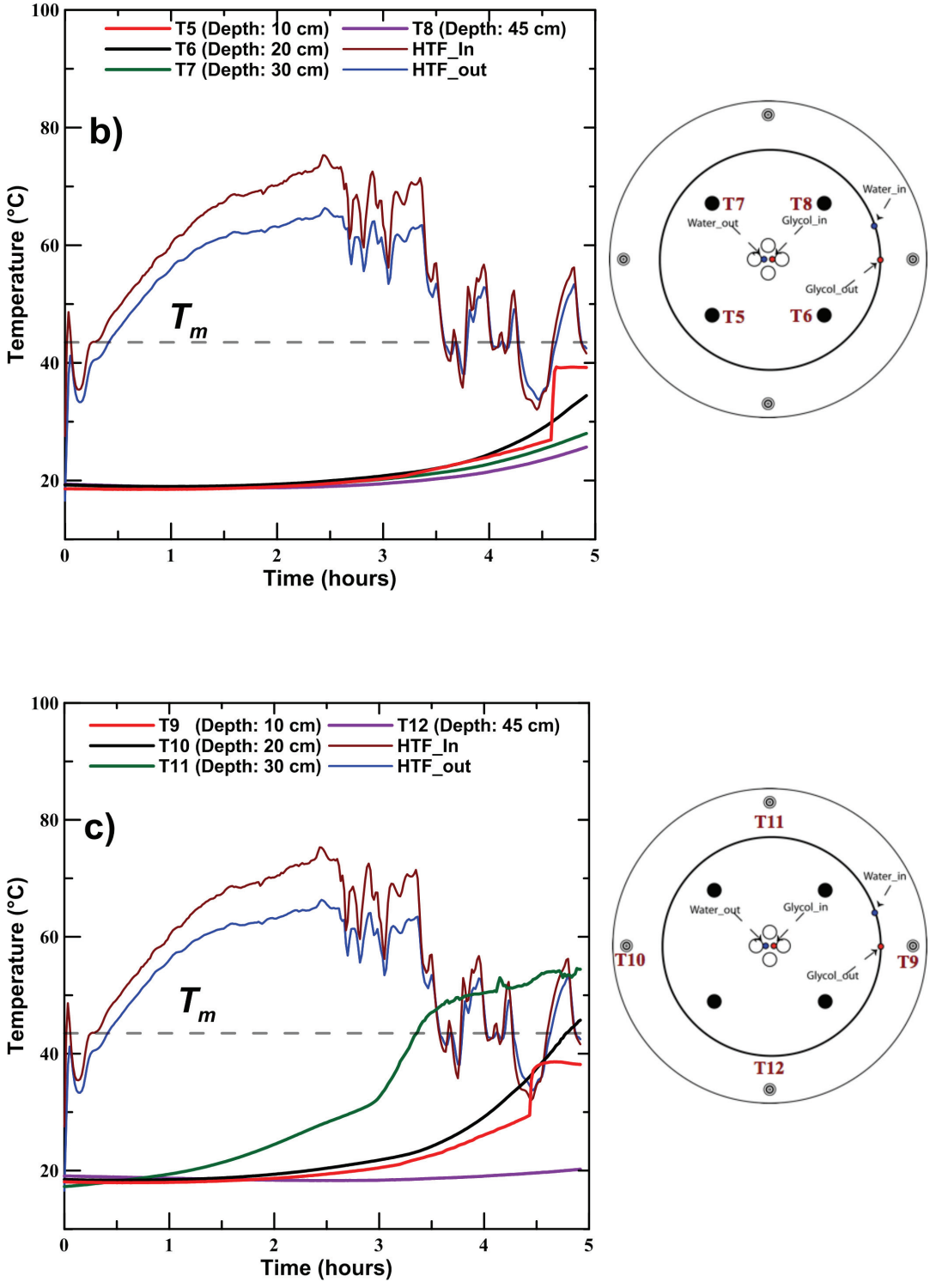

Figure 5.23 Temperature profiles as a function of time on February 11th 2014: b) Middle probes T5 to T8 c) Outer probes T9 to T12, continued

The outer probes shown in Fig. 5.22c) follow a similar profile to the one observed in November. One possible explanation that the outer probes were not affected by natural convection is that the heat transfer to the outer probes as shown in section 5.1 is dominated by radial conduction during the early stages of the process. However, similarly to the observed day in November, T11 melts due to its location next the glycol coil at the bottom of the tank where the HTF is warmest.

Figure 5.24 shows the power input and the HTF inlet and outlet temperatures over the whole charging period for February 11th. The peak power input observed was 0.38 kW, and the cumulative energy stored was 3.25 MJ (< 1 kWh) with an uncertainty of 23% as shown in Fig. 5.25. The power input tracks the profile of the HTF inlet temperatures and outlet temperatures, noting that at parts of the process the power input is a negative value, which indicates heat loss from the tank as opposed to heat gain. This explains the lower cumulative energy stored throughout the process in comparison to November even though higher heat transfer rates were achieved. Obviously, a control strategy would need to be in place in such a system in order to avoid such scenarios. However for the purpose of this study, it is part of the experiment to observe such scenarios, in order to quantify their effects on the LHESS performance.

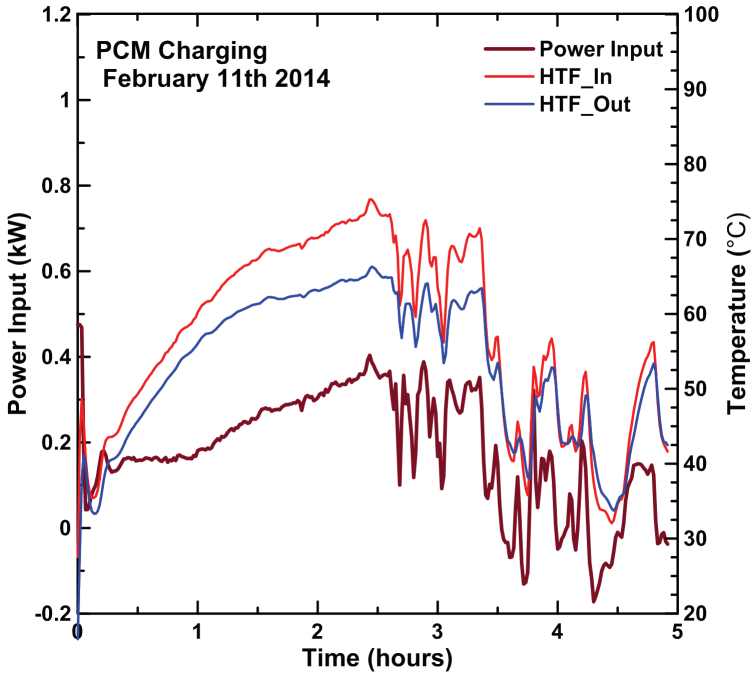

Figure 5.24 Power input and HTF inlet and outlet temperatures as a function of time during PCM charging on February 11th 2014.

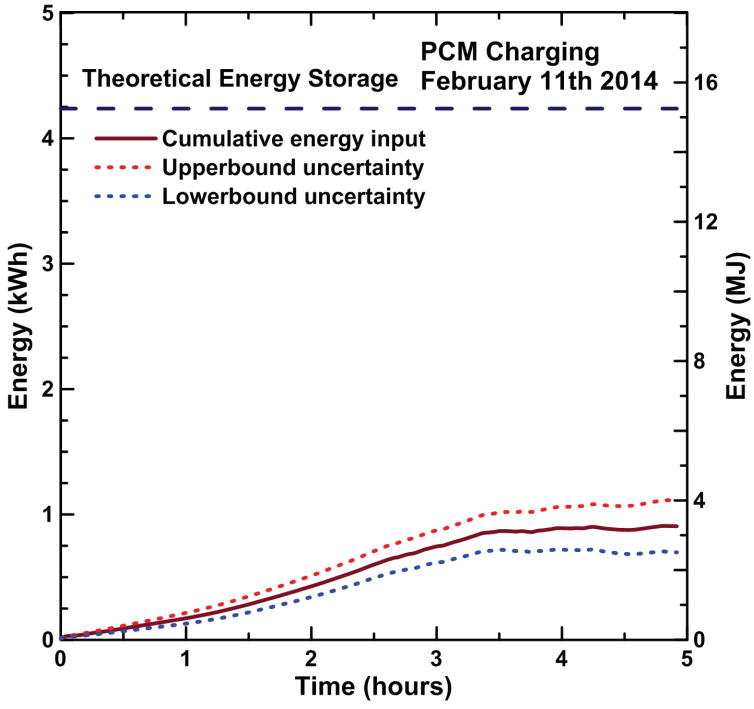

Figure 5.25 Cumulative energy stored as a function of time during PCM charging on February 11th 2014.

5.2.3 March 2014

Data collected on March 4th 2014 illustrates the real-time solar charging during higher insolation solar winter conditions. As it can be seen in Fig. 5.26, the solar insolation indicates a clear day with a maximum insolation reaching 700 W/m^2 at solar noon. The effects of shading are still present and impeded the general performance of the system.

Figure 5.27 shows the temperature profiles of the probes in the tank. Probes at a lower depth in the tank (T4 and T11) can be observed to reach melting after approximately 2 hours. The glycol HTF enters through the straight copper and therefore it is hottest at the bottom of the tank. The middle probes (T5 to T8) do not show any melting. The general state of the tank showed more melting than that observed during November and February, however it can be seen that most of the probes still measure temperature lower than the melting temperature showing the most of the PCM remains in the solid phase, and the latent thermal capacity of it is not fully engaged.

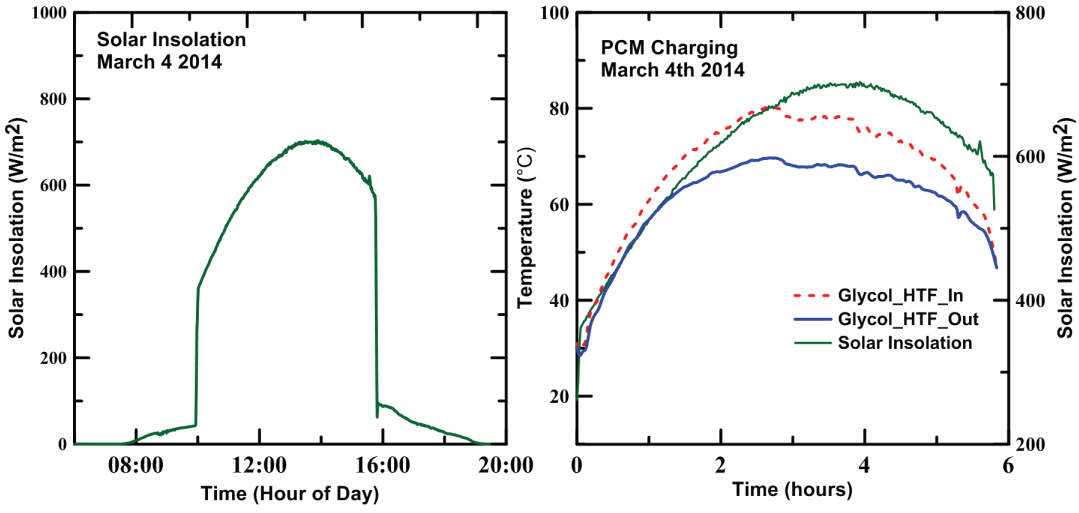

Figure 5.26 a) Solar insolation on March 4th 2014 at NSCC campus, b) Glycol inlet/outlet temperatures relatively to solar insolation

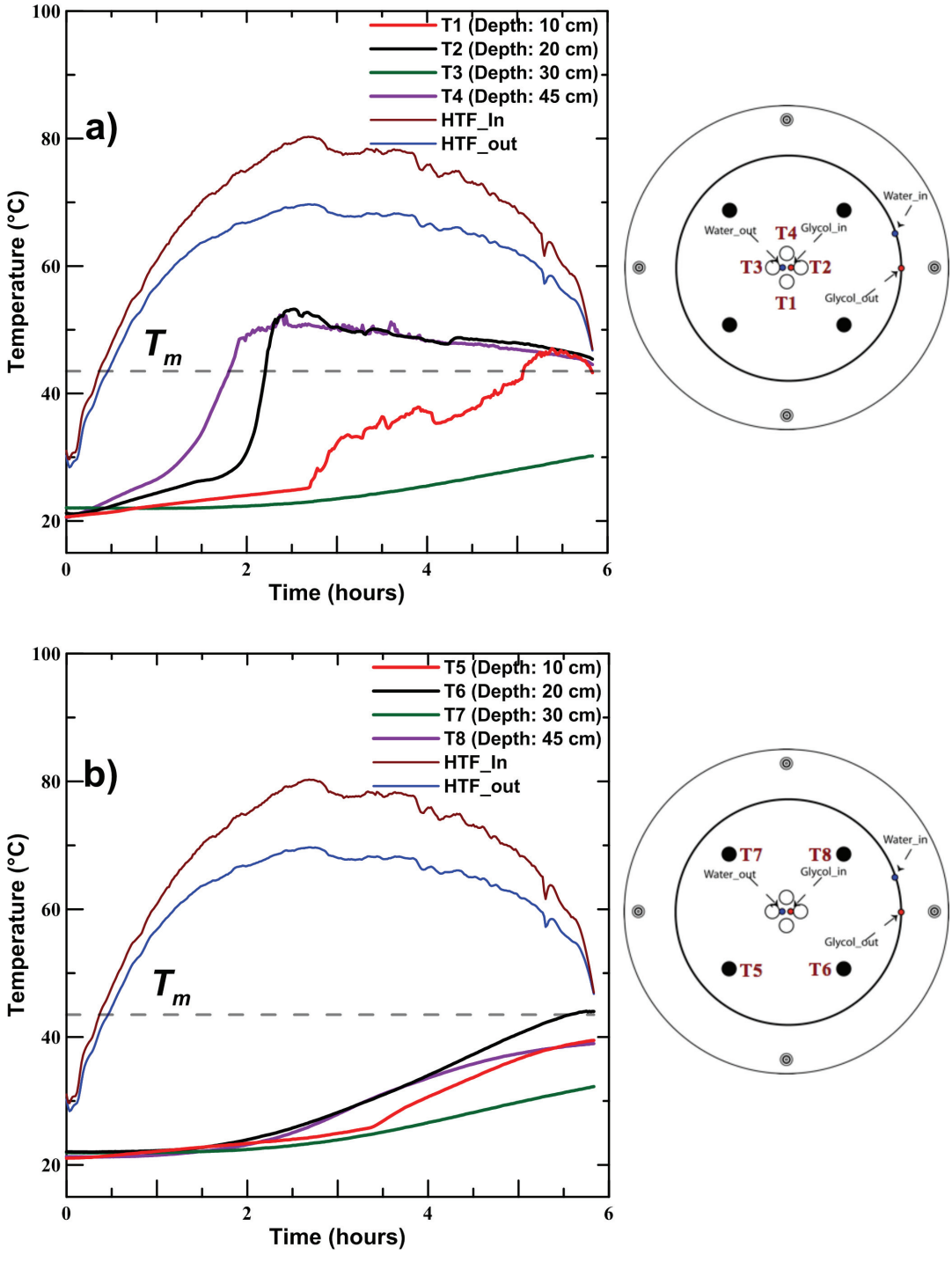

Figure 5.26 Temperature profiles as a function of time on March 4th 2014: a) Inner probes T1 to T4 b) Middle probes T5 to T8

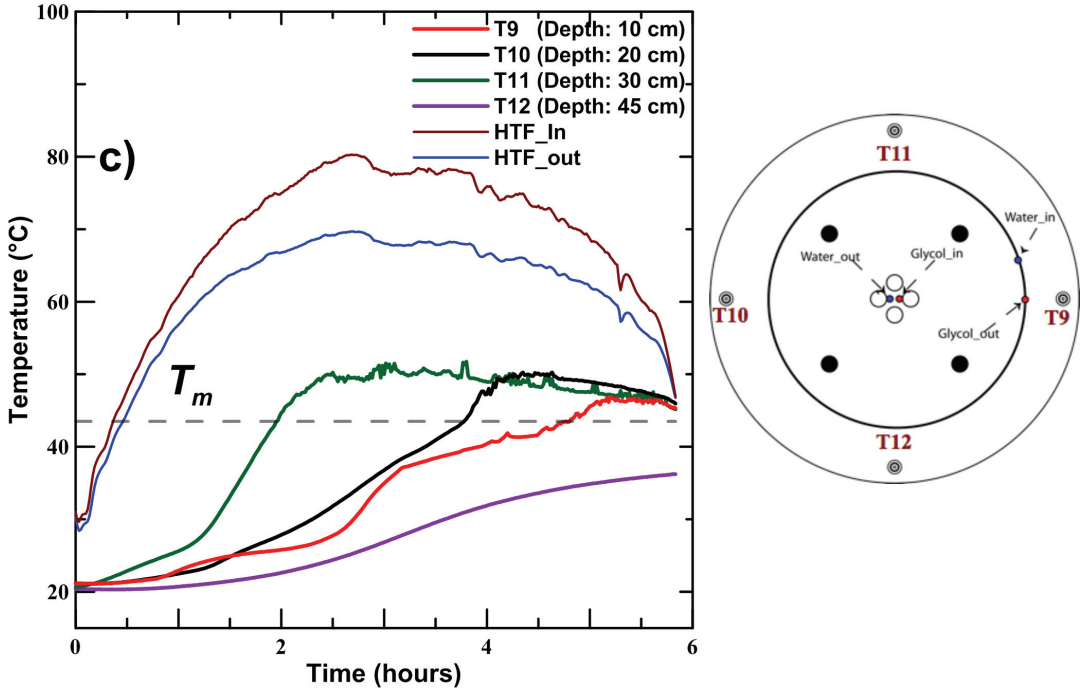

Figure 5.27 Temperature profiles as a function of time on March 4th 2014: c) Outer probes T9 to T12, continued

Figure 5.28 shows the power input and the HTF inlet and outlet temperatures over the whole charging period for March 4th. The peak power input observed was 0.44 kW and the cumulative energy stored was 6.30 MJ (1.75 kWh) with an uncertainty of 15% as shown in Fig. 5.29. The power input tracks the profile of the HTF inlet temperatures and outlet temperatures.

The performance on this clear March day was proved to be better than the days observed in November and February, however the rates at which the heat was transferred were not sufficient, and the tank only stored 41 % of the overall maximum storage capacity of the LHESS.

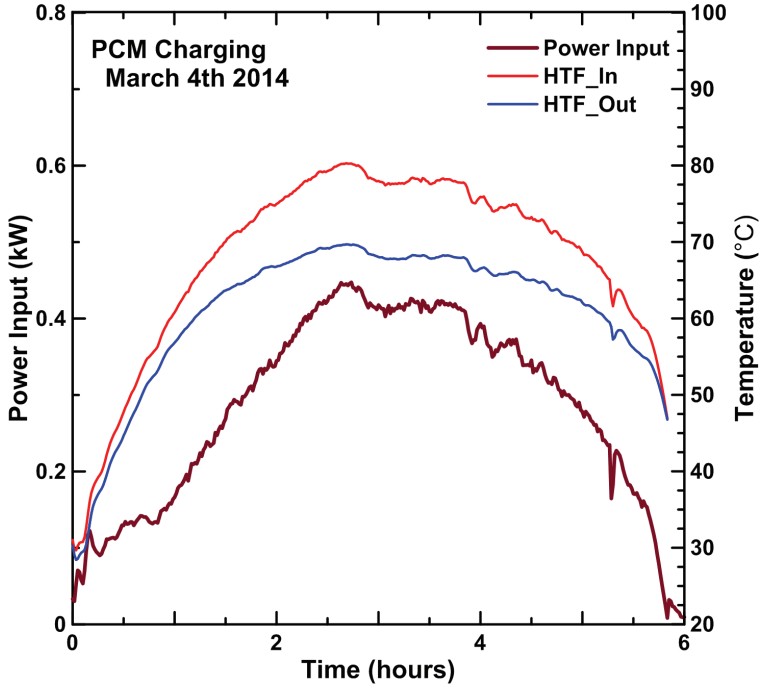

Figure 5.28 Power input and HTF inlet and outlet temperatures as a function of time during PCM charging on March 4th 2014.

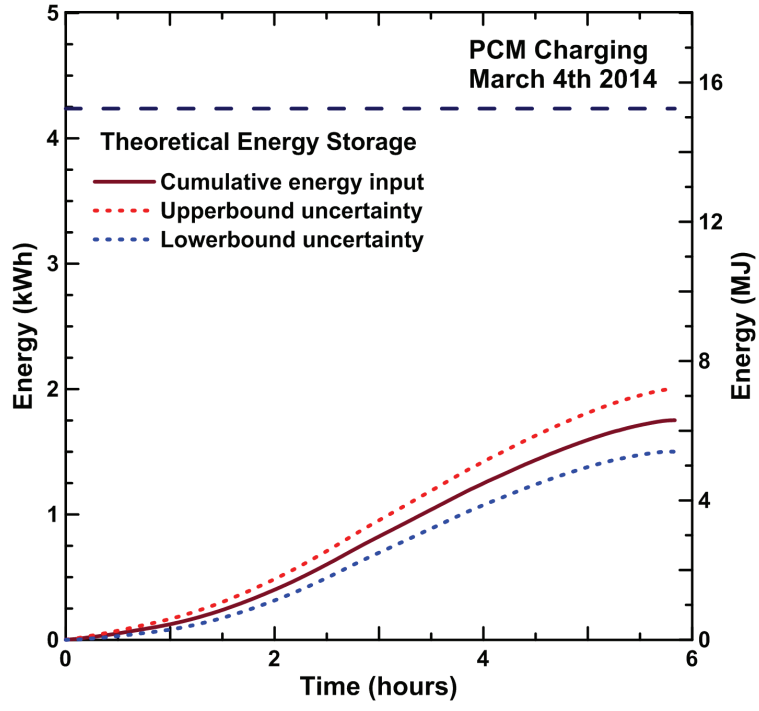

Figure 5.29 Cumulative energy stored as a function of time during PCM charging on March 4th 2014.

5.2.4 July 2014

Test conducted on July 12th 2014 demonstrated system behavior under nearly ideal clear-sky summer conditions. The test was conducted at the new roof location of the solar collector, which helped eliminate the shading effects. The solar insolation shown in Fig. 5.30 shows an ideal solar day with a maximum insulation value of 925 W/m^2. The temperature profiles shown in Fig. 5.31 show melting in 15 probes with the exception of the probe T12 which is located at the bottom outer edge of the tank. The observation is consistent with the findings from the tank characterization where it was found that T12 was the last probe to undergo melting. The first probe to undergo melting was T4, which is located near the coil at the bottom of the tank, thus it is exposed to the highest temperature differential. Despite showing a closely aligned trend, the thermocouples at the top (T1, T5, T9) show a brief anomaly. The thermocouple T1 showed an unusual trend during the phase change stage. The temperature readings of T1 went above the melting temperature, only then to drop below it and follow closely thermocouples T5 and T9, which in itself is indicative of even distribution of energy at the top of tank through natural convection. One probable explanation for the anomaly is the shifting of a solid material or the presence of an air cavity around the thermocouple.

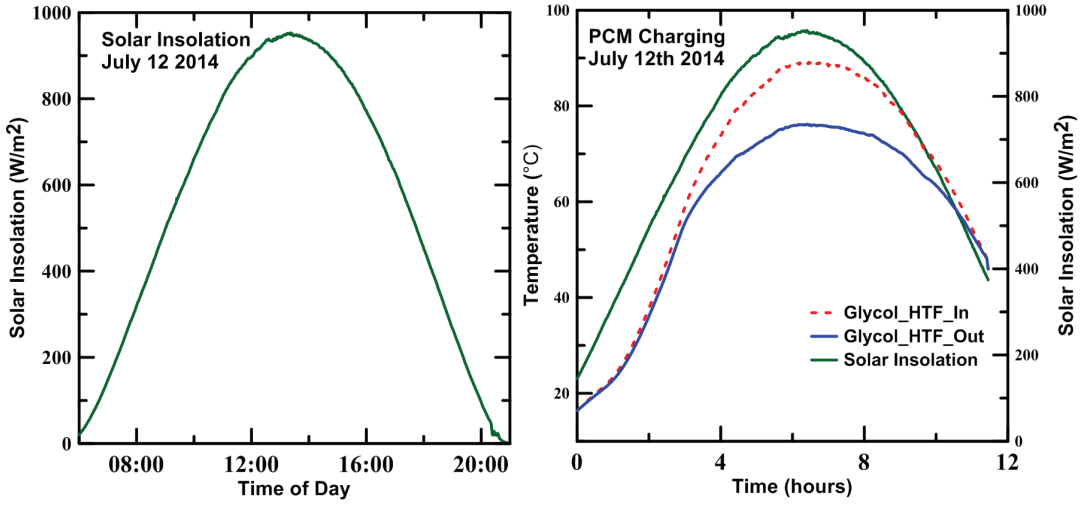

Figure 5.30 a) Solar insolation on July 12th 2014, b) Glycol inlet/outlet temperatures relatively to solar insolation

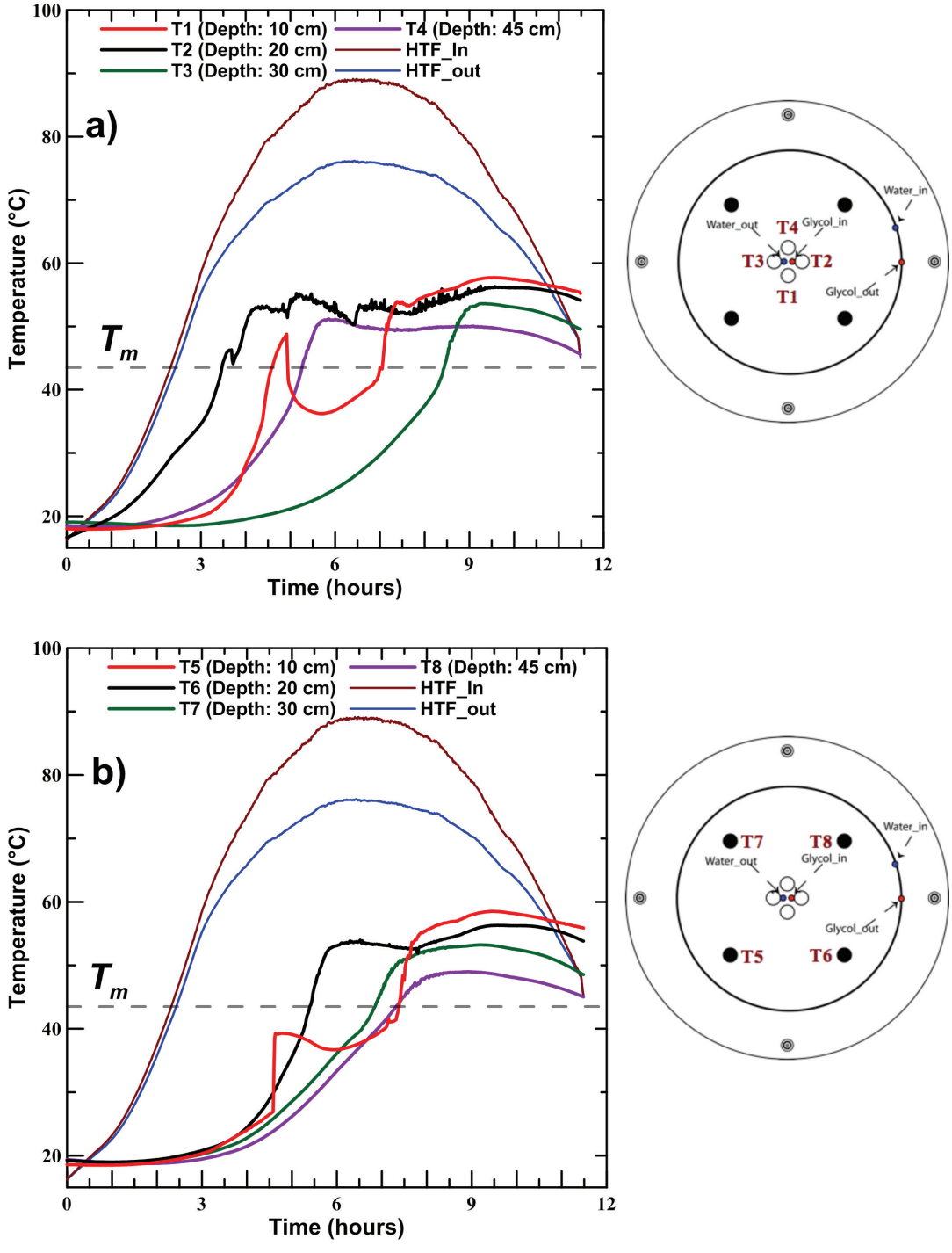

Figure 5.30 Temperature profiles as a function of time on July 12th 2014: a) Inner probes T1 to T4 b) Middle probes T5 to T8

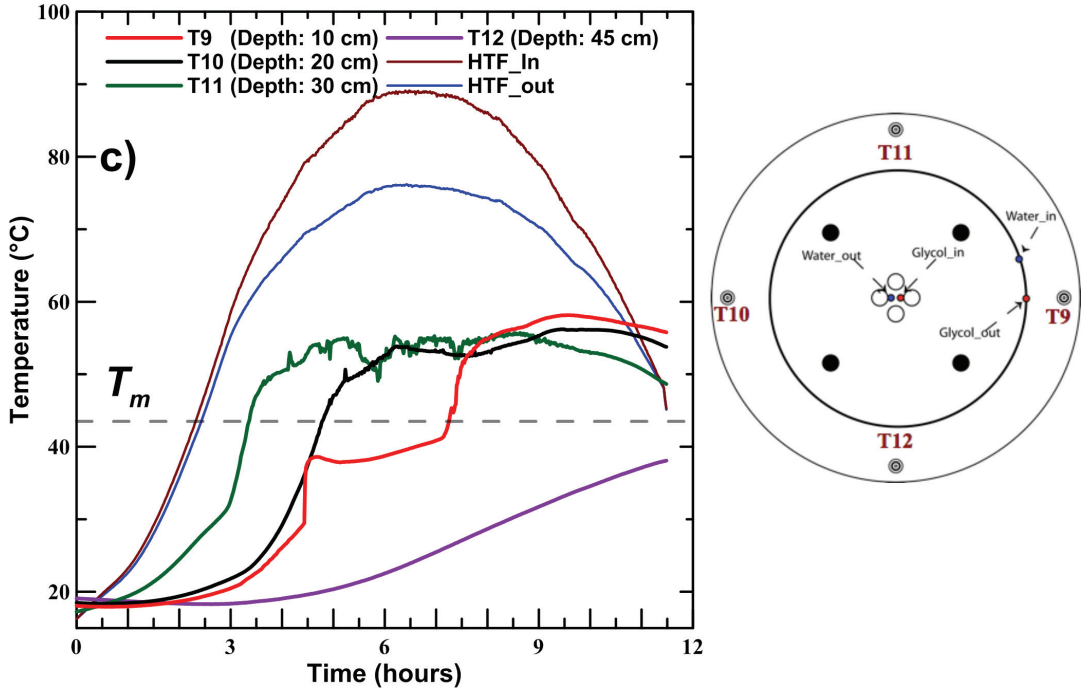

Figure 5.31 Temperature profiles as a function of time on July 12th 2014: c) Outer probes T9 to T12, continued

Figures 5.32 and 5.33 show the power input and cumulative energy storage respectively for the solar charging on July 12th 2014. The peak power input was 0.55 kW, which coincided with the peak solar insolation. The cumulative energy transferred to the system was 12 MJ with an uncertainty of 15%. The amount of energy stored under ideal solar conditions substantially improved in comparison with earlier dates with poorer conditions, with increases of approximately 300% and 100% in energy stored relatively to the November and March test days, respectively. However, the tank was not fully charged and had a charge percentage of 78%.

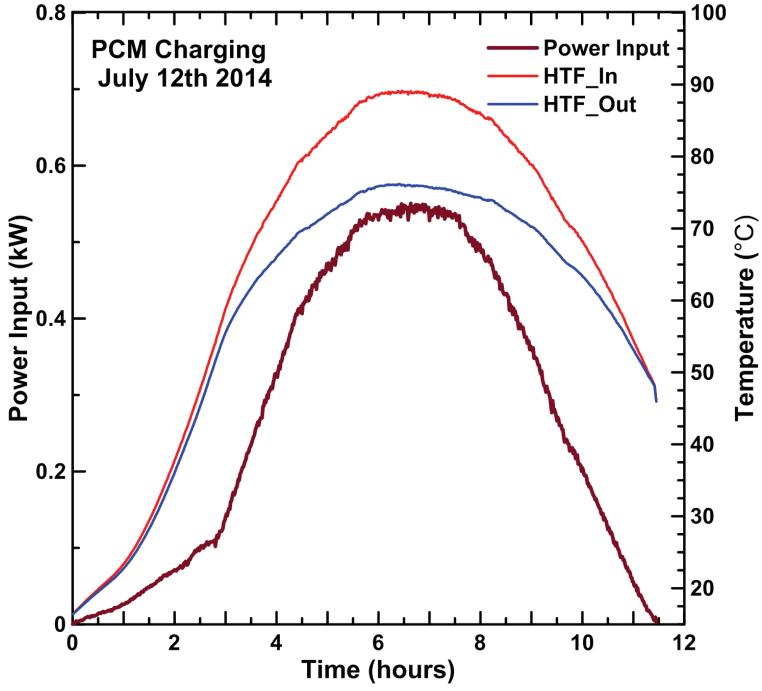

Figure 5.32 Power input and HTF inlet and outlet temperatures as a function of time during PCM charging on July 12th 2014.

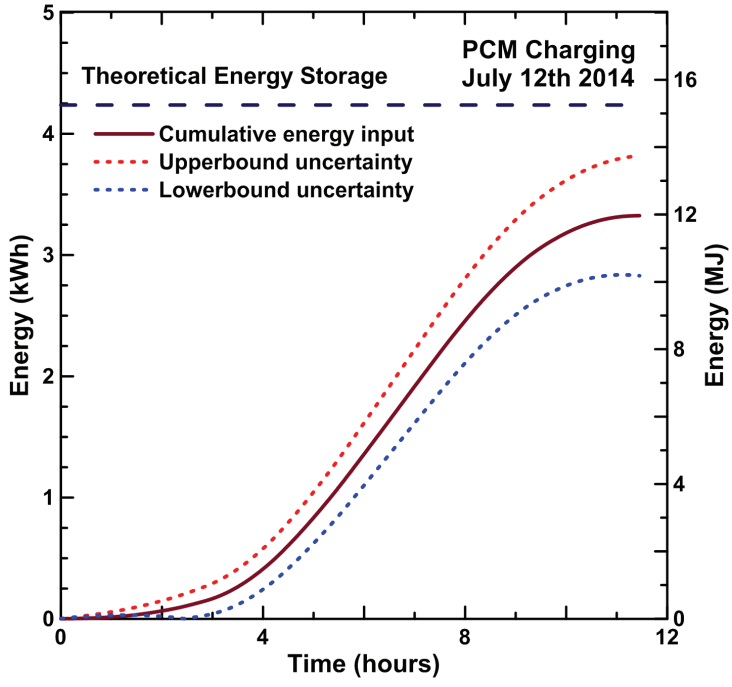

Figure 5.33 Cumulative energy stored as a function of time during PCM charging on July 12th 2014.

Table 5.5 shows a summary of the results on the real-time solar charging conducted on the tank, with the peak power input and cumulative energy stored over the charging period.

Table 5.5 Summary of the real-time solar charging results for various days

Solar day date	Peak Power input	Cumulative energy stored
November 24th 2013	0.25 kW	3.50 MJ ± 25 %
February 11th 2014	0.38 kW	3.25 MJ ± 23 %
March 4th 2014	0.44 kW	6.30 MJ ± 15 %
July 12th 2014	0.55 kW	12.02 MJ ± 15 %

5.3 MUNICIPAL DISCHARGE

The discharge process for the LHESS was conducted running municipal water through the heat exchanger and exiting to a drain. The conditions of the water were dependent on uncontrollable parameters such as the weather conditions and the instantaneous use of water in the building. This section presents two experiments, which possess different conditions. The experiments are not directly comparable, however they do show insight regarding the effect of the HTF inlet temperature and flow rate on the discharge process. The experiments are described in Table 5.2. The Stefan number values are 0.49 and 0.42 for experiments 6 and 7, respectively.

Table 5.6 List of experiments conducted during discharge and the parameters used

Experiment Number	Location in Thesis	Flow Rate	Average HTF Temperature
6	Section 5.3.1	1.5 ±0.02 L/min	9 ± 0.45 °C
7	Section 5.3.2	2.6 ±0.02 L/min	16 ± 0.45 °C

Figure 5.34 shows the temperature profiles of all 12 probes located in the tank during discharging for experiment 6. The time scale for discharging was significantly longer than the charging process as shown later in the section. During solidification all probes exhibited a constant temperature plateau at the solidification temperature. The time

length of the plateau differed based on the location of the probe and its proximity to the heat exchange surface. The water entered through the coiled part and exited through the straight copper therefore certain thermocouples near the top showed faster solidification such as T1, T2 and T5. Other probes are in close proximity in the radial direction to the heat source and exhibit solidification at very fast rates, such as T2 (same depth as the 1st turn of the water coil), T1 (next to the straight copper tubing), and T4 (same depth as 4th turn of the water coil). The profiles indicate that natural convection does not play a visible role during the solidification process since the temperature profiles are not dependent on the height of the thermocouple but more on the radial position. At 20 cm in depth, T2 takes 2 hours to solidify, while T6 takes 32 hours, and T10 takes 28 hours.

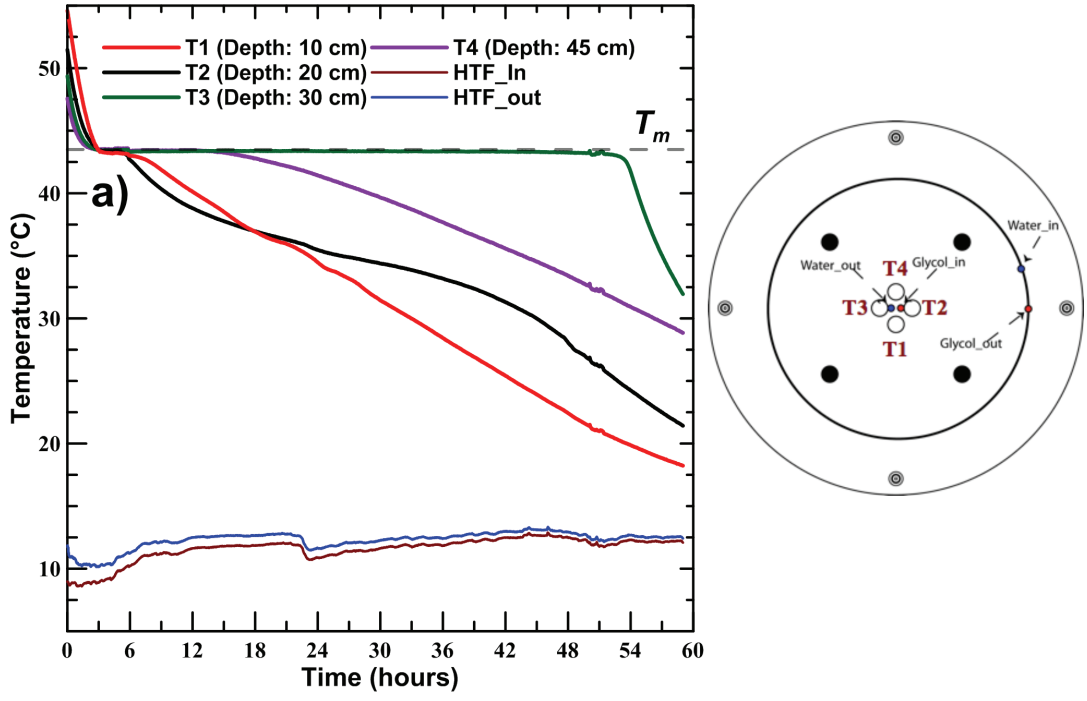

Figure 5.34 Temperature profiles as a function of time measured during discharging ($T_{C,in}$ = 9 °C, 1.5 L/min) : a) Inner probes T1 to T4

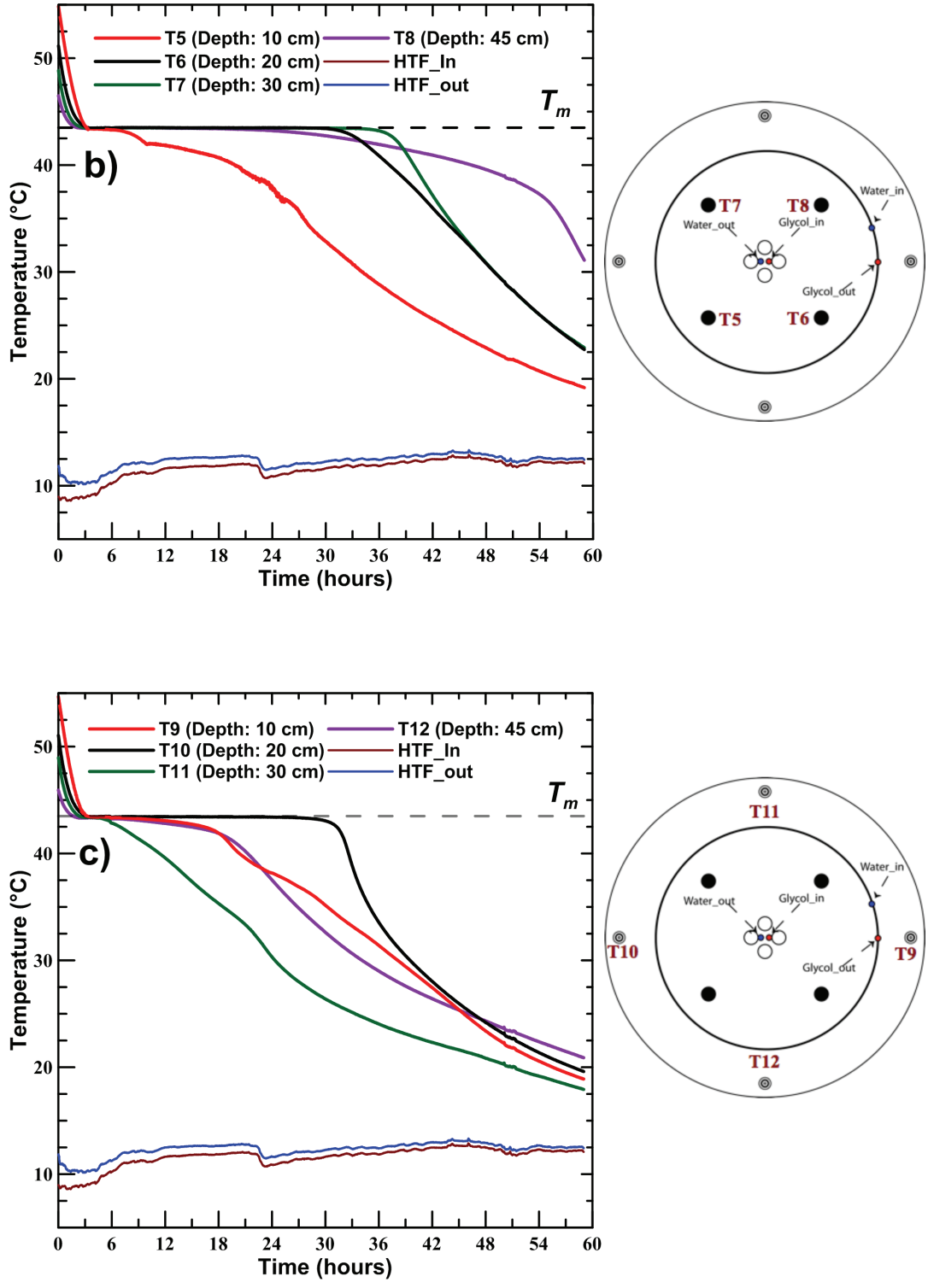

Figure 5.34 Temperature profiles as a function of time measured during discharging ($T_{C,in}$ = 9 °C, 1.5 L/min) : b) Middle probes T5 to T8, c) Outer probes T9 to T12, continued

Figure 5.35 shows the power input as a function of time, along with the HTF inlet and outlet temperatures. The power output shows a decreasing trend with time, which can be explained by the ever-increasing amount of solid PCM forming around the heat exchanger surface with time. The maximum power output starts at 0.3 kW and drops asymptotically to 0.04 kW. The total discharge time was observed to be 59 hours.

Figure 5.36 shows the amount of energy recovered over time. The amount recovered is closely aligned with the theoretical storage capacity and was 15.7 MJ. The uncertainty associated with the energy recovered was 56%. As it is seen in Fig. 5.33, the temperature difference between the HTF inlet and outlet are especially low, and given the measurement uncertainty on the thermocouples the accumulated uncertainty is expected to be unreasonably high. However, the proximity of the total energy recovered to theoretical storage capacity increases the confidence in the results.

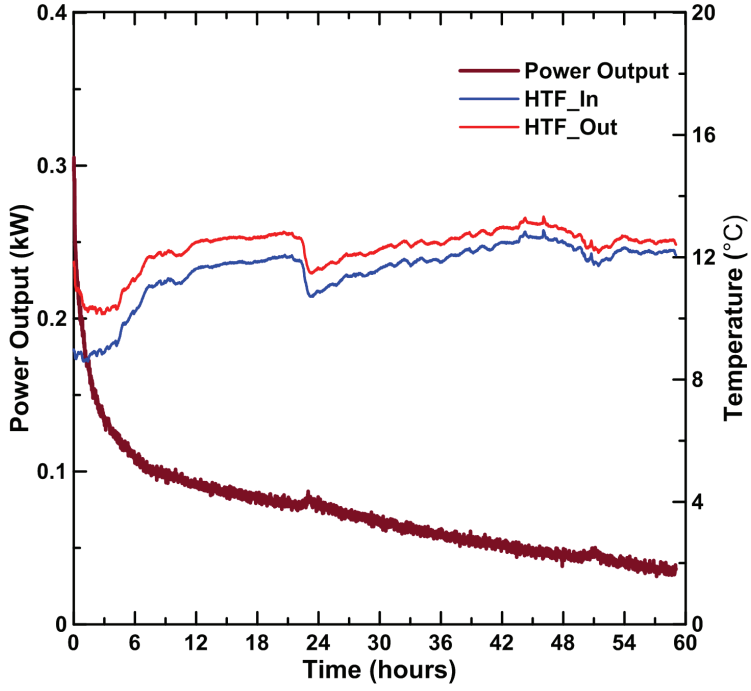

Figure 5.35 Power output as a function of time during discharging experiment ($T_{C,in}$ = 9 °C, 1.5 L/min)

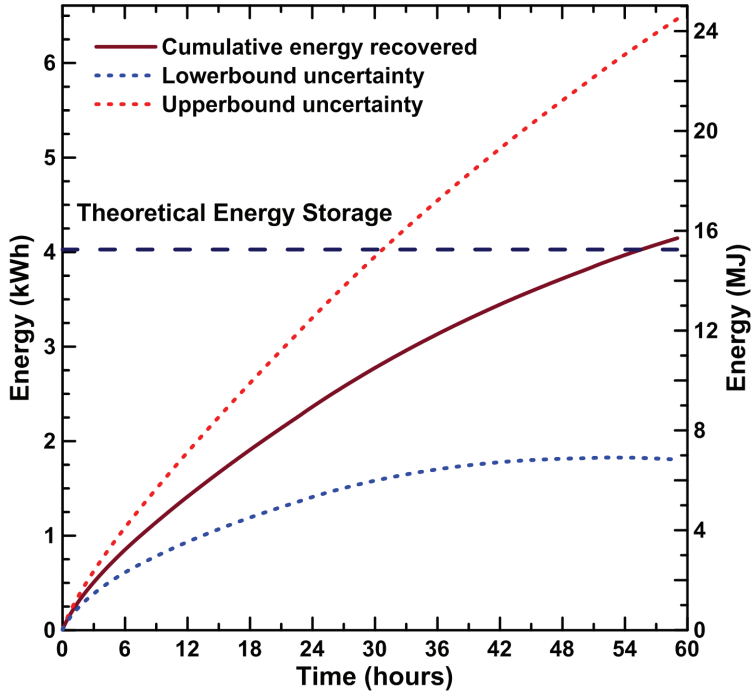

Figure 5.36 Cumulative energy recovered as a function of time during discharging experiment ($T_{C,in}$ = 9 ºC, 1.5 L/min)

Figure 5.37 shows the temperature profiles of all 12 probes located in the tank during discharging for experiment 7. The trend of the temperature profiles was consistent between the two experiments. However, in some cases, the plateaus lasted longer which could be caused by the lower heat transfer rate due to the lower temperature difference between the heat transfer fluid and the PCM. Therefore, the increase in HTF inlet temperature reduces heat transfer rates, while an increase in the flow rate has the potential to increase them.

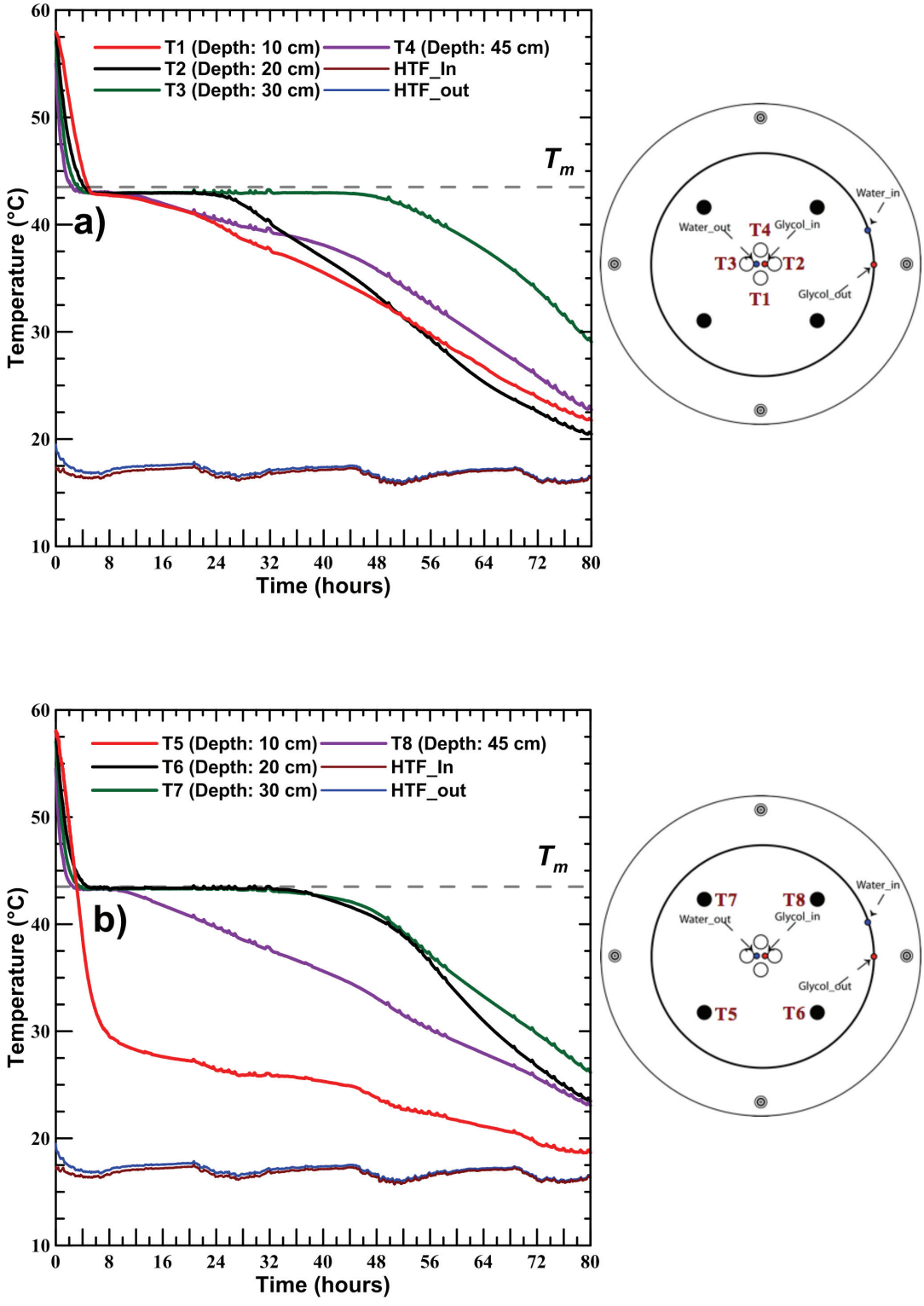

Figure 5.36 Temperature profiles as a function of time measured during discharging ($T_{C,in}$ = 16°C, 2.5 L/min): a) Inner probes T1 to T4, b) Middle probes T5 to T8

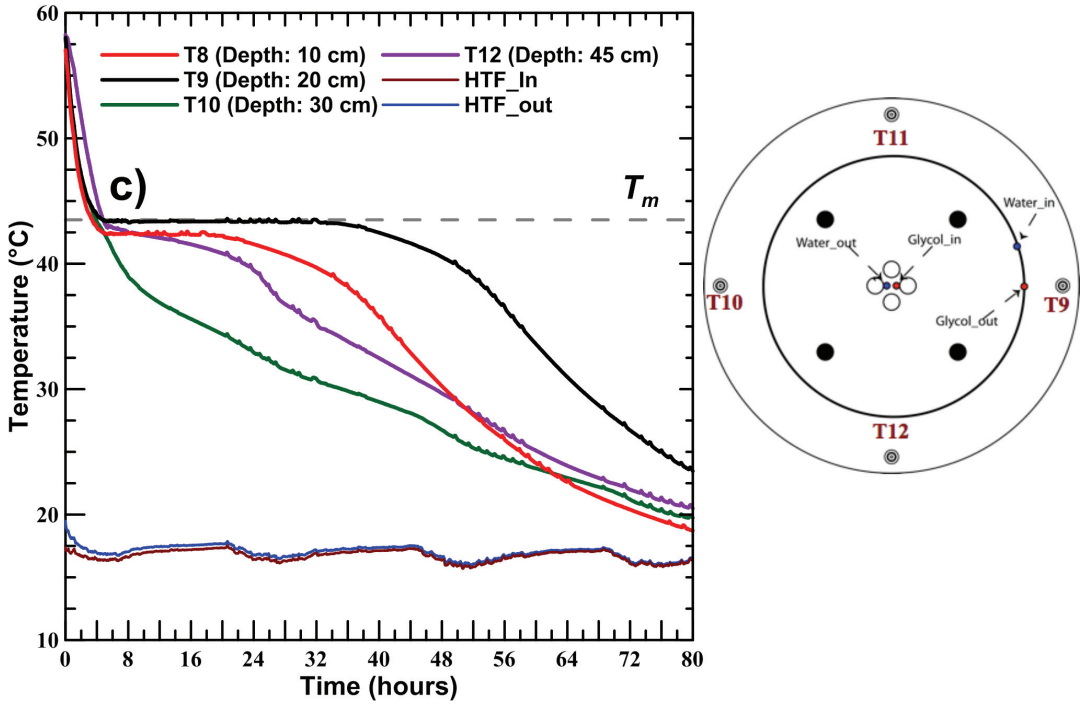

Figure 5.37 Temperature profiles as a function of time measured during discharging ($T_{C,in}$ = 16ºC, 2.5 L/min): c) Outer probes T9 to T12, continued

The power output shown in Fig. 5.38 shows the same trend observed in the previous experiment with a starting peak at 0.3 kW. The cumulative energy recovered is closely aligned with the theoretical storage capacity was 15.11 MJ as shown in Fig. 5.39. The uncertainty associated with the energy recovered was 99 %, ranging between 0 MJ to 30 MJ. The unreasonable uncertainty is due to the extremely low temperature difference between inlet and outlet with an average value of 0.25 ºC, which is smaller than the measurement uncertainty of the thermocouple. The absolute value of the power plot slope is higher for experiment 6 than experiment 7. Since both parameters were varied, it is difficult to draw conclusion on the parametric effects on discharging. However, in theory it is known that an increase of the flow rate should increase the heat transfer coefficient due to forced convection, which in effect decreases the thermal resistance between the water and the PCM. Therefore, if an increase in temperature alongside an increase with the HTF flow rate decreases the heat transfer rates therefore it is safe to deduce that the HTF inlet temperature has more of an effect on solidification than the

HTF flow rate. In addition, such findings are consistent with the findings reported in the literature as shown in section 2.4.2.

While the total discharge time was 80 hours, the energy recovered after 40 hours was 10.29 MJ, which constitutes 67 ± 1 % of the total amount of energy that will ultimately be recovered through the process. Table 5.7 shows a summary of the results including the range of the power output, the cumulative energy recovered and the discharge time.

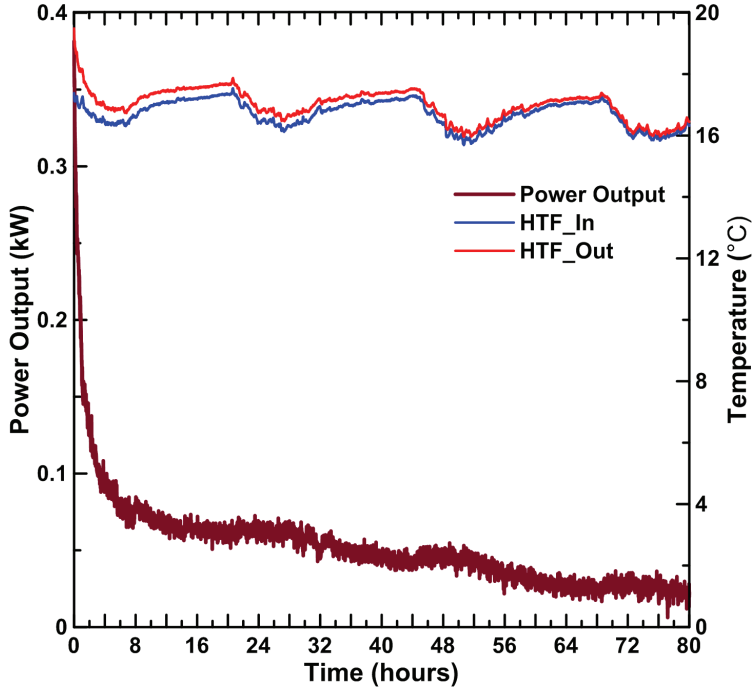

Figure 5.38 Power output as a function of time during discharging experiment ($T_{C,in}$ = 16 ºC, 2.5 L/min)

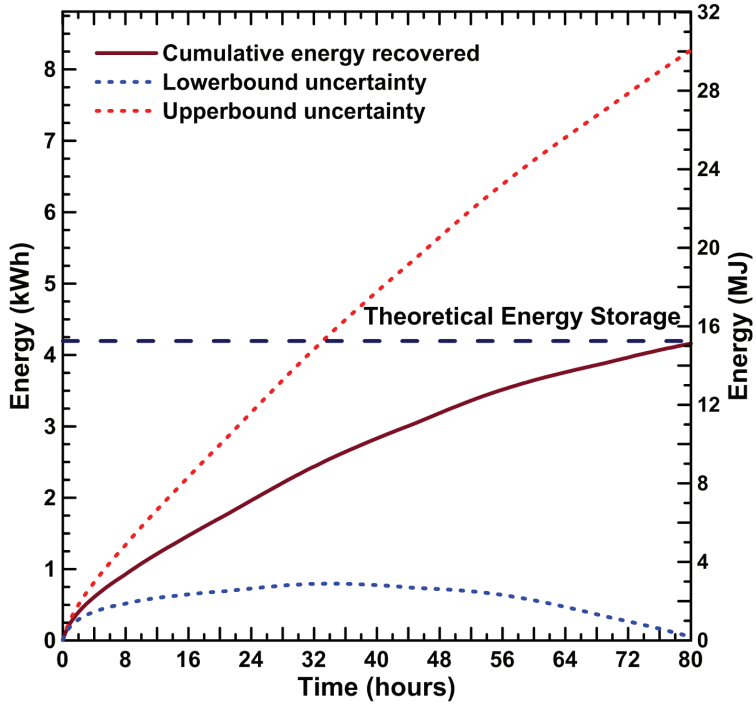

Figure 5.39 Cumulative energy recovered as a function of time during discharging experiment ($T_{C,in}$ = 9 ºC, 1.5 L/min)

Table 5.7 Summary of the result of the municipal discharge experiments

Experiment	Power output range (kW)	Cumulative Energy recovered (MJ)	Discharging time (Hours)
6	0.3-0.04	15.7 ± 56 %	59
7	0.3-0.02	15.11 ±99 %	80

5.4 SENSIBLE VERSUS LATENT STORAGE

In order to evaluate the limitations of the current LHESS with the coil heat exchanger, a comparative study was conducted between water-based storage and PCM-based storage in an identical tank with the same thermocouple locations. The value of such a

comparison provides a reference point for design and optimization of heat exchangers in LHESS. For example, the implementation of a LHESS into SDHW system requires the LHESS to be able to perform at least at the same quality of a conventional system. A coil heat exchanger was used in a comparative study between PCM and water storage, and illustrates the degree of design optimization required for a LHESS heat exchanger.

5.4.1 Real-Time Solar Water Charging

Two days with nearly identical solar conditions were chosen. The PCM charging was conducted on March 4th and was previously presented and discussed in section 5.2.3. The water charging was conducted on March 6th. Figure 5.40 shows the solar insolation in addition to the glycol inlet and outlet temperatures. The glycol inlet/outlet temperatures for PCM charging are shown in Fig. 5.25b). A comparison between the two glycol loops in both figures reveals that the inlet temperatures measured for the PCM system quickly reach higher values relatively to the water system. The inlet/outlet HTF temperature differential in the PCM system (Fig. 5.25b) was initially significantly less than what was observed in the water system as shown in Fig. 5.40b).

Both of these observations can be explained by the higher thermal resistance of the PCM, stemming from its low thermal conductivity, in the solid phase relatively to the liquid water, which results in less heat transfer from the HTF to the storage media at the beginning of the experiment. As the PCM melts, natural convection becomes the dominant mode of heat transfer as observed in sections 5.1 and 5.2. This increases heat transfer and therefore results in higher storage rates and faster removal of energy from the HTF. The effect is observed in the PCM glycol inlet and outlet temperature profiles seen in Fig. 5.25b), by comparing hour 1 and hour 3. For the water storage system, natural convection is the dominant mode of heat transfer throughout the process and the water tank is not subject to the initial charging lag observed in the PCM.

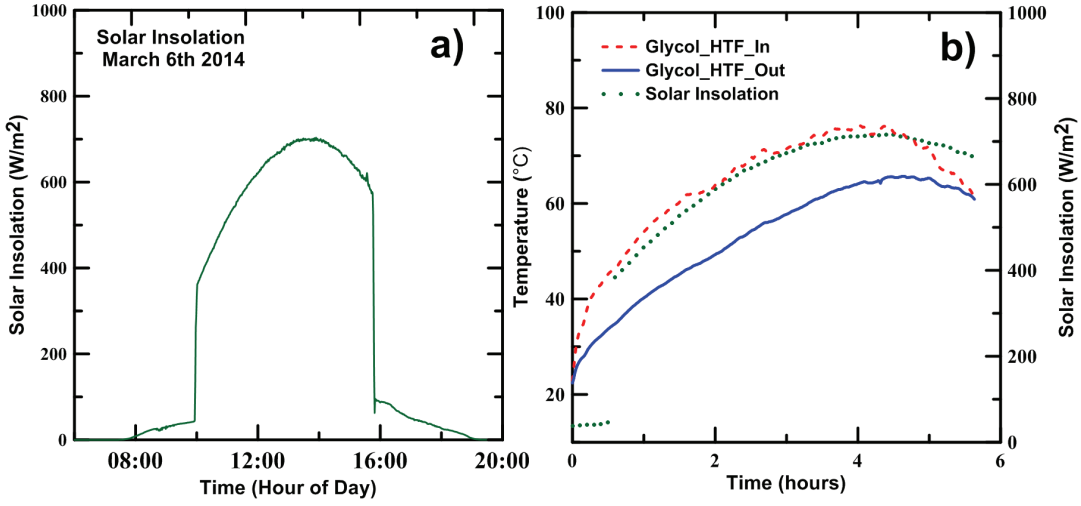

Figure 5.40 a) Solar insolation on March 6th 2014, b) Glycol inlet/outlet temperatures relatively to solar insolation

Figure 5.41 shows the temperature profiles of the 12 probes located inside the water tank during charging. It can be seen that water reaches a higher final temperature slightly above 60 °C and that the temperatures increases nearly linearly everywhere in the tank, with a small degree of stratification due to the natural convection cells. While in the PCM, as seen in Fig. 5.26, only 5 probes recorded temperatures higher than the melting point (43.5 ± 0.5°C), taking approximately 2 hours from the beginning of the experiment to reach the melting temperature.

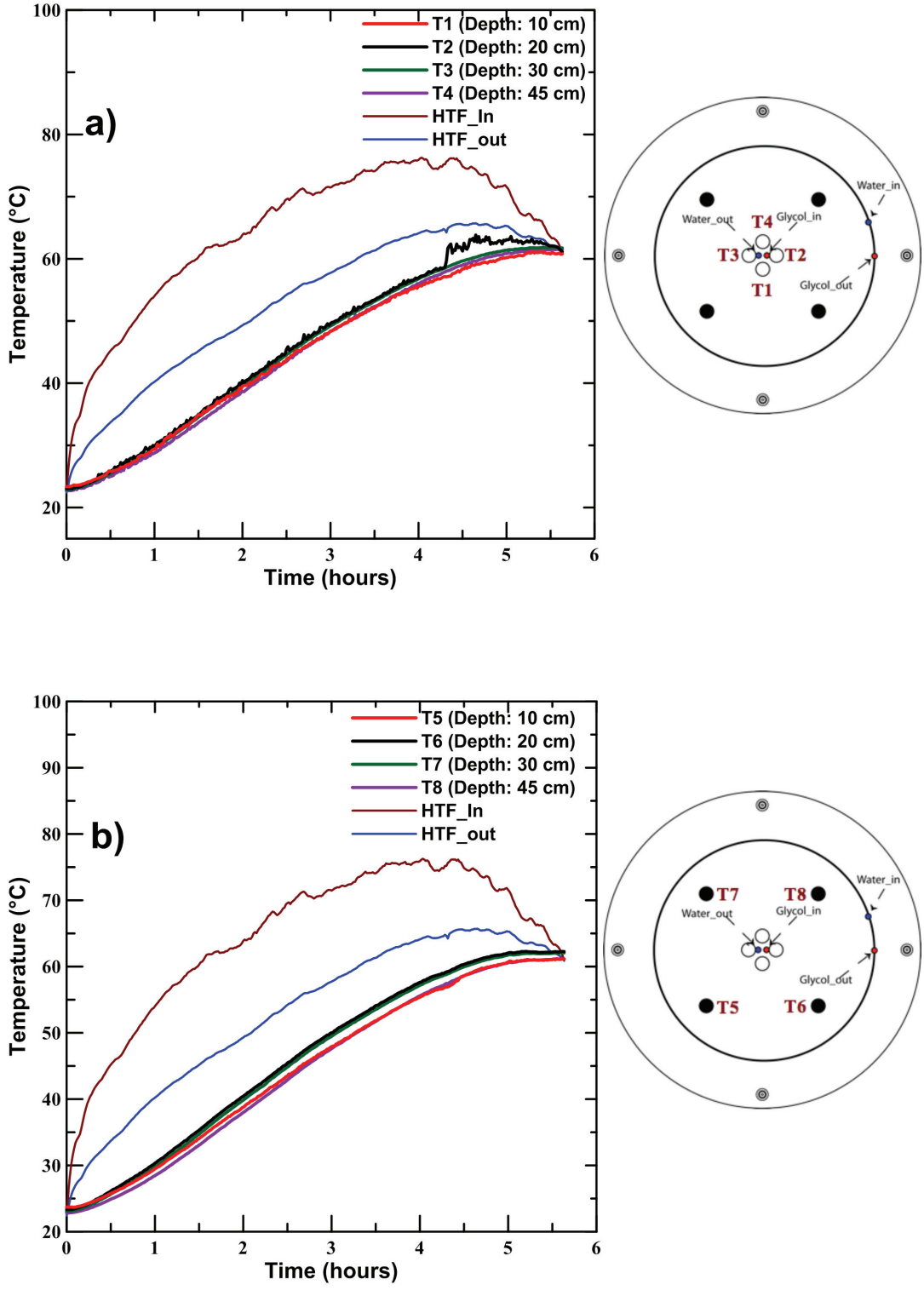

Figure 5.40 Temperature profiles as a function of time on March 6th 2014 for solar water charging: a) Inner probes T1 to T4 b) Middle probes T5 to T8

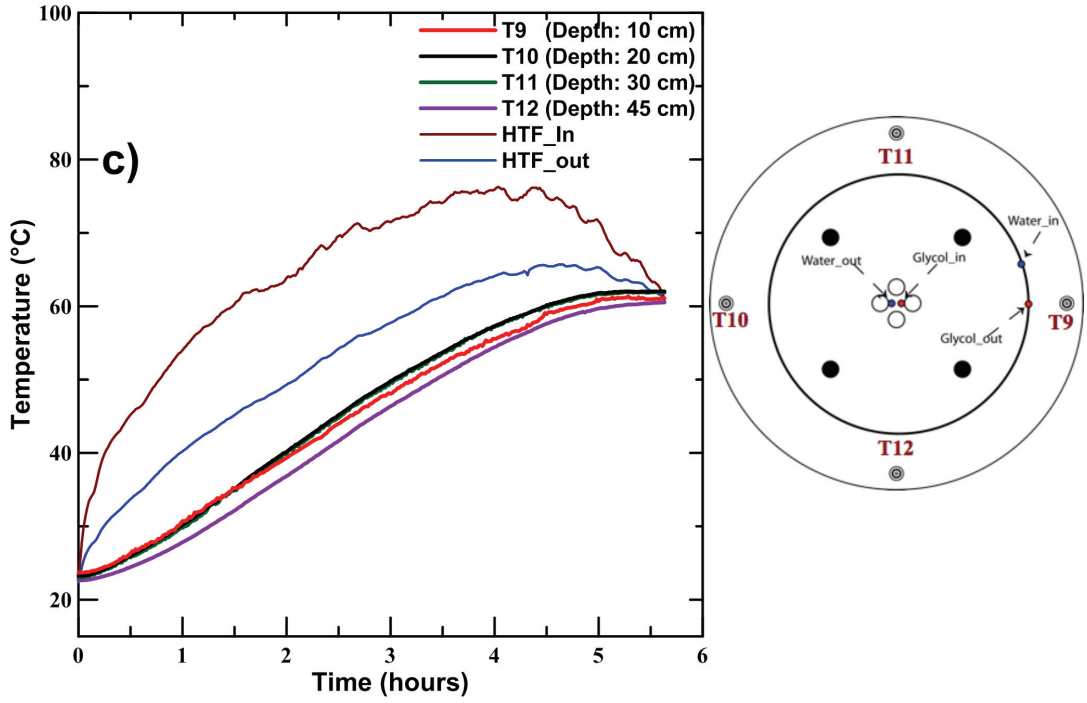

Figure 5.41 Temperature profiles as a function of time on March 6th 2014 for solar water charging: c) Outer probes T9 to T12, continued

The power input to the water tank over the charging period is shown in Fig. 5.42, the maximum power input to the water tank is 0.66 kW. While the maximum power input achieved by the PCM was 0.45 kW. In addition, the power input to the water tank was maintained for a longer period of time as can be observed in the comparison between Figs. 5.27 and 5.42. Figure 5.43 shows the cumulative energy stored with the cumulative uncertainty. The tank was able to store 9.7 MJ with an uncertainty of 12% during a 6-hour solar charge, nearing its maximum theoretical storage capacity. In comparison, the PCM in the LHESS stored 6.3 MJ, with 59% of its theoretical storage capacity remaining after a 6-hour solar charge. The LHESS is theoretically capable of storing a greater quantity of energy. However, due to the low heat transfer properties of the PCM, this was not achieved using a simple coil heat exchanger.

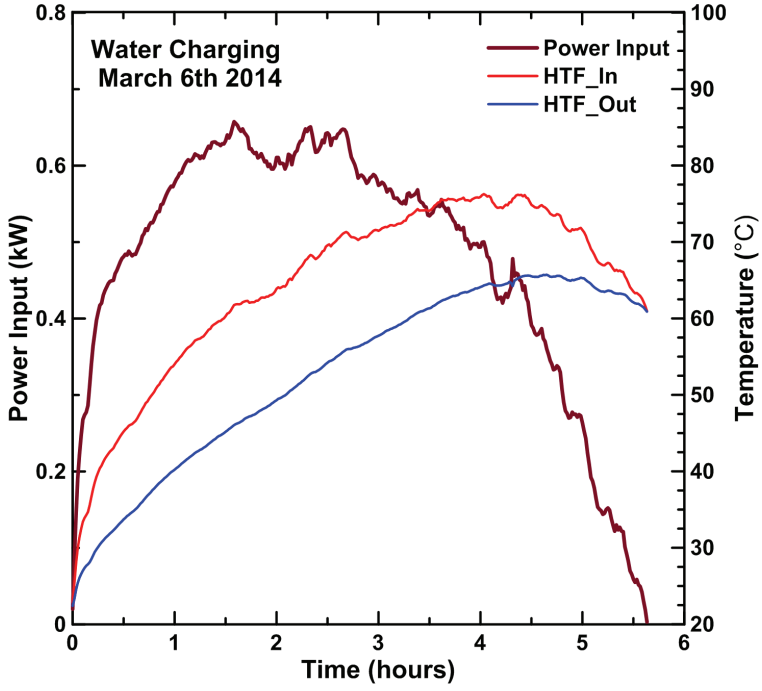

Figure 5.42 Power input and HTF inlet and outlet temperatures as a function of time during water charging on March 6^{h} 2014.

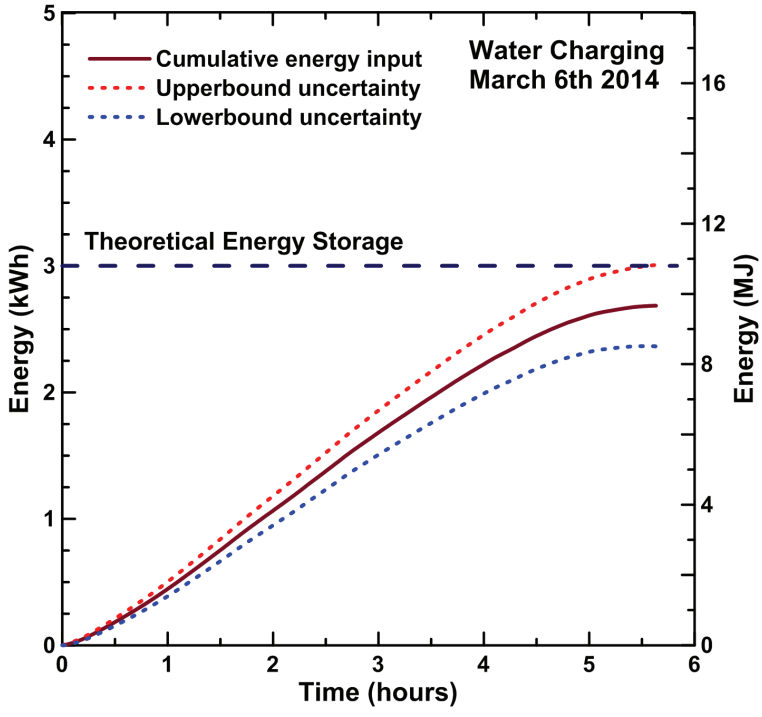

Figure 5.43 Cumulative energy stored as a function of time during water charging on March 6^{h} 2014.

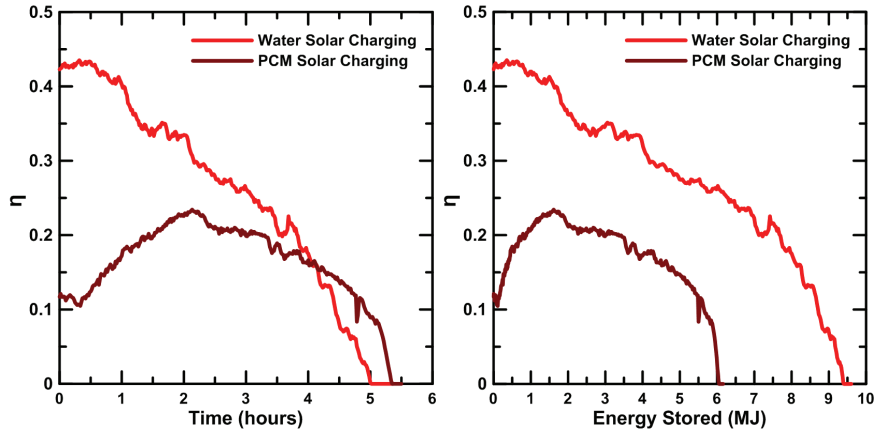

Figure 5.44 Solar collector efficiency as a function of time and energy stored during the solar charging of water and PCM tanks.

This indicates that not all of the available solar energy is being transferred to the LHESS. Figure 5.44 shows the solar collector efficiency calculated for both systems over the charging period. The solar collector efficiency ($\eta_{collector}$) is defined as the ratio of the rate of useful thermal energy leaving the collector, to the useable solar irradiance falling on the aperture area, as shown in Eq. (5.4):

$$\eta_{collector} = \frac{\dot{m}C_p\left(T_{glycol,in} - T_{glycol,out}\right)}{A_{collector} \times G} \tag{5.4}$$

The efficiency of the collector during the solar charging of the water tank shows a steady decreasing trend, ranging between 0.42 and zero. The efficiency of the collector during the solar charging of PCM shows a different trend, with an initial increase until a maximum value of approximately 0.25 is reached after 2 hours. This increase can be explained by the gradual increase of the HTF temperature difference during the initial charging period as seen in Fig. 5.25. After 4 hours, it can appear that the efficiency is higher for the PCM charging, however the efficiency for water charging is higher throughout the whole process when the efficiency is gauged relatively the energy stored. This is caused by the decrease in the HTF temperature difference for the water charging at the end of the process as the water tank temperature approaches the HTF temperature. This observation shows that the performance of the heat exchanger in the LHESS does

not only affect the system's ability to store the solar energy but also affects its ability to capture it.

It must be noted however, that test conditions for early-March in Canada offer short solar days and low ambient temperatures. The results demonstrate that LHESS should be improved through alternative heat exchanger designs that will increase the heat transfer rate to the PCM. The study of finned tubes and the possibility of implementing multiple coils in the tank are discussed in Chapter 6.

5.4.2 Municipal Discharge

In order to compare the discharging performance of the LHESS and water system, the discharging on a fully charged PCM tank shown in section 5.3 is used for comparison with the solar charged water tank. Municipal water was used for both experiments as the cooling HTF. The temperature profiles discussed earlier in section 5.3 show that the energy in the liquid PCM is quickly recovered, however the plateau around the solidification temperature releases the heat at a slow rate. Radial gradients were observed in the PCM tank, which indicates conduction dominated heat transfer during discharging. The water tank temperature profiles shown in Fig. 5.45 show only horizontal stratification. The HTF temperature difference between the inlet and outlet for the PCM was significantly smaller than that observed with the water tank. Figure 5.45 shows a large temperature difference, which results in useful pre-heated water. The PCM discharge shows a steady temperature difference for 60 hours. The integration of that energy over time is larger for the PCM, however the usefulness of energy is a major issue when it comes to systems that are demand dependent.

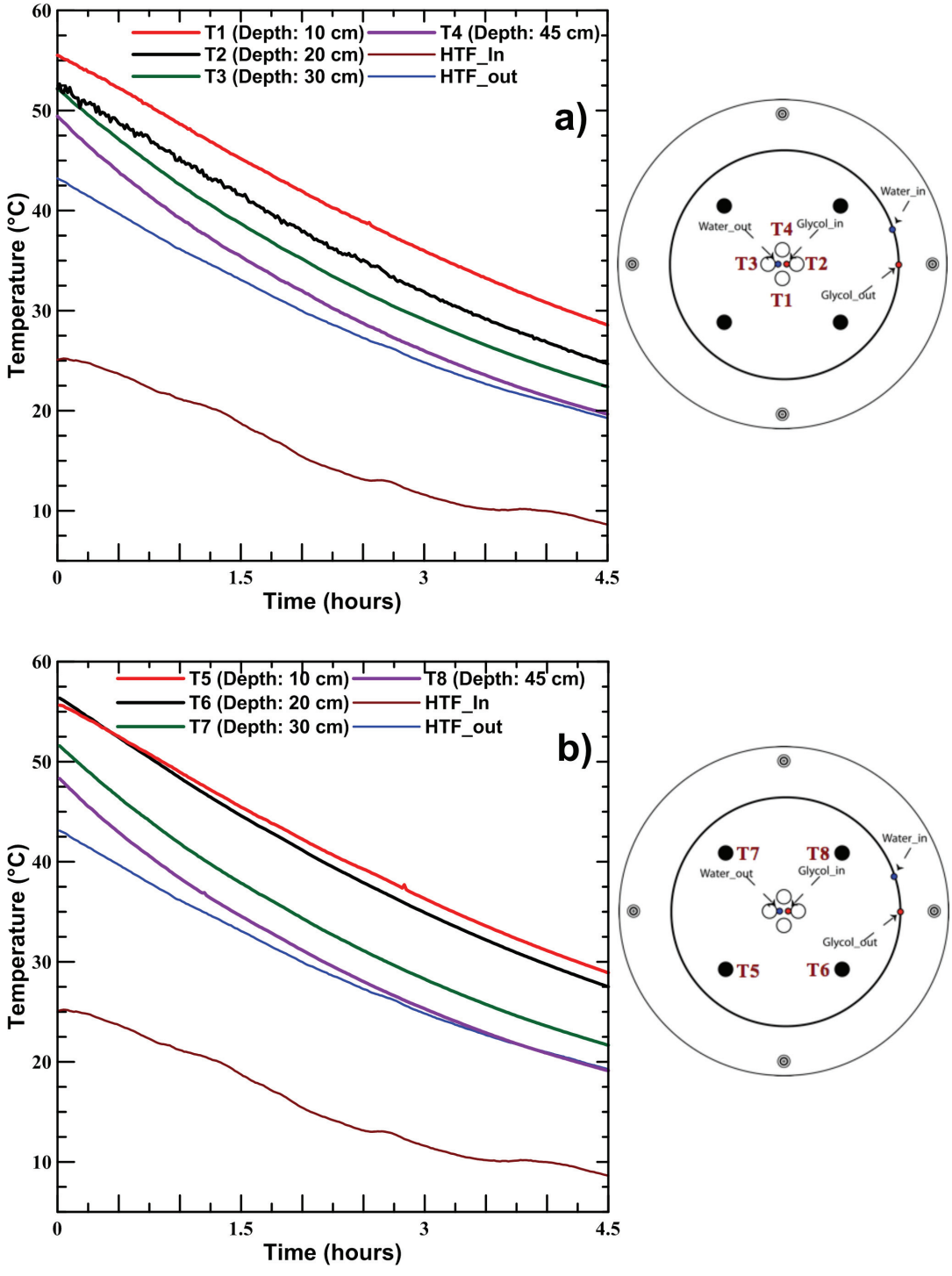

Figure 5.45 Temperature profiles as a function of time measured during discharging: a) Inner probes T1 to T4 b) Middle probes T5 to T8

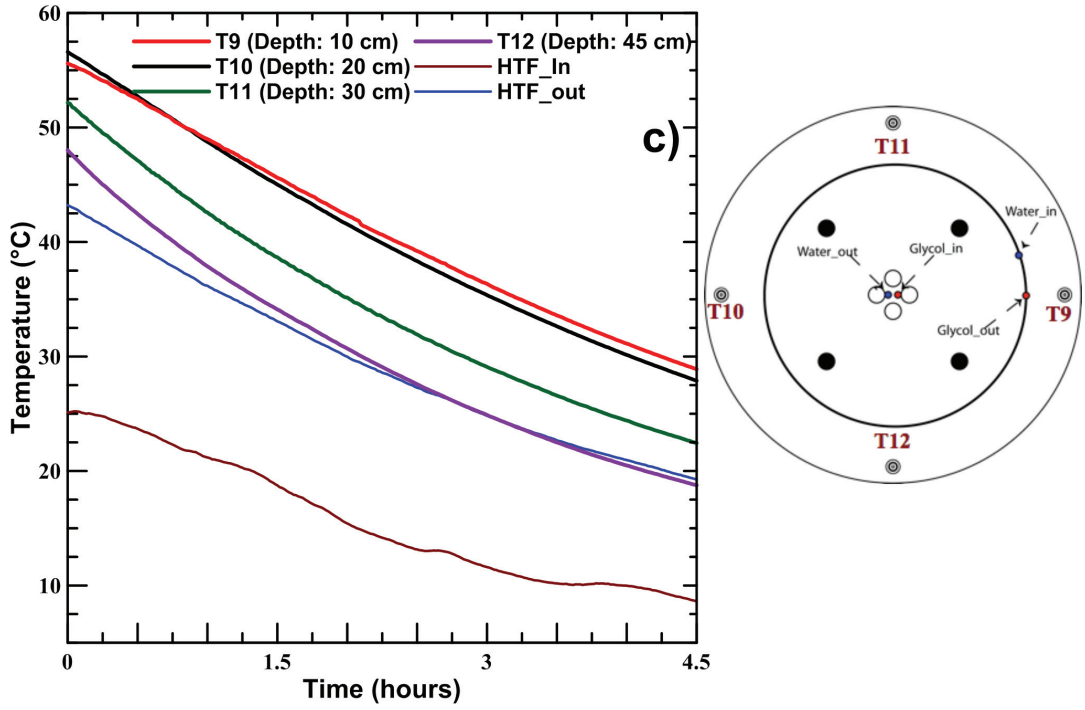

Figure 5.45 Temperature profiles as a function of time measured during discharging: c) Outer probes T9 to T12, continued

Power output as shown in Fig. 5.46 for the water discharge was around 6-8 times higher than that observed for the PCM. The peak power output was approximately 0.8 kW and decreases down to 0.42 kW. The cumulative energy recovered was closely aligned with the energy stored during the real-time solar charging experiment on March 6th. The energy recovered was 9.4 MJ with an uncertainty of 10% as shown in Fig.5.47. The low uncertainty is due to the high temperature difference observed throughout the process. The rate of energy transfer from the water tank was substantially faster than the PCM tank, requiring only 4.5 hours in the case of water for energy discharge, versus nearly 60 hours to release the energy from the PCM. However it should be noted that the initial cumulative energy in the PCM tank was 60% higher than in the water tank due to dodecanoic acid's high energy density from latent heat. Therefore, an improvement in heat exchanger design will allow for the exploitation of the additional heat storage capacity available in LHESS.

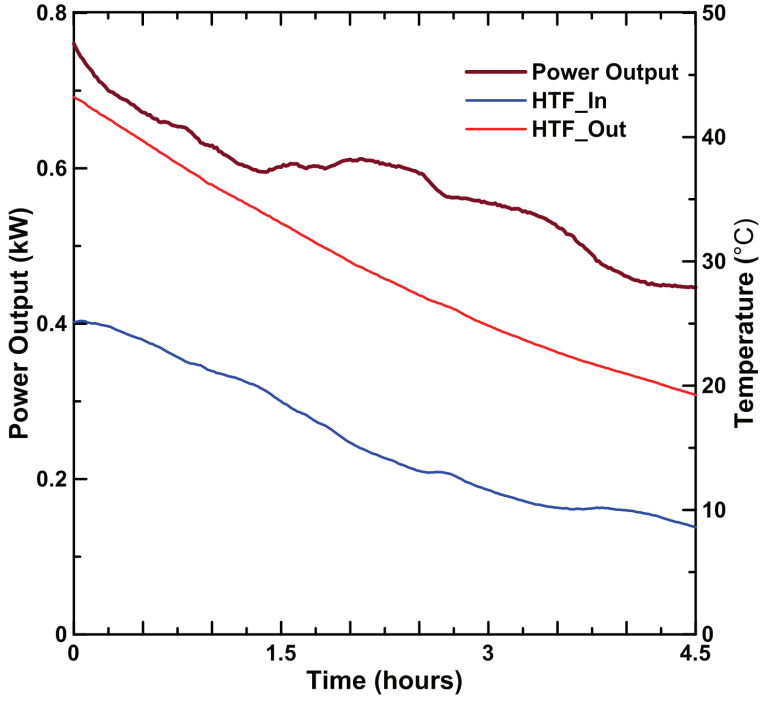

Figure 5.46 Power output and HTF inlet and outlet temperatures as a function of time during water discharging.

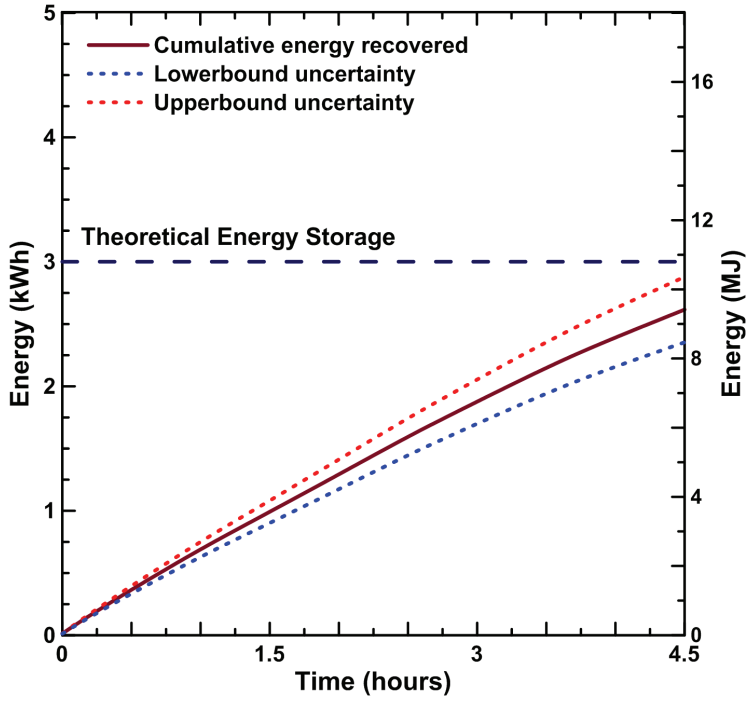

Figure 5.47 Cumulative energy recovered as a function of time during water discharging.

5.5 CONCLUSION

Chapter 5 showed the results of characterization experiments of Tank A under controlled experimental conditions. It was found that during the initial periods of charging conduction was the main mode of heat transfer, while natural convection played an important role once significant melting has occurred in the tank. The increase of the HTF inlet temperature showed to have a significant impact on increasing heat transfer rates during the charging process. The increase of the HTF flow rate showed improved heat transfer rates but not at the same degree of significance as the increase of the inlet temperature.

Results from real-time solar experiments were also shown for four solar days representing various seasonal and weather conditions. It was found that during shorter days with low available solar radiation, significant melting was not observed and the main mode of heat transfer remained conduction.

Two municipal discharge experiments under various conditions were conducted. It was shown that the time scale for discharge was much higher than charging. The main mode of heat transfer was conduction due to the heat exchanger having an ever-growing layer of solid surrounding it throughout the process.

Tank A was analyzed as a latent heat storage system with lauric acid and as a sensible heat storage system with water. Real-time solar results on a similar March day indicated that the water tank stored more energy over the course of the day while nearing its maximum storage capacity, while the PCM tank only stored 40% of its maximum storage capacity. The solar collector efficiency also showed to be affected by the performance of the heat exchanger in the storage tank, with higher efficiencies for the water tank. The discharge process for water was more than 10 times faster than that of PCM. This indicates the level of improvement required for PCM storage to compete with water storage.

CHAPTER 6 RESULTS AND DISCUSSION: TANK B

This chapter presents a comparison of the experimental results of charging and discharging of tank B using a coil heat exchanger versus a finned tubed heat exchanger. The results include temperature profiles, heat transfer rates (power input/output), cumulative energy stored/recovered with the uncertainty and heat fluxes. The performance of the coil heat exchanger for tank B is compared to the one from tank A in the context of the Fourier number analogy. The heat flux is used to compare the performance of the two coils that operate under the same parameters.

In order to compare the two coils, conditions were matched in order to separate the effect of the operating parameters from the performance. Charging was conducted under matching experimental conditions for experiment 1 performed on Tank A. Discharging was conducted using municipal water at comparable conditions as experiment 6 conducted on tank A.

The scale-up design method proposed in section 3.4.2 is validated using observations from experiments on tank A and tank B. The method is then described in more detail in terms of a perspective design using multiple coils.

Table 6.1 List of the experiments conducted for heat exchanger comparison

Experiment Number	Location in Thesis	Heat Exchanger
Charging experiments with HTF at 1.1 L/min and 60 °C		
8	Section 6.1	Helical Coil
9	Section 6.2	Finned Tubes
Discharging experiments with HTF at 1.5 L/min and 9 °C		
10	Section 6.3	Helical Coil
11	Section 6.4	Finned Tubes

6.1 CHARGING: COIL HEAT EXCHANGER

An experiment was conducted on Tank B using the coil heat exchanger designed using the method described in section 3.4.3. The purpose of the experiment was to compare the system's capacity to transfer heat to the PCM per unit area (*i.e.* heat flux) relatively to Tank A, and to another heat exchanger in Tank B (Finned tubes). The experimental conditions consisted of a HTF inlet temperature of 60 °C and flow rate of 1.1 L/min, which matched those used in experiment 1 conducted on Tank A.

Figure 6.1 shows the temperature profiles of the thirteen temperature probes located inside of Tank B during the charging process using the coil heat exchanger. An illustration of the tank is shown next to each figure with the location of the probes shown in the graph and the direction of the first turn of the coil. Figure 6.1a) shows the temperature profiles of the probes located in the center section of the tank. The HTF enters from the side through the coiled part and exits after passing through the straight copper tubing located at the center of the tank. The probe R1D2 showed a fast increase in temperature at the beginning of the experiment due to its location at the center near the straight copper tubing and at a lower depth than R1D1, which exposes it to a hotter HTF. However, as more PCM melted, the effects of buoyancy contributed to increasing the temperature of the top of the tank, which made R1D1 the first probe to show melting. Similarly, the effects of the onset of natural convection and its location closer to the inlet led to higher temperatures recorded by R2D1 in comparison to R2D2 which happened to be the last probe to show melting in the center section of the tank. Probes located at the same depth showed a uniform temperature profile after melting, with R1D1 and R2D1 showing uniform temperatures after 5 hours, and R21D2 and R2D2 after 10 hours.

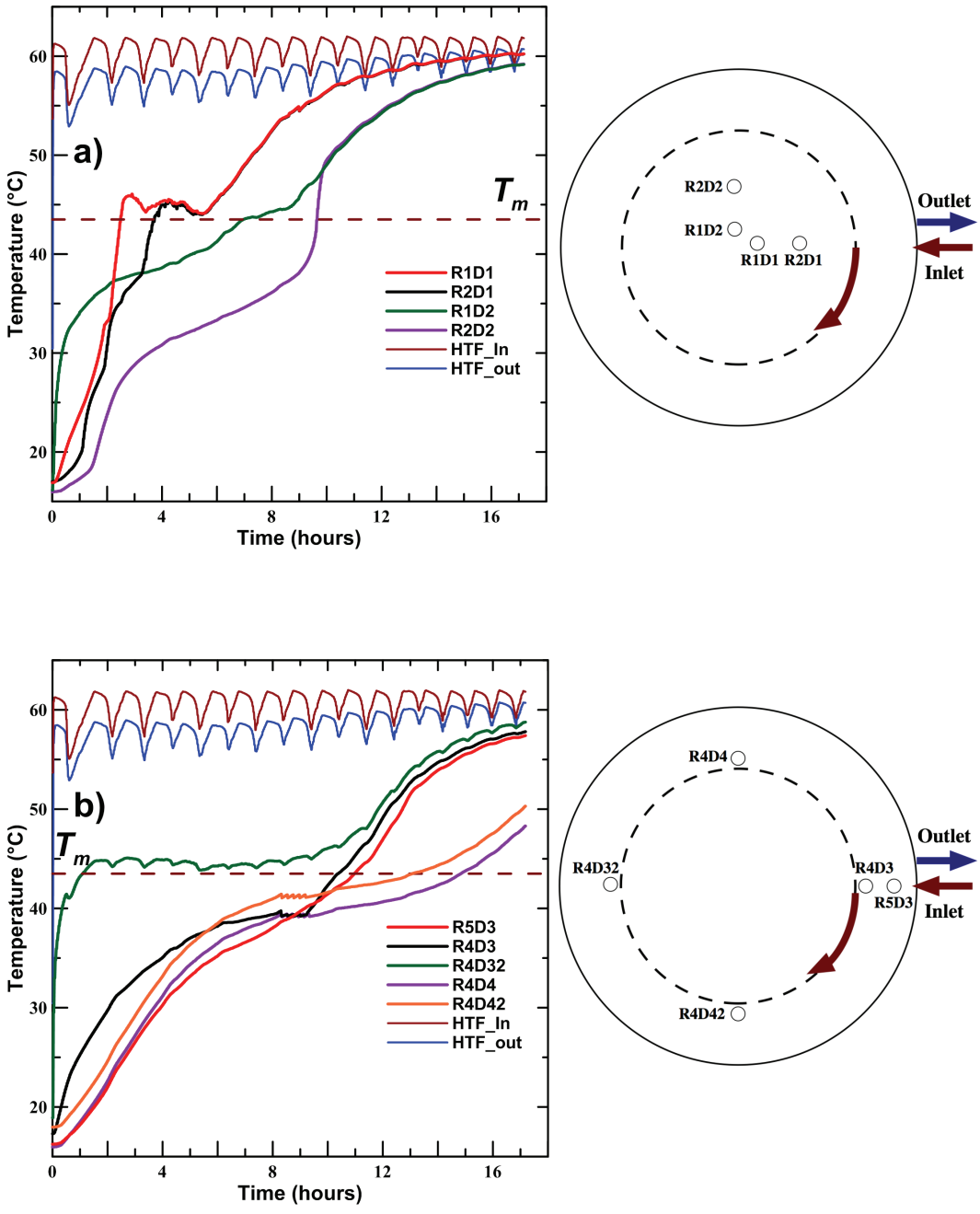

Figure 6.1 Temperature profiles as a function of time measured during charging for tank B using coil heat exchanger ($T_{H,in}$ = 60°, 1.1 L/min) : a) R1D1,R1D2,R2D1,R2D2, b)R5D3,R4D3,R4D32,R4D4,R4D42

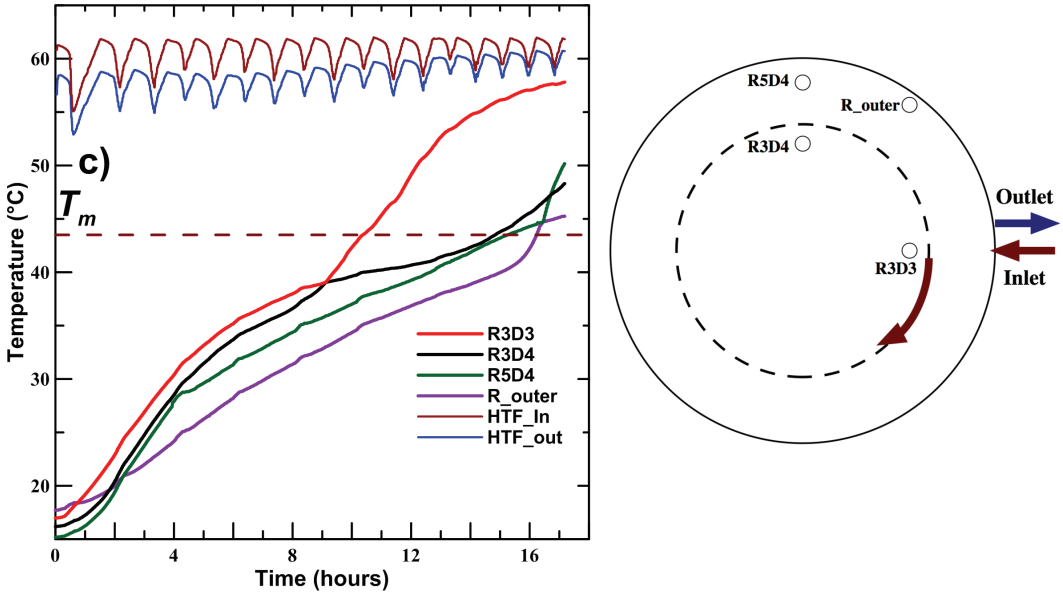

Figure 6.1 Temperature profiles as a function of time measured during charging for tank B using coil heat exchanger ($T_{H,in}$ = 60°, 1.1 L/min) : c) R3D3, R3D4,R5D4,R_{outer}, continued

Figure 6.1b) shows the temperature profiles of the probes located near the coil, in addition to one probe near the entrance. The first probe to show melting in the tank was R4D32. Since the probe R4D32 is next to the coil's 1st turn, it was therefore exposed to the highest HTF temperature. It was expected for it to show the fastest increase in temperature and melting. The temperature profiles of R4D4 and R4D42 were higher than R5D3 for the first 8 hours of the process. After approximately 10 hours, the temperature of R5D3 was higher that of R4D4 and R4D42 and showed melting prior to them. This is indicative of the important role natural convection played during the later stage of the melting process, which allowed R5D3 that is further away radially to the heat source, but higher in the tank, than R4D4 and R4D42 to undergo melting first. The probe R4D4 showed a lower temperature profile than its counterpart R4D42, due to its location at the opposite side of the tank. Therefore, it can be concluded that the proximity of the material to the HTF inlet has a significant effect.

Figure 6.1c) shows the temperature probes located near the coil (R3D3, R3D4), and on the outer edge of the tank (R5D4, R_{outer}). The first probes to show melting naturally

were the ones closer to the coil, with R3D3 showing higher temperature than R3D4 due to its location near the top. R5D4 showed a similar but higher profile that R_{outer} since it is closer radially to the coil and at a higher position. R_{outer} was the last probe to show melting due its location near the edge of the tank and at the very bottom.

Figure 6.2 shows the power input for the charging process as a function of time. The figure shows a similar trend that was observed in all the other charging processes discussed in section 5.1 for Tank A. The power input ranged between 0.15 and 0.05 kW. The power input was lower than that observed in experiment 1, which ranged between 0.2 and 0.1 kW. However, the heat flux for the coil in Tank B ranged between 3 and 1.5 kW/m^2, while that for Tank A ranged between 2.5 and 1.25 kW/m^2. Therefore, the performance of the coil during melting was comparable for both tanks.

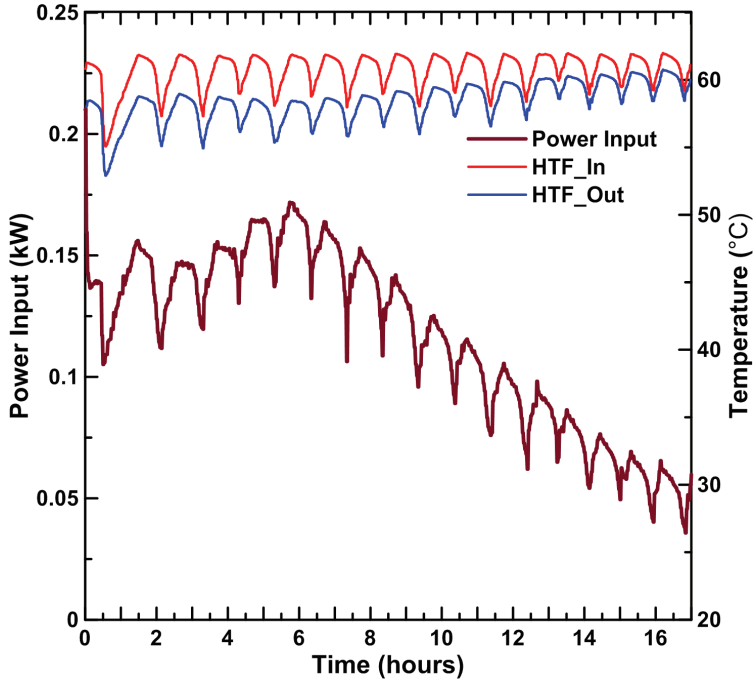

Figure 6.2 Power input as a function of time during charging experiment for Tank B ($T_{H,in}$ = 60°C, 1.1 L/min)

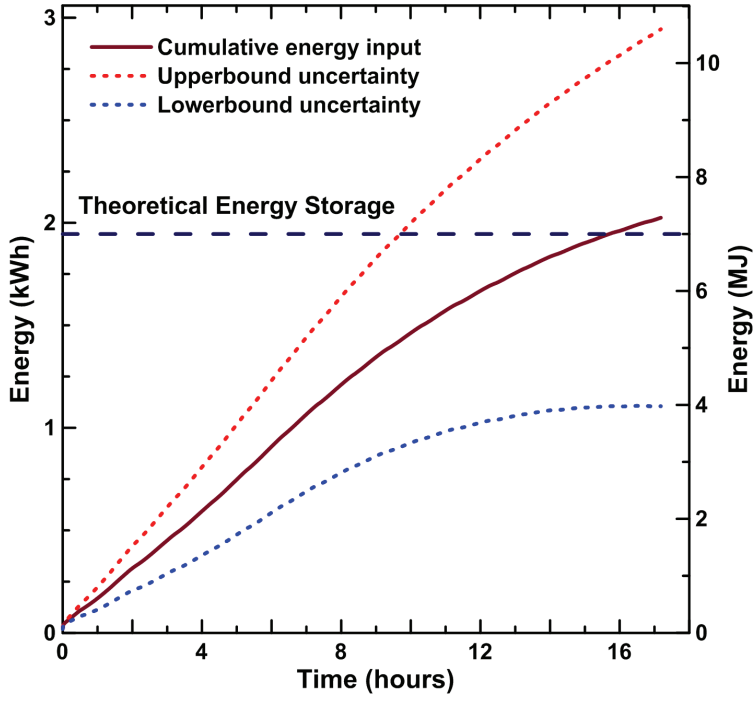

Figure 6.3 Cumulative energy stored as a function of time during charging experiment for Tank B ($T_{H,in}$ = 60°C, 1.1 L/min)

Figure 6.3 shows the cumulative energy stored during the charging process. The cumulative energy was 7.28 MJ and within close proximity to the theoretical energy storage, which is consistent with previous experiments. The uncertainty associated with the cumulative stored energy was 45%. In comparison, the uncertainty for experiment 1 conducted on Tank A was 13%. This can be explained by the difference in the temperature difference between the HTF inlet and outlet temperatures in both experiments due to the lower residence time associated with the coil in Tank B.

6.2 CHARGING: FINNED TUBES HEAT EXCHANGER

An experiment was conducted using the finned tubes heat exchanger described in section 4.3.3. The purpose of the experiment was to compare the performance of the finned tubes to the coil heat exchanger during charging. The experimental conditions consisted

of a HTF inlet temperature of 60 °C and flow rate of 1.1 L/min, which matched those used in experiment 8 that was conducted using the coil heat exchanger.

Figure 6.4 shows the temperature profiles of the 15 temperature probes (T1-T15) as described in section 4.3.4, with the top probes shown in green, middle ones in red, and bottom ones in blue. The first probe to show melting, T2 (1 in. from the center at a depth of 8 in.) due to its location near the fin closer to the inlet. However as the PCM starts melting, T1 as shown in Fig. 6.4a) (1 in. from the center at a depth of 4 in., but closer to the fin on the outlet side) achieves higher temperatures than T2, which is indicative of the onset of natural convection in the process. In addition, it was observed that the probes closest to the surface (T1, T4, T7, T10 and T13) exceeded the PCM melting temperature and achieved a uniform temperature after 4 hours. The temperature probe T19 shown in Fig. 6.4e) was observed to be the last probe to reach the melting temperature, which was due to the probe being at the edge and bottom of the tank, in addition to its exposure to the fins where the HTF has a lower temperature since it was closest to the exit.

Probes on opposite sides of the tank were compared in order to study the effect of their position relatively to the inlet/outlet of the HTF. The probes closest to the surface (T13 versus T10, and T4 versus T17) showed insignificant variations in their profiles relatively to the profiles to their counterpart since natural convection in the system brings the warmer liquid PCM to the top of the tank resulting in nearly uniform temperature. The probes located at a lower depth showed to be affected by their position relatively to the inlet/outlet of the HTF. T14 and T15 (depth 4 in. and 8 in.) located closest to the inlet of the HTF showed to record faster melting times in comparison to the probes on the opposite side (T11 and T12). Similarly, T5 and T6 showed higher temperatures in comparison to T8 and T9. Therefore it is evident that probes that are in the mid and bottom section of the tank are highly affected by their position relatively to the HTF inlet/outlet since conduction plays a more important role with the PCM being solid for a longer period of time at those depths.

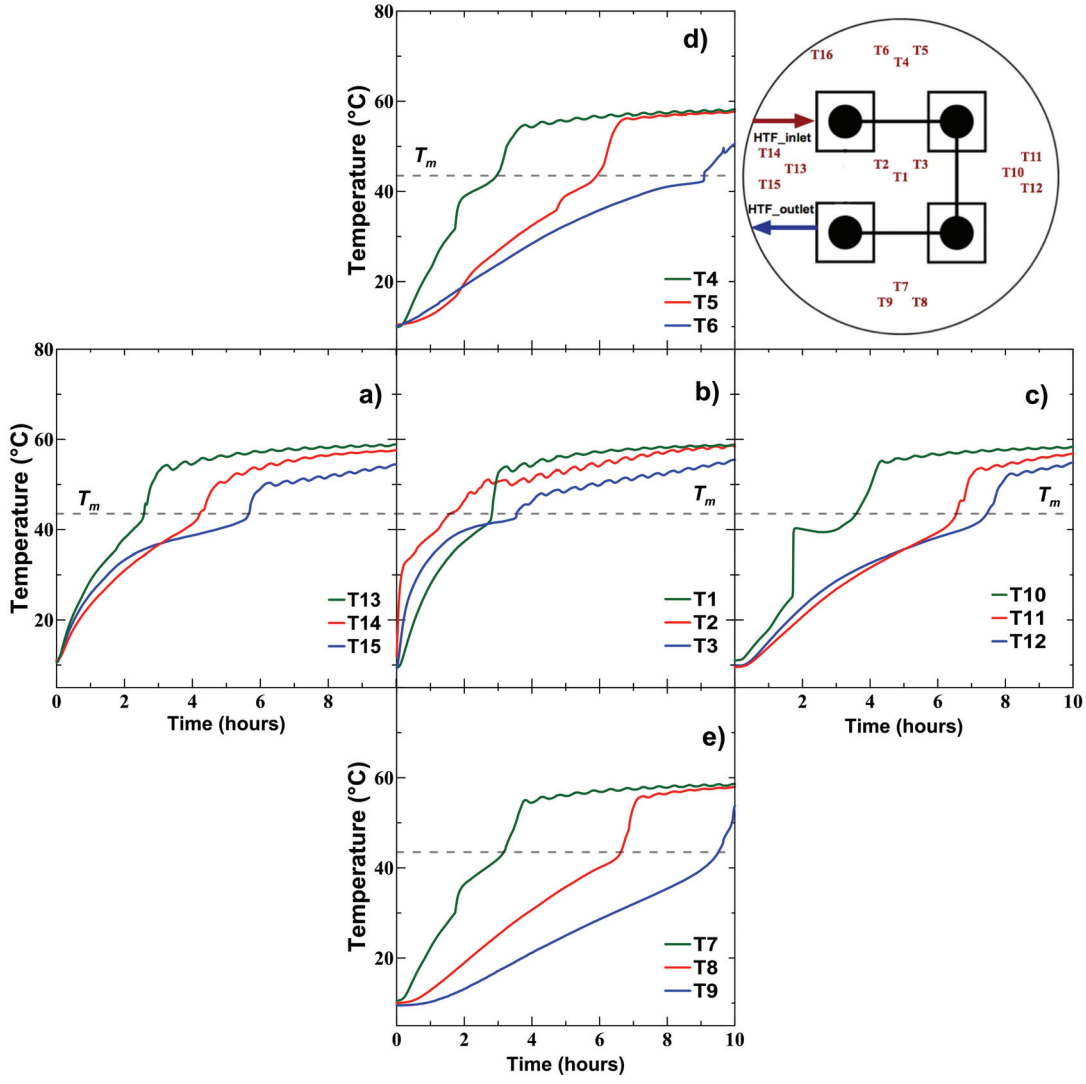

Figure 6.4 Temperature profiles as a function of time measured during charging for tank B using finned tubes heat exchanger ($T_{H,in}$ = 60°, 1.1 L/min) : a) T13 to T15 b) T1 to T3, c) T10 to T12, d) T4 to T6, e) T7 to T9

Vertical gradients were observed in the tank after an initial period of melting, which reinforced the major role of natural convection during the charging process. For example, Fig. 6.4c) shows probes T10, T11 and T12 having a uniform temperature initially (first 30 minutes) before enough liquid PCM is present leading to the onset of natural convection.

Figure 6.5 shows the power input for the charging process as a function of time. The figure shows a similar trend that was observed in all the other charging processes discussed in section 5.1 for Tank A and in section 6.1 for the coil heat exchanger. The power input ranged between 0.3 and 0.1 kW. The heat flux ranged between 1 to 0.3 kW/m^2. The power input was more than double than that observed in experiment 8, which ranged between 0.1 and 0.05 kW. This resulted in a significant decrease in charging time from 17 to 10 hours.

Figure 6.6 shows the cumulative energy stored during charging. The cumulative energy stored was 7.28 MJ with an uncertainty of 37.5%. However, as mentioned in previous sections, the uncertainty is caused by the small temperature difference between the HTF inlet and outlet temperature, and the proximity of the measured stored energy with the theoretical storage capacity gives greater confidence in the results despite having a high uncertainty.

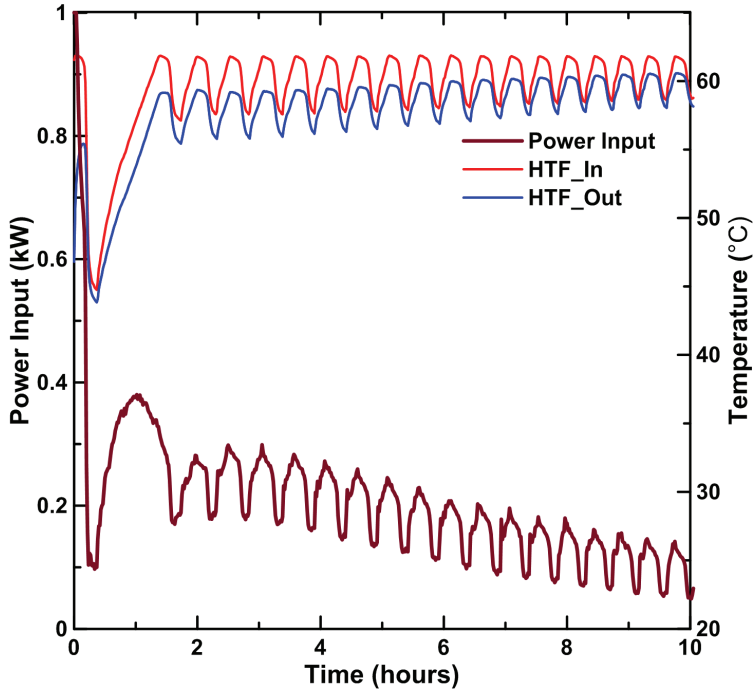

Figure 6.5 Power input as a function of time during charging experiment using finned tubes ($T_{H,in}$ = 60°C, 1.1 L/min)

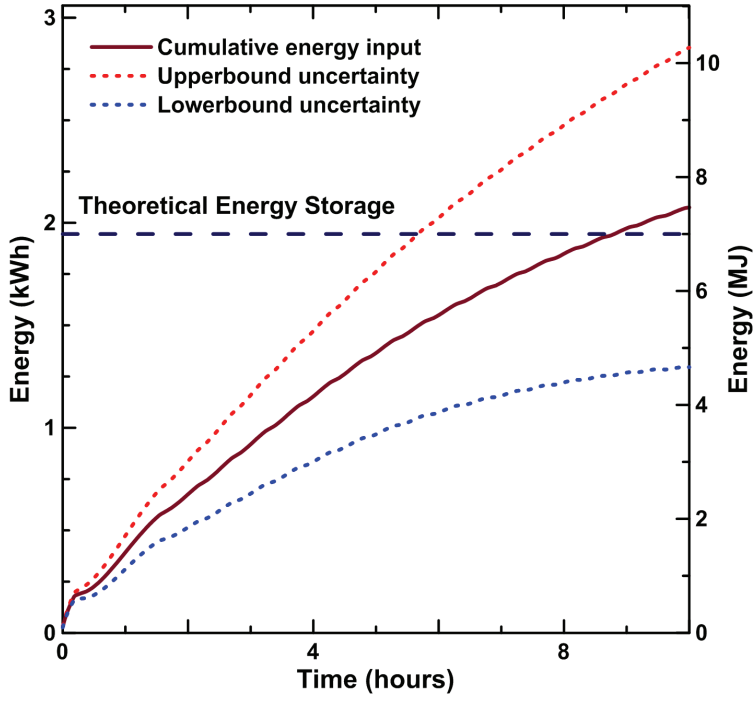

Figure 6.6 Cumulative energy stored during charging experiment using finned tubes ($T_{H,in}$ = 60°C, 1.1 L/min)

Table 6.2 shows a summary of the charging experiments results for the coil and finned tubes heat exchangers. The summary includes the power input range, the cumulative energy stored and the charging time.

Table 6.2 Summary of the charging experiments results using coil and finned tubes

Experiment	Power input range (kW)	Cumulative Energy stored (MJ)	Charging time (Hours)
8	0.15-0.05	7.28 ± 45 %	17
9	0.25-0.1	7.46 ± 37.5 %	10

6.3 DISCHARGING: COIL HEAT EXCHANGER

A discharge experiments with comparable experimental conditions as experiment 6 in section 5.3 was conducted using the coil heat exchanger for Tank B. The purpose of the experiment was to compare the heat transfer rates and heat flux of the process. The results from the experiments will be discussed and analyzed in section 6.5 in order to validate the Fourier number analogy method.

Figure 6.7 shows the temperature profiles of all 13 probes located in the tank during discharging for experiment 10. Figure 6.7a) shows the temperature profiles of the probes that are close to the center at two various radii and depths. The temperature profile of R1D2 shows a swift decrease in temperature due to its location next to straight copper section and at a lower depth than R1D1 which makes it exposed to a lower HTF fluid temperature as the HTF goes up the copper section in order to leave the tank.

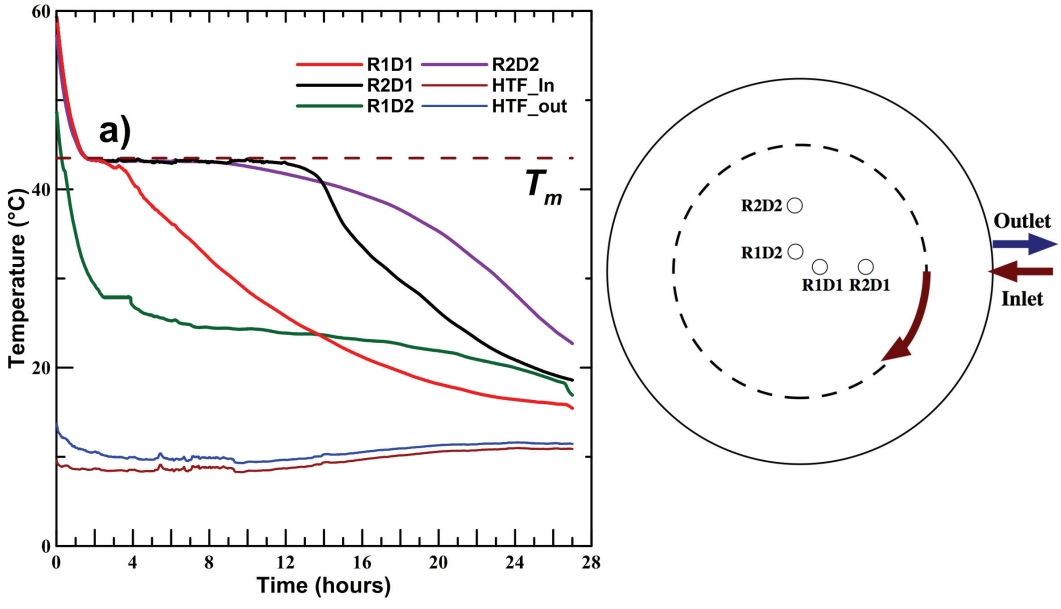

Figure 6.7 Temperature profiles as a function of time measured during discharging for tank B using coil heat exchanger ($T_{H,in}$ = 9°C, 1.1 L/min) : a) R1D1,R1D2,R2D1,R2D2,

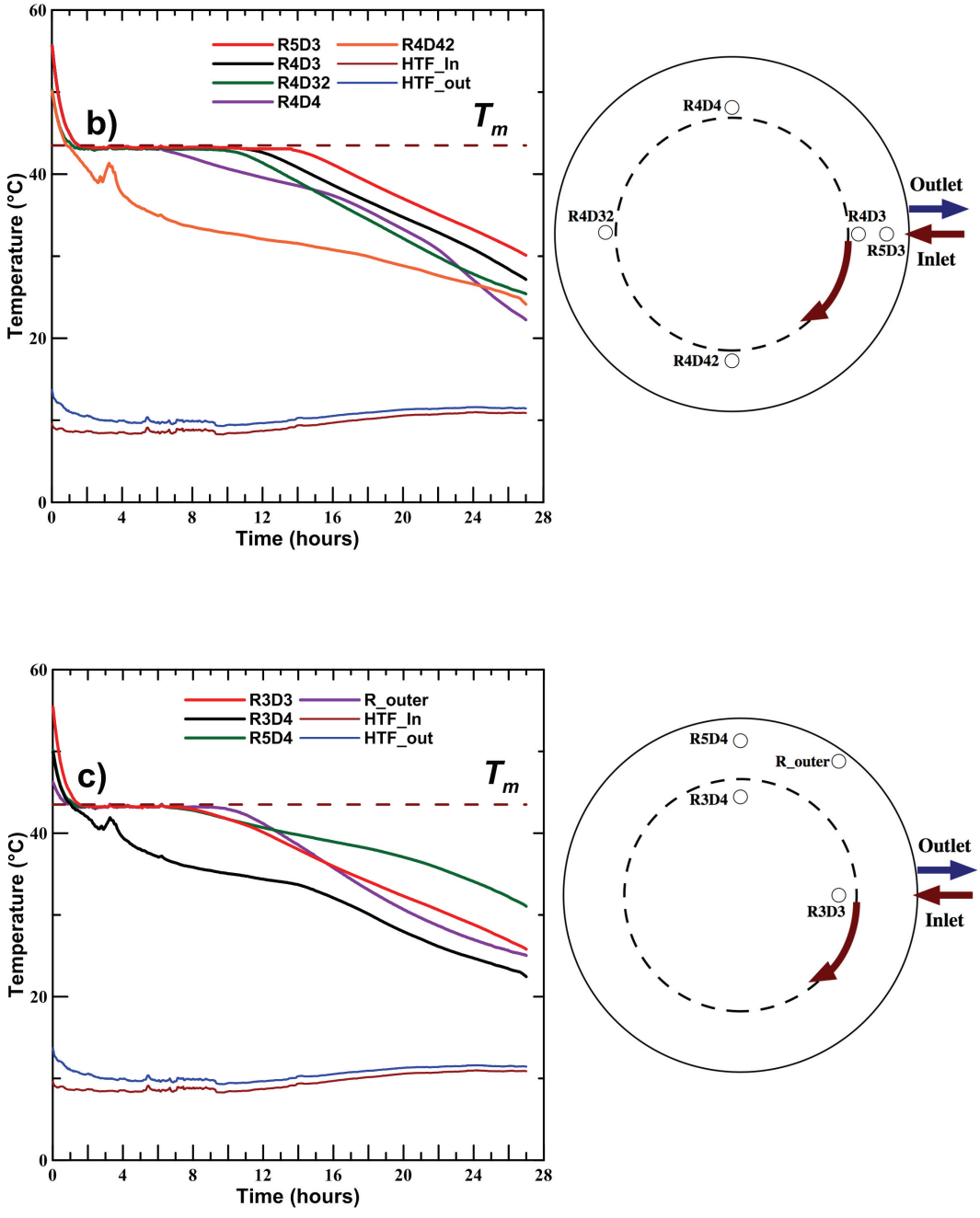

Figure 6.7 Temperature profiles as a function of time measured during discharging for tank B using coil heat exchanger ($T_{H,in}$ = 9°C, 1.1 L/min):
b) R5D3,R4D3,R4D32,R4D4,R4D42, c) R3D3, R3D4,R5D4,R_{outer}, continued

The temperature profiles for R2D1 and R2D2 are comparable, however R2D2 shows solidification 4 hours earlier. This can be explained by the probe's location at a lower depth, which makes it closer to the colder HTF coming up the straight copper section, the probes at a lower depth experience marginally lower temperatures, which may indicate the role of natural convection in the middle section of the tank since this effect is not observed in other sections of the tank.

Figure 6.7b) shows the temperature profiles of the probes located near the coil and entrance of the tank. It is observed that R4D42 is the first probe to undergo solidification, which is similar to the reason given for melting in section 6.1. The rest of the probes all show a similar profile with certain probes showing temperatures decreasing below the plateau at different times. It was observed that these probes at a lower depth and probes closer to the side of the inlet showed faster solidification times. For instance R4D42 showed faster solidification time than R4D4, which showed faster solidification times than R4D3, R4D32 and R5D3.

Figure 6.7c) showed the temperature profiles of the outer probes and probes located near the coil. It was observed the probe near the coil at lower depth (R3D4) experienced solidification faster than that at a higher depth (R3D3). The outer probe R_{outer} showed solidification at a similar time as R3D3, while R5D4 was the last probe to undergo solidification due its radial position and slightly higher depth than R_{outer}.

Figure 6.8 shows the power output as a function of time, along with the HTF inlet and outlet temperatures. The power output shows a decreasing trend with time, which can be explained by the ever-increasing amount of solid PCM forming around the heat exchanger surface with time. The maximum power output starts at 0.3 kW and drops asymptotically to 0.04 kW. The observed power output range is the same power output observed in experiment 6. However the heat flux is much higher for experiment 10, ranging between 6 and 0.8 kW/m^2 in comparison to 3.75 and 0.5 kW/m^2. The total discharge time was observed to be 27 hours in comparison to 60 hours for tank A. This is further discussed in section 6.5 in relation with the effect of the characteristic length.

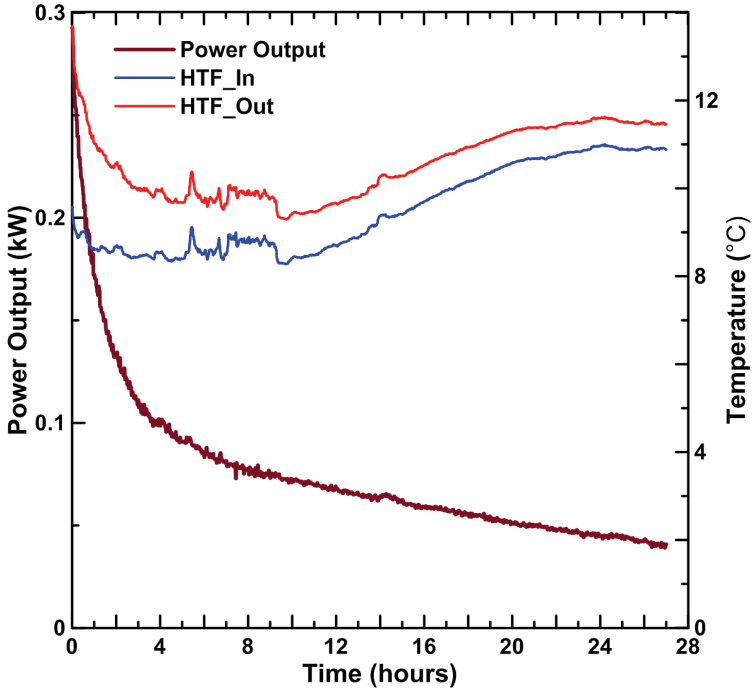

Figure 6.8 Power output as a function of time during discharging experiment for Tank B ($T_{H,in}$ = 9°C, 1.5 L/min)

Figure 6.9 shows the amount of energy recovered over time. The amount recovered is closely aligned with the theoretical storage capacity, which was approximately 7.29 MJ. The uncertainty associated with the energy recovered was 71%. It is seen in Fig. 6.8, the temperature differences between the HTF inlet and outlet are especially low, and given the measurement uncertainty on the thermocouples the accumulated uncertainty is going to be unreasonably high. However, the proximity of the total recovery to theoretical storage capacity increases the confidence in the results.

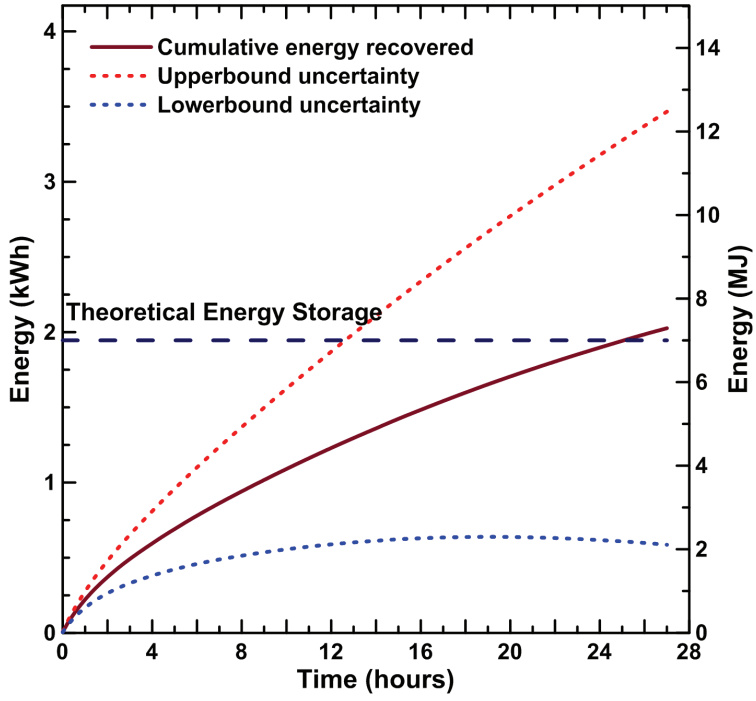

Figure 6.9 Cumulative energy stored as a function of time during discharging experiment for Tank B ($T_{H,in}$ = 9 °C, 1.5 L/min)

6.4 DISCHARGING: FINNED TUBES HEAT EXCHANGER

An experiment was conducted using the finned tubes heat exchanger described in section 4.3.3. The purpose of the experiment was to compare the performance of the finned tubes to the coil heat exchanger during discharge. The experimental conditions consisted of a HTF inlet temperature of 9 °C and flow rate of 1.5 L/min, which matched those used in experiment 10 that was conducted using the coil heat exchanger.

Figure 6.10 shows the temperature profiles of the 15 temperature probes (T1-T15) as described in section 4.3.4, with the top probes shown in green, middle ones in red, and bottom ones in blue. The first probes to show solidification were T2 and T3, which is due to their position close to the fins nearest to the HTF inlet. This indicates that the temperature drop across the first finned tube and the second is not significant since both probes showed highly similar profiles. Shortly after, the probe T13 showed a similar profile. The time lag is caused by the small difference in radial distance from the fins between T13 and the central probes (T2, T3). In general, it can be observed that the

probes located closer to the fins surface (T2, T3, T4, T7, T10 and T13) were the first to show solidification in the tank. The solidification plateau was exhibited for all probes except the ones located near the inlet as it can be seen in Figs. 6.10a) and 6.10b). The probes observed in Figs. 6.10a), 6.10b) and 6.10c) showed uniform temperatures at the end of the process. While probes observed in Figs. 6.10d) and 6.10e) showed radial gradients. This observation indicates the conduction dominant process with the sides of the tank taking more time to reach full solidification.

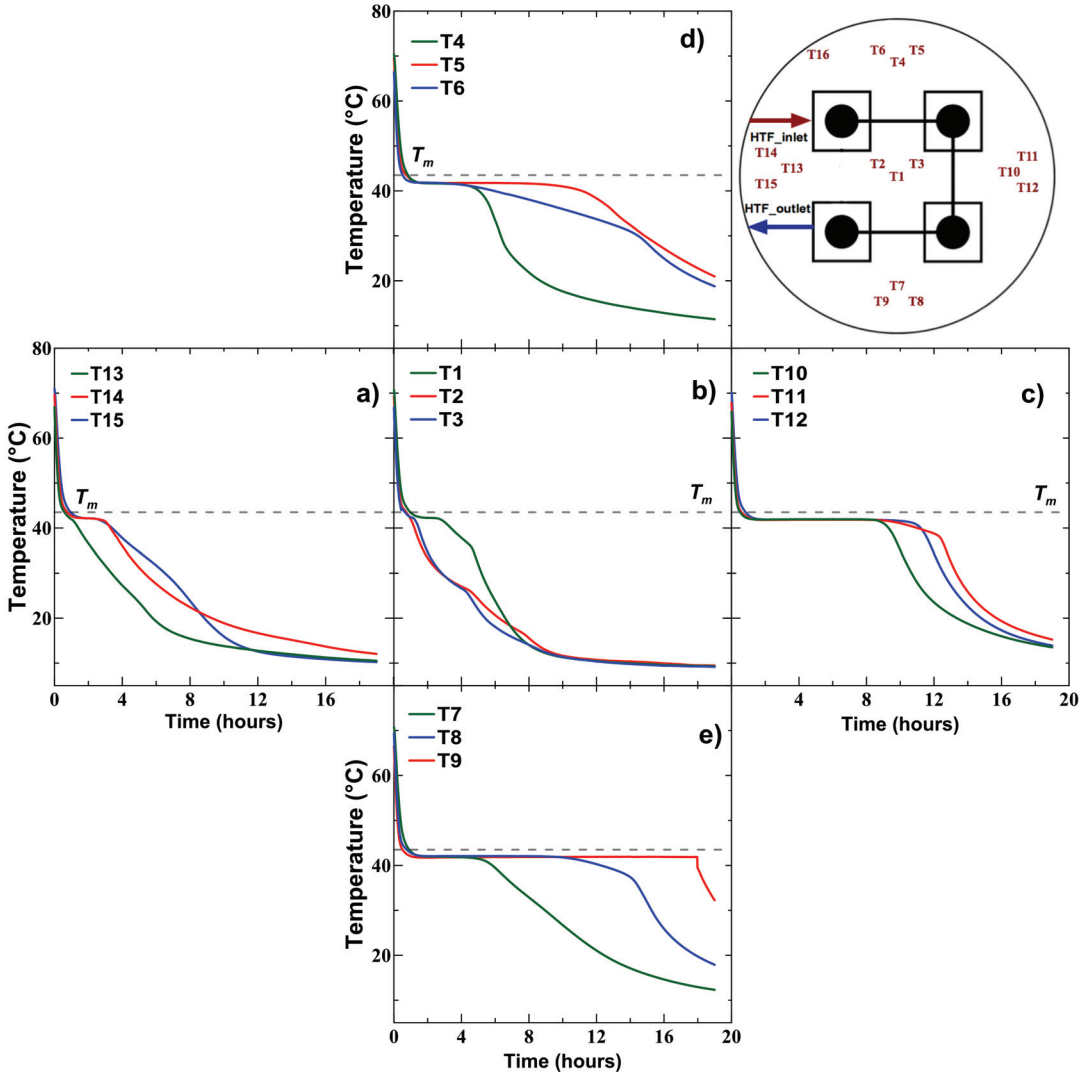

Figure 6.10 Temperature profiles as a function of time measured during discharging for tank B using finned tubes heat exchanger ($T_{H,in}$ = 9º, 1.1 L/min) : a) T13 to T15 b) T1 to T3, c) T10 to T12, d) T4 to T6, e) T7 to T9

Figure 6.11 shows the power output as a function of time, along with the HTF inlet and outlet temperatures. The power output follows a similar trend to previous discharging processes discussed in sections 5.3, 5.4.2 and 6.3. The maximum power output starts at 1.6 kW and shows a quick drop after 1 hour to 0.2 kW and then drops asymptotically to 0. The heat flux ranged between 5.3 and 0.6 kW/m^2. The observed range power output is higher than that observed for experiment 10, which starts with 0.3 kW and drop to 0.1 kW after 1 hour. The total discharge time was observed to be 19 hours in comparison to 27 hours for coil heat exchanger. This is explained by the increase of heat transfer area, which increased heat transfer rates.

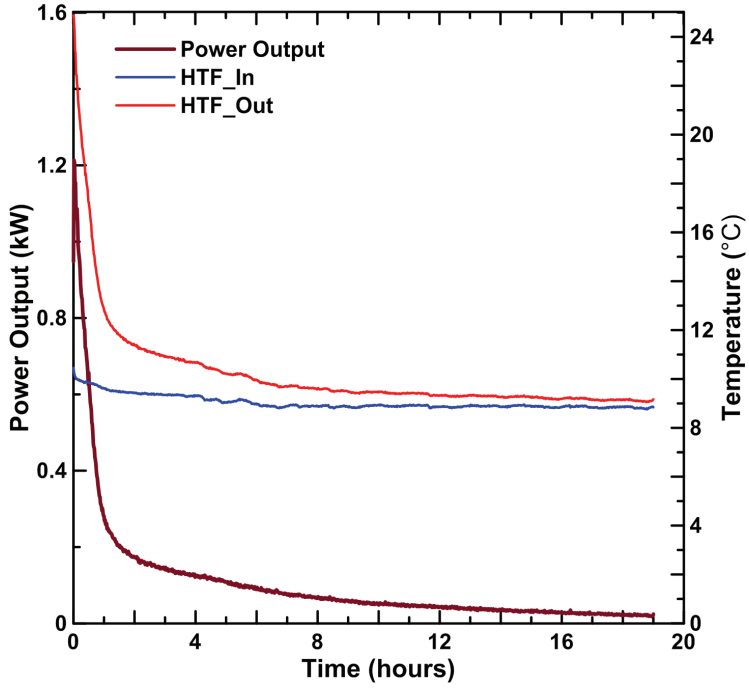

Figure 6.11 Power input as a function of time during discharging experiment using finned tubes ($T_{H,in}$ = 9°C, 1.1 L/min)

Figure 6.12 shows the amount of energy recovered over time. The amount recovered was 7.28 MJ, which is closely aligned with the theoretical storage capacity. The uncertainty

associated with the energy recovered was 45%. Since the temperature difference in the HTF inlet and outlet temperature was higher than experiment 10, the uncertainty was observed to be lower in comparison. The proximity of the total recovery to theoretical storage capacity is consistent with previous experiment and increases the confidence in the results.

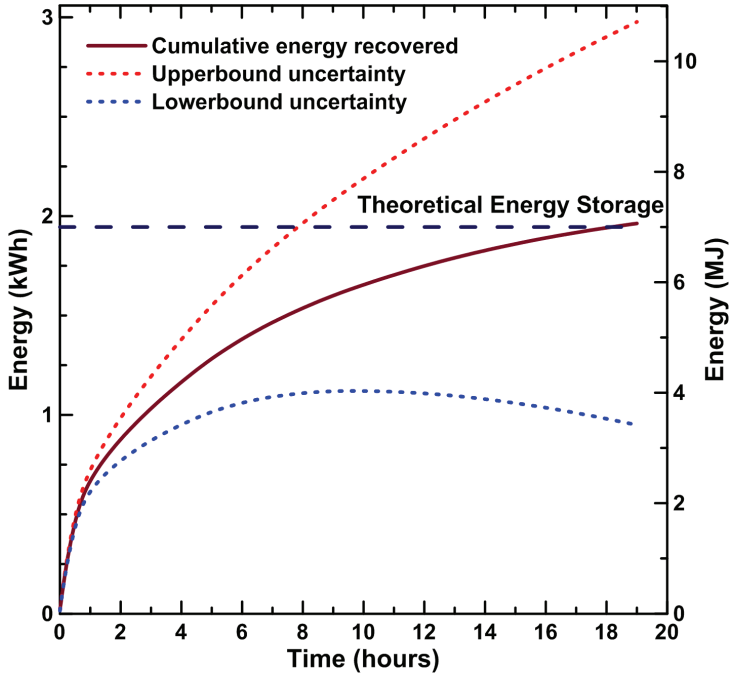

Figure 6.12 Cumulative energy recovered as a function of time during discharging experiment using finned tubes ($T_{H,in}$ = 9°C, 1.1 L/min)

Table 6.3 shows a summary of the power out range, cumulative energy recovered and discharging time for discharge experiments on the coil and finned tubes heat exchangers.

Table 6.3 Summary of the discharging results of the coil and finned tubes heat exchangers

Experiment	Power output range (kW)	Cumulative Energy recovered (MJ)	Discharging time (Hours)
10	0.3-0.05	7.29 ± 71 %	17
11	1.6-0.025	7.28 ± 45 %	10

6.5 VALIDATION OF THE FOURIER NUMBER ANALOGY

The coil used for Tank A was not deliberately designed using the method described in section 3.4.2, however its dimensions happened to coincidentally match to a certain degree with the dimensions found using the uniformity of the heat diffusion method. Therefore the comparison between the two coils is based mainly on the effect of the characteristic length on the overall performance of the system. The method described in section 3.4.2 takes into account the computed Fourier number to describe the state of discharge of the tank. For Tank A, the calculated Fourier number using Eq. (3.9) was 2.97 for the state of the tank at the end of the discharge process. This was determined using the observed characteristic time for the discharge process. Therefore this method does depend on an experimental prototype in order to provide the initial experimental information needed (*i.e.* discharge time). The method as described earlier takes into account this Fourier number as a reference to state of discharge. Therefore if the desired outcome is decreasing the time required for the discharge process, and the state of discharge is described by the Fourier number previously determined, therefore the characteristic length must decrease since they are inversely proportional as shown in Eq. (3.9). The characteristic length for the coils in Tank A and B were 8 cm and 5.25 cm, respectively. Therefore, the characteristic length required for a desired discharge time can be described using Eq. (6.1):

$$L = \sqrt{\frac{\alpha t_{desired}}{Fo}} \tag{6.1}$$

As shown in section 3.4.3, the characteristic length for a coil heat exchanger is dependent on the diameter of the tank (Eq. (3.13)), therefore a validation based on a desired time requires specific tank dimensions. Given that there were certain limitations based on the tank available, the validation using the desired time could not be performed. However, by studying a different tank with a known characteristic length, the method should allow for an accurate prediction of the discharge time using the Fourier number analogy, which serves as an equivalent validation but using a different approach.

Therefore, the discharge time for a given characteristic length can be determined by using Eq. (6.2):

$$t_c = \frac{FoL^2}{\alpha} \tag{6.2}$$

Equation (6.2) was used in order to predict time required for Tank B to reach the state of discharge described by the Fourier number value of 2.97. The predicted time was 25.77 hours. The experimentally observed discharge time was 27 hours. These calculations are shown in Appendix B. The percent difference between the two values is 1 %, while the percent error is 4.5%. Therefore, it is compelling to consider the validity of such an analogy with such a prediction of the discharge time.

The value of such method in a LHESS design is to provide the ability to determine the maximum allowable characteristic length of diffusion that a certain heat exchanger can have in order to discharge the energy in the desired amount of time. For instance, in the case of the tanks and coil heat exchangers discussed in this thesis, if the desired time for discharge was 12 hours the maximum allowable characteristic length to achieve that using a coil would be 3.6 cm, which translates into a coil with a diameter of 14.3 cm and a tank with a diameter of 20 cm.

Figure 6.13 shows a possible design for Tank A with 5 helical coils. Each coil's diameter is 14.3 cm as determined with the Fourier number analogy. All five coils engage the middle section. Setting them up in parallel would require a higher flow rate before splitting the flow in order to achieve the same flow rate in the coil as the series setup. Therefore, the setup of these coils would preferably be in series in order to achieve higher residence time which in effect will provide a cumulative increase in the temperature difference between the HTF inlet and outlet temperatures.

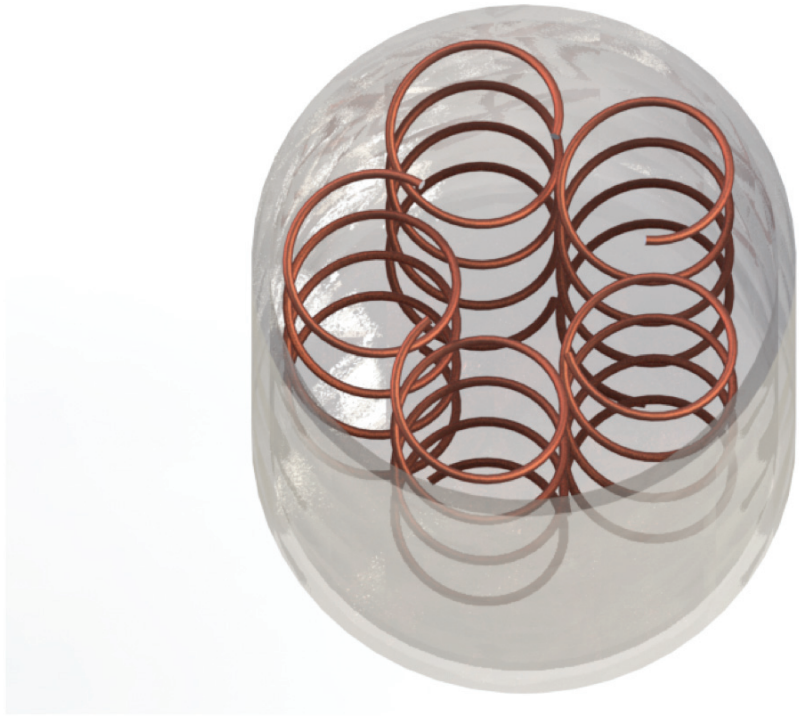

Figure 6.13 Multiple coil design based on Fourier number Analogy

Therefore, a probable method of design with multiple coils would include considering any given tank as a combination of smaller tanks, each associated with its own local maximum allowable characteristic lengths.

6.6 CONCLUSION

Chapter 6 showed experiments on Tank B conducted using coil and finned tubes heat exchanger. It was found that the use of finned tubes heat exchanger had a significant impact on the overall performance of the system in comparison to the use of the coil heat exchanger. The use of finned tubes showed an increase in the power inputs by 60% and a decrease of charging time by 7 hours. The benefit of the finned tubes was also shown during discharge whereas it showed a significant increase in power output during the initial discharge period, which resulted in a decrease in the overall discharge time by 8 hours.

Tank B was used for validation of the Fourier number analogy. The discharge time required for Tank B using the coil heat exchanger was predicted by using the characteristic length of Tank B and the Fourier number that was determined from the discharge experiment conducted on Tank A. The predicted discharge time was within 5% of the observed discharge time, which provides a compelling case in support of the Fourier number design methodology. In addition, a multiple coil design proposal based on the Fourier number design method was shown.

CHAPTER 7 CONCLUSIONS AND FUTURE WORK

The use of LHESS is a possible method of overcoming space barriers for high requirement thermal energy storage applications (*i.e.* large scale SDWH). This thesis presented an experimental characterization of a LHESS under real-time solar conditions and controlled conditions. The PCM used in these experiments was dodecanoic acid (lauric acid). Three LHESS, consisting of two separate tanks (Tank A and B) were studied experimentally.

Tank A used a helical coil heat exchanger and was tested under real-time solar conditions and controlled experimental conditions. Controlled experiments included a parametric characterization of the tank through varying the HTF inlet temperature and flow rate during charging. Real-time solar experiments were conducted on a seasonal basis. A direct comparison between a latent storage system using PCM and a sensible storage system using water was conducted.

By considering the discharge process as the limiting factor of a LHESS, a design method that proposes improving discharge times was proposed. The method was based on the Fourier number. Tank B was used in order to validate the proposed design method. Two separate heat exchangers (helical coil and finned tubes) were tested and compared using Tank B.

7.1 CONCLUSIONS

Controlled experiments on Tank A using various HTF inlet temperatures (*i.e.* various Ste number values) indicated that an increase of the HTF inlet temperature significantly increases heat transfer rates (power inputs) and reduced charging time. The phase change behavior was analyzed in the tank through the observation of thermocouple temperature profiles. It was shown that the top of the tank exhibited faster melting and showed higher temperatures. This is explained by the onset of natural convection, which

increased the overall heat transfer coefficient and thus reduced the thermal resistance from the water to the PCM. In addition, it was observed that the increase of the HTF inlet temperature significantly increased the temperatures recorded by the probes located at the top of the tank, which indicates that the reduction in melting time with higher HTF inlet temperature is partly due to the increase of the heat transfer coefficient due to natural convection.

Various HTF flow rates were also used in order to study the effect of flow rate on the system. It was observed that the increase of flow rate increased heat transfer rates and reduced charging time. This can be explained by the effect of increasing the heat transfer coefficient due to forced convection, which in effect increases the overall heat transfer coefficient of the system. However, the degree at which this occurred was not as significant as the increase of the HTF inlet temperature. Which points to the fact that the thermal resistance due to heat transfer in the PCM is more critical than the resistance due to internal forced convection. Thus, it can be concluded that the increase of the Stephan number plays a more significant role on the overall heat transfer coefficient than the increase of the Reynolds number.

Real-time solar experiments were conducted for November 2013, February, March and July 2014. The LHESS performance varied with the available solar energy and the length of the day. The temperature profiles shown by the thermocouples in the tank showed very little melting during shorter days, making conduction the main heat transfer mode, which explains the poor performance of the system. Sunnier and longer days such as July showed significant melting and a much better overall performance. For instance, the amount of energy stored in July was 4 times the amount stored in November.

Municipal water was used to discharge the system. Two experiments with various conditions of the water's flow rate and temperature were used. The time required for discharged was significantly longer than the charging experiments. It was found that the decrease of the HTF inlet temperature showed some improvement to the system's performance, while the increase of the HTF flow rate did not have any significant impact. In addition, the dominant mode of heat transfer was found to be conduction,

which explains the system's lack of response to the increase of the heat transfer coefficient due to internal forced convection.

A direct comparison between PCM and water was conducted under similar solar conditions in March for charging and municipal water for discharging. The amount of energy stored by the water was 50% higher than that stored by the PCM. However, the amount stored by the water was near its maximum storage capacity after a 6-hour solar charge, however the PCM had 59% of its theoretical storage capacity remaining. The solar collector efficiency was determined for both the PCM and water experiments. It was found that the collector efficiency was significantly lower for the PCM experiments due to the lower temperature difference between the inlet and outlet temperatures to the collector. Therefore, it was found that the performance of the heat exchanger in the LHESS does not only affect the system's ability to store solar energy, but it also affects its ability to collect it. The municipal discharge for the water and PCM storage highlighted the amplitude of the problem associated with the use of PCM. The power outputs for the water discharge were 6 to 8 times higher than that observed for PCM. The rate of energy transfer from the water tank was substantially faster than the PCM tank, requiring only 4.5 hours in the case of water for energy discharge, versus nearly 60 hours to release the energy from the PCM.

Experiments on Tank B showed that the use of finned tubes heat exchanger had a significant impact on the overall performance of the system in comparison to the use of the coil heat exchanger. The use of finned tubes showed an increase in the power inputs by 60%, and a decrease of charging time by 7 hours. The benefit of the finned tubes was also shown during discharge whereas it showed a significant increase in power output during the initial discharge period, which resulted in a decrease in the overall discharge time by 8 hours.

Tank B was used for validation of the Fourier number analogy. The discharge time required for Tank B using the coil heat exchanger was predicted by using the characteristic length of Tank B and the Fourier number that was determined from the discharge experiment conducted on Tank A. The predicted discharge time was within

5% of the observed discharge time, which provides a compelling case in support of the Fourier number design methodology.

7.2 RECOMMENDATIONS AND FUTURE WORK

Real-time solar charging indicated that the solar collector efficiency was dependent on the performance of the heat exchanger within the LHESS. Therefore it is recommended that an evaluation of the effect of various heat exchangers (*e.g.* finned tubes, multiple coils) on the solar collector's efficiency be performed.

Since it was observed that the main issue with LHESS is the ability to compete with the heat transfer rates of water-based storage systems, it is recommended that design considerations be focused largely on heat transfer enhancement for discharging.

The Fourier number analogy can be valuable when it comes to providing a design methodology that accommodates a desired discharge time. Therefore, future work studying various heat exchangers and tank sizes should be performed to gain further validation of the Fourier number design method. In addition, future work can encompass the use of multiple coils in the tank based on the Fourier number method proposed in order to improve the overall performance of the LHESS.

The PCM in this study, dodecanoic acid, provides 60% greater storage capacity than water within the operating temperature range of SDWH. Future work should explore the use of other PCMs with higher storage densities within the temperature range for SDWH systems. As well as the impact of the PCM melting temperature on the storage and recovery behaviour of LHESS, especially during real-time solar charging.

References

Abhat, A. (1983). Low Temperature Latent Heat Thermal Energy Storage: Heat Storage Materials. *Solar Energy, 30*(4), 313-332.

Agyenim, F., Eames, P., and Smyth, M. (2009). A comparison of heat transfer enhancement in a medium temperature thermal energy storage heat exchanger using fins. *Solar Energy, 83*(9), 1509-1520.

Agyenim, F., Eames, P., and Smyth, M. (2010a). Heat transfer enhancement in medium temperature thermal energy storage system using a multitube heat transfer array. *Renewable Energy, 35*(1), 198-207.

Agyenim, F., Hewitt, N., Philip, E., and Smyth, M. (2010b). A review of materials, heat transfer and phase change problem formulation for latent heat thermal energy storage systems (LHTESS). *Renewable and Sustainable Energy Reviews, 14*, 615-628.

Al-Hinti, I., Al-Ghandoor, A., Maaly, A., Abu Naqeera, I., Al-Khateeb, Z., and Al-Sheikh, O. (2010). Experimental investigation on the use of water-phase change material storage in conventional solar water heating systems. *Energy Conversion and Management, 51*(8), 1735-1740.

Alvarado, J., Marsh, C., Sohn, C., Phetteplace, G., and Newell, T. (2007). Thermal performance of microencapsulated phase change material slurry in turbulent flow under constant heat flux. *International Journal of Heat and Mass Transfer, 50*(9-10), 1938-1952.

ASHRAE Handbook. (2009). 2009 -ASHRAE Handbook Fundamentals (I-P Edition): American Society of Heating, Refrigerating and Air-Conditioning Engineers, Inc.

Bédard, N., and Leduc, M. A. (2011). Bilan d'opération de systèmes solaires thermiques au LTE. *Infobec (ASHRAE Quebec Chapter), 35*, 6.

Bertram, R. W. (1981). Chapter 7: Testing and standards for thermal solar collectors. In A. F. J. K. Swartman (Ed.), *Solar Energy Conversion II* (pp. 73-91): Pergamon.

Cabeza, L., and Sole, C. (2007). State of development of the work with PCM modules in DHW tanks at the University of Lleida. In W. Streicher (Ed.), *Laboratory Prototypes of PCM Storage Units* (pp. 21-26): University of Lleida.

Cabeza, L. F., Mehling, H., Hiebler, S., and Ziegler, F. (2002). Heat transfer enhancement in water when used as PCM in thermal energy storage. *Applied Thermal Engineering, 22*, 1141–1151.

Castell, A., Belusko, M., Bruno, F., and Cabeza, L. F. (2011). Maximisation of heat transfer in a coil in tank PCM cold storage system. *Applied Energy, 88*(11), 4120-4127.

Castell, A., Sole, C., Medrano, M., Roca, J., Cabeza, L., and Garcia, D. (2008). Natural convection heat transfer coefficients in phase change material (PCM) modules with external vertical fins. *Applied Thermal Engineering, 28*(13), 1676-1686.

Chaabane, M., Mhiri, H., and Bournot, P. (2014). Thermal performance of an integrated collector storage solar water heater (ICSSWH) with phase change materials (PCM). *Energy Conversion and Management, 78*(0), 897-903.

Desgrosseilliers, L., Catherine A. Whitman, Dominic Groulx, and White, M. A. (2013). Dodecanoic acid as a promising phase-change material for thermal energy storage. *Applied Thermal Engineering, 53*, 37-41.

Desgrosseilliers, L., Murray, R. E., Sefati, A., Marin, G., Stewart, J., Osbourne, N., White, M. A., and Groulx, D. (2011). *Phase Change Material Selection in the Design of a Latent Heat Energy Storage System Coupled with a Domestic Hot Water Solar Thermal System*. Paper presented at the ASHRAE Annual Conference 2011, Montréal, Canada.

Dimaano, M. N., and Escoto, A. D. (1998). Preliminary Assessment of a mixture of carpric and lauric acids for low-temperature thermal energy storage. *Energy, 23*(5), 421-427.

Farid, M. M., AKhudhair, M., Razack, S. A. K., and Al-Hallaj, S. (2004). A review on phase change energy storage: materials and applications. *Energy Conversion and Management, 45*, 1597-1615.

Fukai, J., Hamada, Y., Morozumi, Y., and Miyatake, O. (2003). Improvement of thermal characteristics of latent heat thermal energy storage units using carbon-fiber brushes: experiments and modeling. *International Journal of Heat and Mass Transfer, 46*(23), 4513-4525.

Garg, H. P., Mullick, S. C., and Bhargava, A. K. (1985). *Solar Thermal Energy Storage*: D. Reidel Publishing Company.

Ghoneim, A. A. (1989). Comparison of theoretical models of phase-change and sensible heat storage for air and water-based solar heating systems. *Solar Energy, 42*(3), 209-220.

Halifax Regional Municipality. (2012). Solar City Initiative. 2012, from http://www.halifax.ca/solarcity/

Hamdan, M., and Elwerr, F. A. (1996). Thermal energy storage using a phase change material. *Solar Energy, 56*(2), 183-189.

Hasnain, M. S. (1997). Review on sustainable thermal energy storage technologies, part i: heat storage materials and techniques. *Energy Conversion and Management, 39*(11), 1127-1138.

IEA. (2008). Worldwide Trends in Energy Use and Efficiency. France: International energy agency.

Ilken, Z., and Toksoy, M. (1993). Effect of fin length on solidification rate in a latent heat energy storage system *Experimental Heat Transfer, Fluid Mechanics and Thermodynamics 1993* (pp. 524-528). Amsterdam: Elsevier.

Incropera, F. P., Dewitt, D. P., Bergman, T. L., and Lavine, A. S. (2011). *Funadementals Of Heat and Mass Transfer* (Vol. 7). United States.

Jesumathy, S. P., Udayakumar, M., Suresh, S., and Jegadheeswaran, S. (2014). An experimental study on heat transfer characteristics of paraffin wax in horizontal double pipe heat latent heat storage unit. *Journal of the Taiwan Institute of Chemical Engineers, 45*(4), 1298-1306.

Jiao, C., Ji, B., and Fan, D. (2012). Preparation and properties of lauric acid–stearic acid/expanded perlite composite as phase change materials for thermal energy storage. *Materials Letters, 67*, 352-354.

Jones, B., Sun, D., Krishnan, S., and Garimella, S. (2006). Experimental and numerical study of melting in a cylinder. *International Journal of Heat and Mass Transfer, 49*(15-16), 2724-2738.

Khalifa, A., Tan, L., Date, A., and Akbarzadeh, A. (2014). A numerical and experimental study of solidification around axially finned heat pipes for high temperature latent heat thermal energy storage units. *Applied Thermal Engineering, 70*(1), 609-619.

Lane, G. A. (1983). *Solar heat storage: background and scientific principles*: CCRC Press.

Lane, G. A. (1985). PCM Science and Technology: The Essential Connection. *ASHRAE Transactions, 91*(2b), 1897.

Lane, G. A., Kott, A. C., Warner, G. L., Hartwick, P. B., and Rossow, H. E. (1978). Macro-encapsulation of heat storage phase-change materials for use in residential buildings: report ORO/5217-8. Midland, MI.: Dow Chemical Company.

Li, S., Zhang, Y., Zhang, K., Li, X., Li, Y., and Zhang, X. (2014). Study on Performance of Storage Tanks in Solar Water Heater System in Charge and Discharge Progress. *Energy Procedia, 48*(0), 384-393.

Liu, C., and Groulx, D. (2014). Experimental study of the phase change heat transfer inside a horizontal cylindrical latent heat energy storage system. *International Journal of Thermal Sciences, 82*, 100-110.

Liu, H., Li, S., Chen, Y., and Sun, Z. (2014). The melting of phase change material in a cylinder shell with hierarchical heat sink array. *Applied Thermal Engineering, 73*(1), 973-981.

Massoud, M. (2005). Fluid Mechanics *Engineering Thermofluids* (pp. 223-430): Springer Berlin Heidelberg.

Mehling, H., Cabeza, L. F., Hippeli, S., and Hiebler, S. (2003). PCM-module to improve hot water heat stores with stratification. *Renewable Energy, 28*(5), 699-711.

Mehmet, E., Durmus, A., and Durmus, A. (1997). Geometric design of solar-aided latent heat store depending on various parameters and phase change materials. *Solar Energy, 62*(1), 19-28.

Mettawee, S., and Assassa, G. (2006). Experimental study of a compact PCM solar collector. *Energy, 31*(14), 2958-2968.

Mills, A., Farid, M., Selman, J., and Alhallaj, S. (2006). Thermal conductivity enhancement of phase change materials using a graphite matrix. *Applied Thermal Engineering, 26*(14-15), 1652-1661.

Murray, R., Desgrosseilliers, L., Stewart, J., Osbourne, N., Marin, G., Safatli, A., Groulx, D., and White, M. A. (2011). *Design of a Latent Heat Energy Storage System Coupled with a Domestic Hot Water Solar Thermal System*. Paper presented at the World Renewable Energy Congress 2011, Linköping.

Murray, R., and Groulx, D. (2014a). Experimental study of the phase change and energy characteristics inside a cylindrical latent heat energy storage system: Part 1 consecutive charging and discharging. *Renewable Energy, 62*, 571-581.

Murray, R. E., and Groulx, D. (2014b). Experimental study of the phase change and energy characteristics inside a cylindrical latent heat energy storage system: Part 1 consecutive charging and discharging. *Renewable Energy, 62*, 571-581.

Nomura, T., Tsubota, M., Oya, T., Okinaka, N., and Akiyama, T. (2013). Heat storage in direct-contact heat exchanger with phase change material. *Applied Thermal Engineering, 50*(1), 26-34.

NRCAN. (2012). Energy use data handbook:1990-2009. from Government of Canada

Padovan, R., and Manzan, M. (2014). Genetic optimization of a PCM enhanced storage tank for Solar Domestic Hot Water Systems. *Solar Energy, 103*, 563-573.

Py, X., Olives, R., and Mauran, S. (2001). Paraffin/porous-graphite-matrix composite as a high and constant power thermal storage material. *International Journal of Heat and Mass Transfer, 44*(14), 2727-2737.

Rahimi, M., Ranjbar, A. A., Ganji, D. D., Sedighi, K., Hosseini, M. J., and Bahrampoury, R. (2014). Analysis of geometrical and operational parameters of PCM in a fin and tube heat exchanger. *International Communications in Heat and Mass Transfer, 53*(0), 109-115.

Sarı, A., Karaipekli, A., and Alkan, C. (2009). Preparation, characterization and thermal properties of lauric acid/expanded perlite as novel form-stable composite phase change material. *Chemical Engineering Journal, 155*, 899-904.

Sarı, A., and Kaygusuz, K. (2002). Thermal and heat transfer characteristics in a latent heat storage system using lauric acid. *Energy Conversion and Management, 43*, 2493-2507.

Sciacovelli, A., Gagliardi, F., and Verda, V. (2015). Maximization of performance of a PCM latent heat storage system with innovative fins. *Applied Energy, Volume 137*(0), 707–715.

Scotian Windfields. (2009). Case Study: 21 Plateau - Killam Properties (pp. 2). Halifax,NS.

Sharma, A., Tyagi, V. V., Chen, C. R., and Buddhi, D. (2009). Review on thermal energy storage with phase change materials and applications. *Renewable and Sustainable Energy Reviews, 13*(2), 318-345.

Sharma, S. D., and Sagara, K. (2005). Latent Heat Storage Materials and Systems: A Review. *International Journal of Green Energy, 2*(1), 1-56.

Shokouhmand, H., and Kamkari, B. (2013). Experimental investigation on melting heat transfer characteristics of lauric acid in a rectangular thermal storage unit. *Experimental Thermal and Fluid Science, 50*, 201-212.

Shukla, R., Sumathy, K., Erickson, P., and Gong, J. (2013). Recent advances in the solar water heating systems: A review. *Renewable and Sustainable Energy Reviews, 19*(0), 173-190.

Singh, R. P., and Heldman, D. R. (2014). Heat Transfer in Food Processing. 265-419.

Solomon, A. D. (1979). Melt time and heat flux for a simple PCM body. *Solar Energy, 22*(3), 251-257.

Tay, N. H. S., Bruno, F., and Belusko, M. (2013). Experimental investigation of dynamic melting in a tube-in-tank PCM system. *Applied Energy, 104*, 137-148.

Velraj, R., Seeniraj, R. V., Hafner, B., Faber, C., and Schwarzer, K. (1998). Heat transfer enhancement in a latent heat storage system. *Solar Energy, 65*(3), 171-180.

Zalba, B., Marin, J., Cabeza, L., and Mehling, H. (2003). Review on thermal energy storage with phase change materials, heat transfer analysis and applications. *Applied Thermal Engineering, 23*, 251-283.

Zeng, R., Wang, X., Chen, B., Zhang, Y., Niu, J., Wang, X., and Di, H. (2009). Heat transfer characteristics of microencapsulated phase change material slurry in laminar flow under constant heat flux. *Applied Energy, 86*(12), 2661-2670.

Ziegler, F. (2010). The multiple meanings of the Stefan-number (and relatives) in refrigeration. *International Journal of Refrigeration, 33*(7), 1343-1349.

Zivkovic, B., and Fujii, I. (2001). An analysis of isothermal phase change of phase change material within rectangular and cylindrical containers. *Solar Energy, 70*(1), 51-61.

Zuo, J., Li, W., and Weng, L. (2011). Thermal properties of lauric acid/1-tetradecanol binary system for energy storage. *Applied Thermal Engineering, 31*, 1352-1355.

APPENDIX A: UNCERTAINTY PROPOGATION

Equation (3.5) is used to experimantily quanitfy the energy input/output, while the uncertainty associated with it is given by Eq. (3.6). The partial derivatives of the heat input/ouput Q relatively to the measurent quantities are given in Eqs. (A.1), (A.2) and (A.3)

$$Q_{input/output} = t\dot{m}C_{p_{HTF}}(T_{out} - T_{in}) \pm \delta_Q \tag{3.5}$$

$$\delta_Q = \sqrt{\left(\frac{\partial Q}{\partial \dot{m}}\delta_{\dot{m}}\right)^2 + \left(\frac{\partial Q}{\partial T_{out}}\delta_{T_{out}}\right)^2 + \left(\frac{\partial Q}{\partial T_{in}}\delta_{T_{in}}\right)^2} \tag{3.6}$$

$$\frac{\partial Q}{\partial \dot{m}} = tCp_{HTF}(\Delta T) \tag{A.1}$$

$$\frac{\partial Q}{\partial T_{out}} = tCp_{HTF}\dot{m} \tag{A.2}$$

$$\frac{\partial Q}{\partial T_{in}} = -tCp_{HTF}\dot{m} \tag{A.3}$$

The derived values from Eq. (A.1) to (A.3) were substituted in Eq. (3.6), which resulted in the following:

$$\delta_Q = \sqrt{(tCp_{HTF}(\Delta T)\delta_{\dot{m}})^2 + \left(tCp_{HTF}\dot{m}\delta_{T_{out}}\right)^2 + \left(-tCp_{HTF}\dot{m}\delta_{T_{in}}\right)^2} \tag{A.4}$$

$$\delta_Q = \sqrt{tCp_{HTF}{}^2\left[(\Delta T\delta_{\dot{m}})^2 + \left(\dot{m}\delta_{T_{out}}\right)^2 + \left(-\dot{m}\delta_{T_{in}}\right)^2\right]} \tag{A.5}$$

This can be further reduced to the equation used to compute the uncertainty, given by Eq. (3.7):

$$\delta_Q = tCp_{HTF}\sqrt{(\Delta T\delta_{\dot{m}})^2 + \left(\dot{m}\delta_{T_{out}}\right)^2 + \left(-\dot{m}\delta_{T_{in}}\right)^2} \tag{3.7}$$

APPENDIX B: FOURIER ANALOGY CALCULATIONS

As mentioned in section 6.5, the Fourier number for the state of the tank after the discharge process of Tank A was complete was calculated using the observed discharge time and the known characteristic length. Using Eq. (3.9), where t_c was 60 hours, and L was 8 cm. The properties of the PCM were taken for the solid state as given in section 4.4.

$$Fo = \frac{k}{C_p \rho} \frac{t}{L^2} = \frac{0.16 \frac{W}{m.K} \times 60\ hours \times 3600\ (\frac{seconds}{hour})}{1950 \frac{J}{kg.K} \times 930 \frac{kg}{m^3} \times (0.08\ m)^2} = 2.97 \tag{3.9}$$

The Fourier value was then used to predict the time required for the discharge process in Tank B to reach the state observed in Tank A. The characteristic length of Tank B was 5.25 cm. The predicted time was calculated using Eq. (6.2):

$$t_c = \frac{Fo \times C_p \times \rho \times L^2}{k} \tag{6.2}$$

$$= \frac{2.97 \times 1950 \frac{J}{kg.K} \times 930 \frac{kg}{m^3} \times (0.0525\ m)^2}{0.16 \frac{W}{m}.K} \frac{1\ hour}{3600\ second}$$

$$= 25.7\ hours$$

APPENDIX C: ADDITIONAL REAL-TIME SOLAR CHARGING RESULTS

Additional data for solar days with the setup located on the roof was recorded. This appendix shows two solar days in August. The first day, which happens to be on August 13th 2014, shows a bit of overcast during certain parts of the day, while August 14th 2014 shows a clear day.

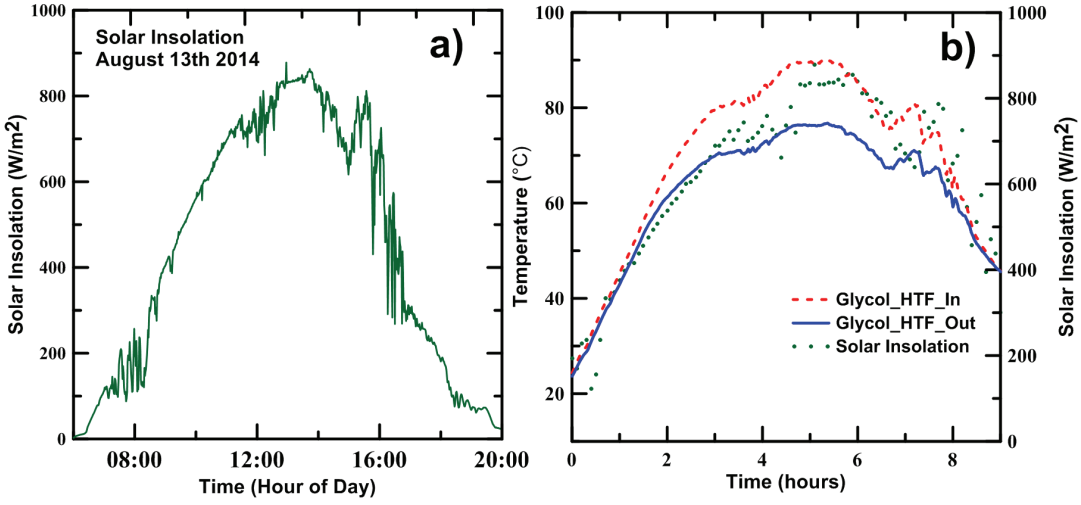

Figure C.1 a) Solar insolation on August 13th 2014, b) Glycol inlet/outlet temperatures relatively to solar insolation

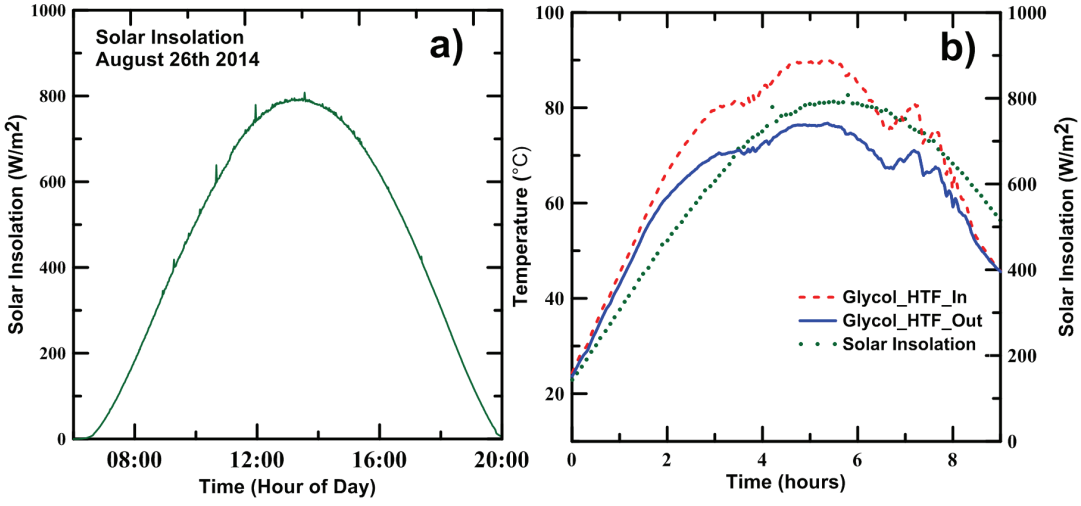

Figure C.2 a) Solar insolation on August 26th 2014, b) Glycol inlet/outlet temperatures relatively to solar insolation

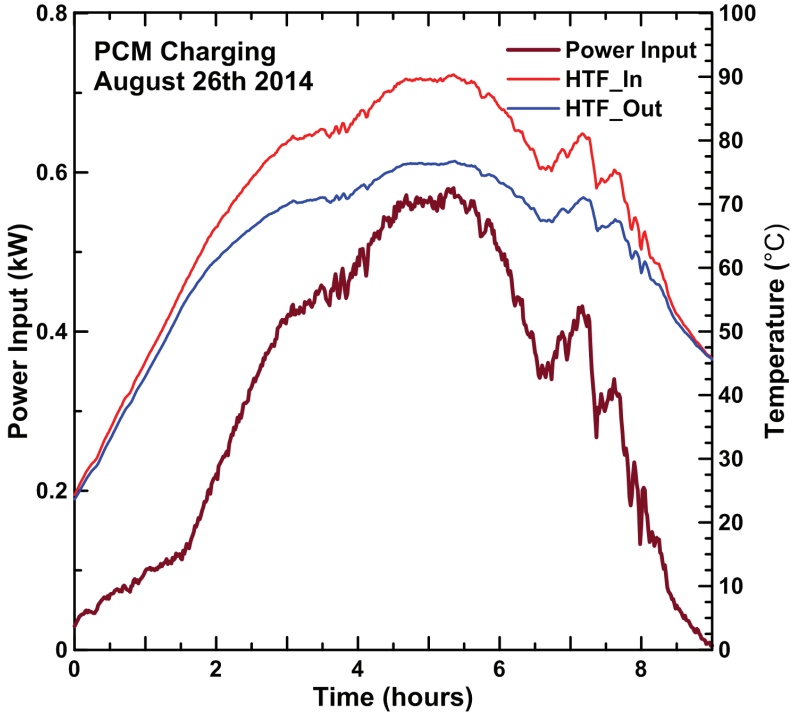

Figure C.3 Power input and HTF inlet and outlet temperatures as a function of time during PCM charging on August 13th 2014.

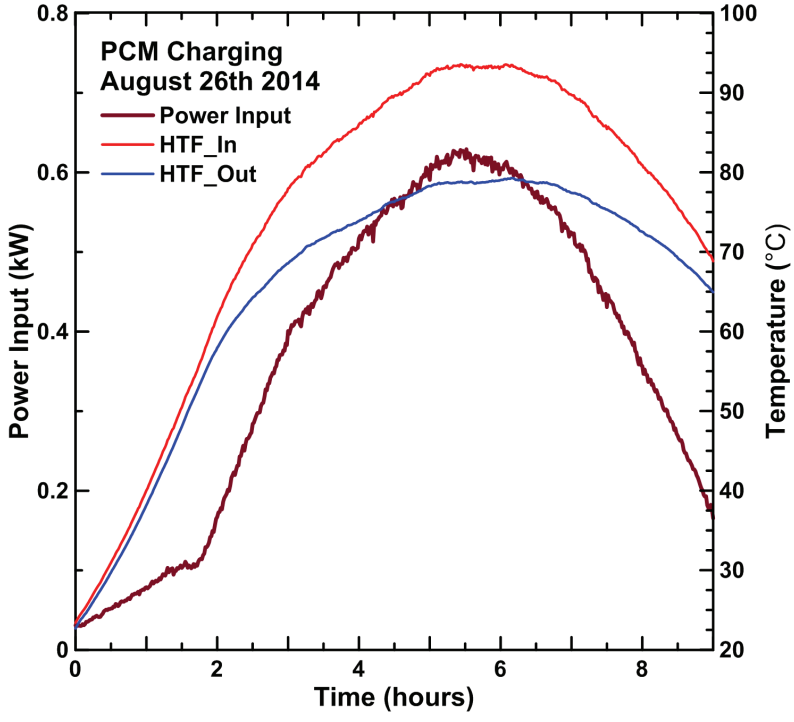

Figure C.4 Power input and HTF inlet and outlet temperatures as a function of time during PCM charging on August 26th 2014.

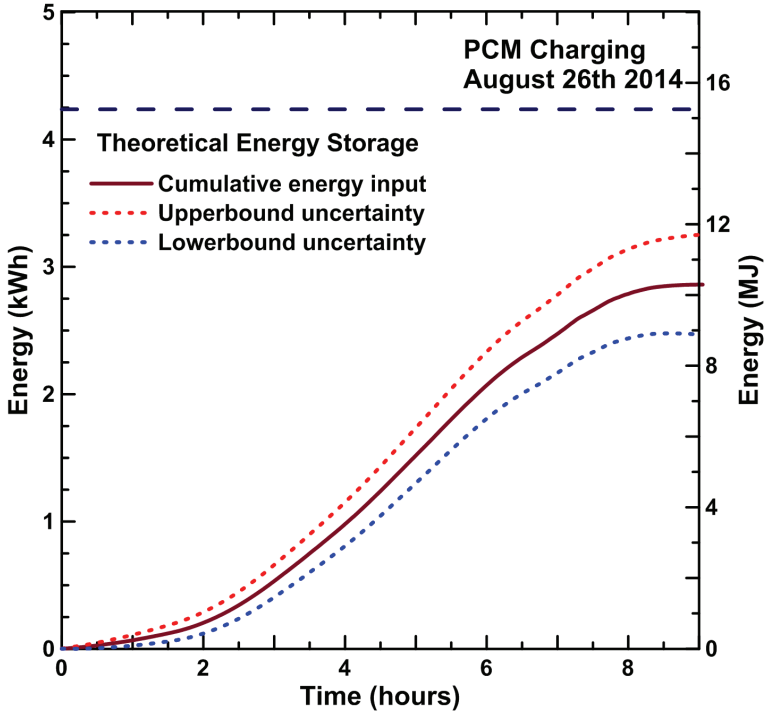

Figure C.5 Cumulative energy stored as a function of time during PCM charging on August 13th 2014.

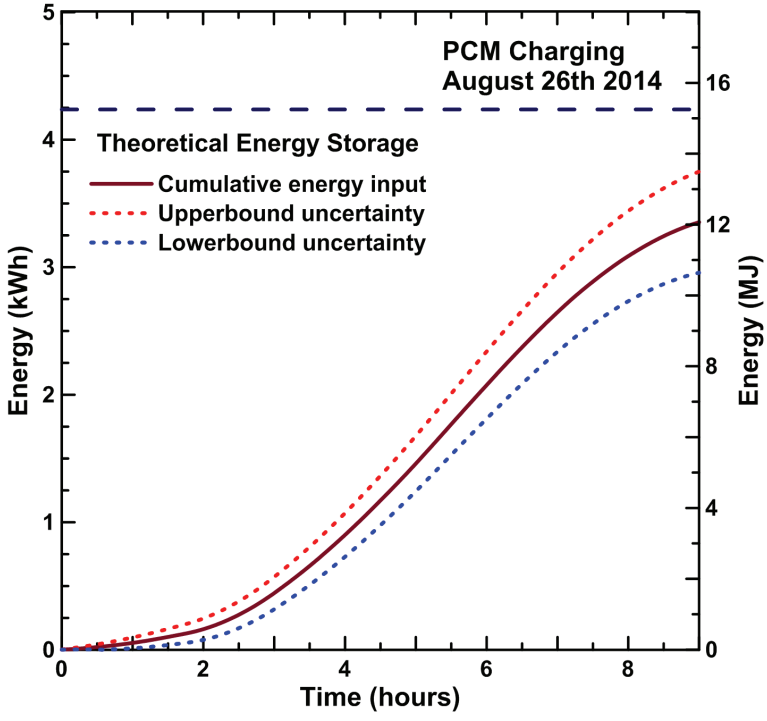

Figure C.6 Cumulative energy stored as a function of time during PCM charging on August 26th 2014.